Eberhard Altstadt; Hans-Georg Willschuetz;
Bal Raj Sehgal; Frank-Peter Weiss

SARNET – Corium – WP 10-2

Modelling of in-vessel retention after
relocation of corium into the lower plenum

FZR   Forschungszentrum
Rossendorf

Eberhard Altstadt; Hans-Georg Willschuetz;
Bal Raj Sehgal; Frank-Peter Weiss

SARNET – Corium – WP 10-2
Technical Report

Modelling of in-vessel retention after relocation of corium into the lower plenum

ZR Forschungszentrum
Rossendorf

SARNET – Corium – WP 10-2
Technical Report

Modelling of in-vessel retention after relocation of corium into the lower plenum

Authors:

Eberhard Altstadt
Hans-Georg Willschuetz
Bal Raj Sehgal
Frank-Peter Weiss

October 10, 2005

Abstract

Considering the unlikely core melt down scenario for a light water reactor (LWR) a possible failure mode of the reactor pressure vessel (RPV) and its failure time has to be investigated for a determination of the loadings on the containment. Worldwide several experiments have been performed accompanied with material properties evaluation, theoretical, and numerical work.

At the Institute of Safety Research of the FZR a finite element model has been developed simulating the thermal processes and the viscoplastic behaviour of the vessel wall. An advanced model for creep and material damage has been established and has been validated using experimental data. The thermal and the mechanical calculations are sequentially and recursively coupled. The model is capable of evaluating fracture time and fracture position of a vessel with an internally heated melt pool.

The model was applied to pre- and post test calculations for the FOREVER test series representing the lower head RPV of a PWR in the geometrical scale of 1:10. These experiments were performed at the Royal Institute of Technology in Stockholm. The results of the calculations can be summarised as follows:

- The creeping process is caused by the simultaneous presence of high temperature (>600 °C) <u>and</u> pressure (>1 MPa)

- The hot focus region is the most endangered zone exhibiting the highest creep strain rates.

- The exact level of temperature and pressure has an influence on the vessel failure time but not on the failure position

- The failure time can be predicted with an uncertainty of 20 to 25%. This uncertainty is caused by the large scatter and the high temperature sensitivity of the viscoplastic properties of the RPV steel.

- Contrary to the hot focus region, the lower centre of the vessel head exhibits a higher strength because of the lower temperatures in this zone. The lower part moves down without significant deformation. Therefore it can be assumed, that the vessel failure can be retarded or prevented by supporting this range.

- The development of a gap between melt crust and vessel wall could not be proofed.

First calculations for a PWR geometry were performed to work out differences and commonalities between prototypic scenarios and scaled experiments. The results of the FOREVER-experiments cannot be transferred directly to PWR geometry. The geometrical, mechanical and thermal relations cannot be scaled in the same way. Because of the significantly higher temperature level, a partial ablation of the vessel wall has to be to expected in the PWR scenario, which is not the case in the FOREVER tests. But nevertheless the FOREVER tests are the only integral in-vessel retention experiments up to now and they led to a number of important insights about the behaviour of a vessel under the loading of a melt pool and pressure.

Contents

Abbreviations and Symbols

<u>Abbreviations</u>

APDL	ANSYS parametric design language (Macro language)
CDB	Creep Data Base
CEA	Commissariat À L'Énergy Atomique
CFD	Computational Fluid Dynamics
CS	Coordinate system
ECCM	Effective convection conduction model
FE	Finite Element
FOREVER	Failure Of REactor VEssel Retention
GPE	General Physics Environment
GRS	Gesellschaft für Anlagen- und Reaktorsicherheit
HAZ	Heat affected zone
HTC	Heat transfer coefficient
ISTC	International Science and Technology Center
IVR	In vessel retention
KTH	Kungl Teknsika Högskolan
LHF	Lower Head Failure
LP	Lower plenum
LWR	Light Water Reactor
NoE	Network of Excellence
OECD	Organisation for Economic Co-operation and Development
OLHF	OECD Lower Head Failure Program
RPV	Reactor Pressure Vessel
RT	Room temperature
PWR	Pressure Water Reactor
SBLOCA	Small break loss of coolant accident
UPF	User Programmable Feature
VDI	Verein Deutscher Ingenieure

<u>Latin Symbols</u>

a	Temperature conductibility
D	Damage
E	Young's modulus (Elasticity modulus)
g	Gravity (g=9.81 m/s²)
H, h	Height
Nu	Nusselt number
Pr	Prandtl number
q	Heat flux density
Ra	Rayleigh number
R_v	Triaxiality function
T	Temperature
t	Time
w	Weighting factor

Greek Symbols

α	Heat transfer coefficient
β	Volumetric thermal expansion coefficient
ε	Strain or emission coefficient
$\dot{\varepsilon}$	Strain rate
ε_{frac}^{cr}	Creep fracture strain
ε_{eqv}^{cr}	Equivalent creep strain
$\Delta\varepsilon_{eqv}^{cr}$	Equivalent creep strain increment
ε_{frac}^{pl}	Plastic fracture strain
ε_{eqv}^{pl}	Plastic equivalent strain
ε_{eqv}^{pl}	Plastic equivalent strain increment
ρ	Density
κ	Plastic work
λ	Heat conductivity
ν	Poisson number or kinematic viscosity
σ	Mechanical stress
σ_{eqv}	von-Mises equivalent stress
σ_h	Hydrostatic stress
σ_Y	Yield strength
σ_{SB}	Stefan-Boltzmann constant

1 Introduction

1.1 Background

Several scenarios – with extreme low probability – are existing for a severe accident with relocation of corium into the lower plenum (LP). In general the ungoverned station black out (outage of all electrically driven emergency cooling systems) is considered as the initiating event. The core cannot be cooled sufficiently and is destroyed. The subsequent course of the accident depends amongst others on the following questions [Büscher et al., 1998]:

- Is all the cooling water in the RPV evaporated (e.g. as a consequence of an SBLOCA) or does a water pool remain in the lower plenum?

- Will the core be re-flooded?

- Can the system pressure be decreased?

The following facts depend from the answers to above questions:

- the amount and composition of the melt, which is relocated to the LP

- the constitution of the melt (debris bed or molten pool with crust)

- the primary stresses in the RPV wall (low pressure or high pressure path)

- the thermal load of the RPV wall and the location of the hot spot

These parameters on their part determine the failure time and the failure mode of the RPV. But also the construction of the RPV itself is of importance (e.g. wall thickness, existence of nozzles and penetrations). The mode of failure has a decisive influence to the source term for the containment [Büscher et al., 1999].

Therefore as well the experimental as the theoretical research in the field of in-vessel retention has again been intensified during the last years. The complexity of the thermal dynamic and mechanical processes requires at first a separate investigation of the different phenomena. In the following an overview about selected related activities is given.

1.2 Survey of related research activities

1.2.1 Thermal fluid dynamics of melts

The BALI experiments were conducted by CEA in Grenoble [Bernaz et al, 1997]. The convection of salt water was studied in a plane gap between two Perspex plates. The shape of the plates corresponded to a vertical cut through the lower head of a RPV. The abutting faces of the gap boundary were cooled by an organic fluid, what lead to solidification and crust formation during the natural convection. Wire meshes were applied to the wetted sides of the gap side walls. The impressed voltage lead to a heat generation in the salt water (Joule effect). This heat on the one hand and the cooled abutting faces on the other hand drove a natural convection. The experiment, which was not a prototypical one, has been used for validation of numerical thermal fluid dynamic models.

The RASPLAV experiments conducted at Kurchatov Institute Moscow aimed at the determination of thermal hydraulic properties of corium in the temperature range of up to 3000 °C [Asmolov, 1998]. Different mixtures of UO_2, ZrO_2 and Zr were melted in a special crucible by inductive side wall heating. The convection of the melt and

the solidification phenomena were studied in a hemispherical slice geometry. For this purpose a special measurement technique for high temperatures was developed. The experiments were supported by analytical and numerical models.

In the SIMECO experiment [Sehgal et al, 1998a] the convection was investigated in a scaled slice gap representing a longitudinal section of a RPV lower head. The scale was approximately 1:8. A binary salt ($NaNO_3$ - KNO_3) was used as a simulant melt. Later two-phase melts were employed. Phase segregation and the resulting charges in vessel wall thermal loadings were studied.

The numerical simulation of the thermal fluid dynamics of melts is either done by CFD codes (finite element codes and finite volume codes) or by simplified models, which are based on experimental correlations (e.g. effective conduction convection model – section 3.2). A detailed overview about models and phenomena is given in [Theofanous et al, 1997]. Specific problems to be solved in connection with corium melt are:

- Modelling of phase transition (liquid-solid), crust formation

- Stratification with several liquid phases (metal, oxide)

- Heat transfer between the phases

- Extreme temperature and velocity gradients between liquid and solid phases

- Modelling of physical properties (viscosity, heat conductivity, heat capacity, density) at high temperatures and in the region of phase transition

The prompt stratification of two-phase or multi-phase melts has been observed in many experiments [Asmolov, 1998]. Therefore, many of the simulations of the thermal fluid dynamics start from melt configurations that are already segregated [Kolev, 1996; Theofanous et al, 1997]. However, according to new results of the MASCA experiments [Müller 2003] it seems possible that more complex configurations of the phases could occur. In the solidified melts, as well homogeneous phases with coarse disperse precipitates as three layer configurations have been observed.

The corium melt convection in the lower head is highly turbulent as a consequence of the steep temperature gradients at the wall, the large geometric dimensions and the strong internal heat generation. The internal Rayleigh numbers (Ra') are close to 10^{16} depending on the configuration [Kolev, 1996; Theofanous et al 1997]. Therefore the turbulence model is decisive for the quality of CFD simulation. Nourgaliev investigated different turbulence approaches and carried out also direct numerical simulation [Nourgaliev et al, 1998] with the result that the conventional turbulence models (e.g. k-epsilon model) underestimate the upward heat flow especially in cases of higher Rayleigh numbers ($Ra_i > 10^{12}$). The direct numerical simulation (DNS) requires an extremely high mesh density – the number of nodes or grid points have to be in the order of magnitude of the Rayleigh number. This requirement leads to an unreasonable computational effort in the case of the LWR geometry. The Effective Conduction-Convection Model (ECCM) seems to be a promising alternative [Bui,1998].

1.2.2 Experiments and models related to creep of steel and to vessel failure

A large experimental data base of mechanical properties of selected German steels at high temperatures was generated by MPA Stuttgart [Obst und Maile, 1989; Bothe et al, 1991]. Creep curves and stress strain curves were generated in the temperature range up to 1000 °C. Especially the material behaviour during multi-axial stress states were investigated. The experiments were supported by FE models.

Similar programs were carried out for American RPV steels and Inconel [Rempe et al, 1993] and for the French RPV steel 16MND5 [Ikonen, 1999].

The LHF (lower head failure) experiments were carried out in the U.S.A. at the Sandia National Laboratories [Chu et al., 1999]. A succeeding test series (OLHF tests) was carried out under the umbrella of the OECD [Humphries et al, 2002]. The lower head was modelled in a scale of 1:5. The vessel was heated by an electrical radiator allowing to locate the hot focus at different position of the vessel. The maximum wall temperatures were around 900 °C. The vessel failure was initiated by internal pressure varying in the range of 53 to 123 bars. The experiments were accompanied by FE simulations.

The CORVIS experiment (Corium Reactor Vessel Interaction Studies) was carried out at the Paul-Scherrer-Institut in Switzerland [Hirschmann, 1997]. The melt through of a pipe welded to a medium scaled vessel bottom was investigated. The configuration was related to a melt pool in a BWR lower head with penetrations. The heat transfer from the metal melt into the vessel, the ablation of the vessel wall and the time until nozzle failure were investigated.

In the frame of the ISTC project METCOR the thermal chemical interaction between molten corium and vessel steel is investigated [Bechta et al, 2004]. An inductively heated corium melt is located on top of a RPV cylindrical steel specimen (diameter 40 mm). The ablation rate is studied in dependence on the interface temperature, the heat flux, the corium composition and its degree of oxidation and the atmosphere (inert or steam).

At the Royal Institute of Technology in Stockholm the FOREVER (Failure Of Reactor Vessel Retention) experiments were carried out [Sehgal et al, 1998b]. The test program is described in chapter 2 of this report.

1.2.3 Gap cooling

The phenomenon of gap cooling can be described as follows: if the deformation of the RPV wall and the solidified melt (crust) is different, a gap could be formed between the RPV wall and the crust. This leads to a decreased heat transfer to the vessel wall and – if water ingresses into this gap – to an additional cooling of melt and vessel wall.

There are several investigations related to the critical heat flux in plane or spherical gaps filled with water or steam [Suh et al, 1999a; Köhler et al, 1998]. In general, an existing gap with constant geometry is assumed in these experiments or simulations. The influence of surface roughness, the gap geometry etc. have been studied.

For the case of a predetermined gap with fixed geometry the thermal hydraulic processes are well understood. However, it is not yet finally clarified, under which circumstances a gap will be generated and which geometry this possible gap then will have [Schaaf, 1998]. In the LAVA experiments [Suh et al, 1999b] a thermite melt in a 1:10 scaled vessel was used to investigate the development of a gap. The post test examination of the cut vessel revealed that in tests with higher pressure as 17 bars a gap was existing. However, it was not clear, at which time this gap had been formed and if there was a water ingression or whether it was only a consequence of shrinking during the cool down.

No gap has been observed in all FOREVER tests (cf. chapter 2). The question of gap formation seems still to be open.

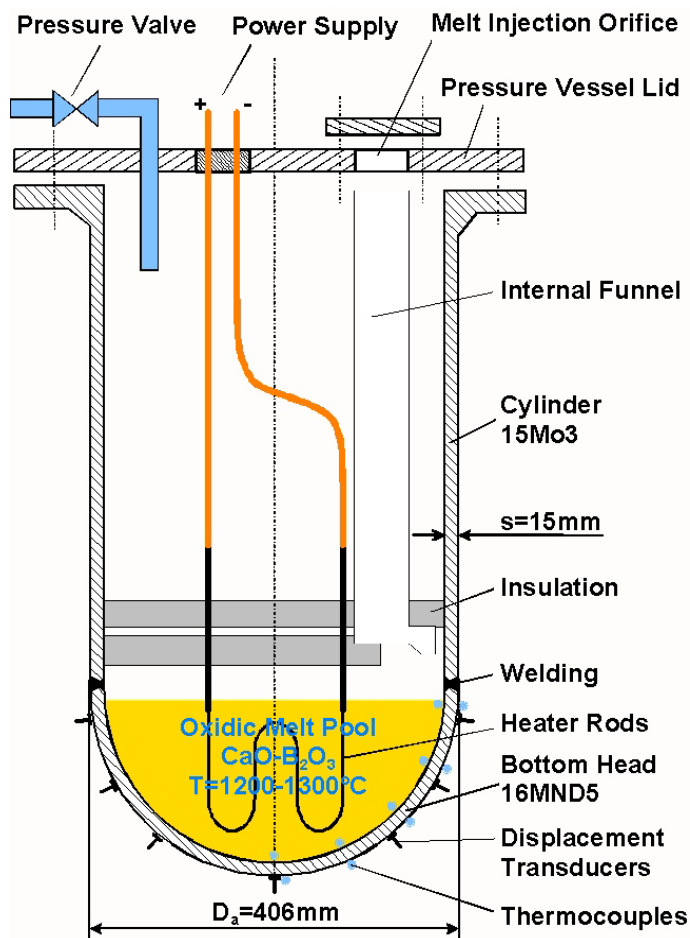# 2 The FOREVER-Experiments at KTH Stockholm

2.1 Experimental setup

Figure 2-1: Scheme of the experimental setup

The FOREVER-tests performed at the Royal Institute of Technology, Stockholm, are used for model validation purposes.

In the FOREVER-experiments the lower head of a RPV is simulated with a geometrical scale of 1:10 (cf. Figure 2-1). The vessel consists of a cylindrical part (material 15Mo3), which is welded to a hemisphere (material 16MND5 or SA-533B1). The internal radius of the vessel is 188 mm, and the wall thickness is approximately 15 mm.

Instead of a prototypic melt a simulant was used: an internally heated binary salt (70 wt.-% CaO, 30 wt.-% B_2O_3) with a melting point of approximately 1000 °C is used. The heater is made of a winded Kanthal®-rod and can provide a heating power of up to 45 kW. Using an Argon pressurization system an internal vessel pressure of up to 40 bar can be created.

The maximum melt temperature is around 1350 °C, while the maximum wall temperature is about 1000 °C and the corresponding heat flux reached ≈140 kW/m². These figures are reference values, which can change between the tests according to the power applied (cf. chapter 2.2). Die Table 2-1 gives an overview of the main thermal parameters of the FOREVER-melt.

Table 2-1: Main parameters of the melt

Density	2 500 kg/m³
Heat capacity (melt): $c_{p,l}$	2 200 J/kgK
Heat capacity (crust): $c_{p,s}$	1 530 J/kgK
Latent heat of fusion (melt)	460 kJ/kgK
Heat conductivity	3.0 W/mK
Solidus temperature	1250 K = 977 °C
Liquidus temperature	1300 K = 1027 °C
Kinematic viscosity	$4 \cdot 10^{-5}$ m²/s
Thermal diffusivity	$5.5 \cdot 10^{-7}$ m²/s
Prandtl-number	~ 70
Volumetric expansion coefficient	$9.04 \cdot 10^{-5}$ 1/K
Volumetric heat generation density (at 35 kW power)	~ 2.5 MW/m³
Max. through wall heat flux	~ 140 kW/m²
Melt pool depth in the centre	0.18 m
Melt volume	(13.5 ± 0.5) Litres

The temperature load leads in combination with a static internal pressure load to a vessel failure (creep fracture). This vessel failure should take place in the wall of the hemispherical part (i. e., below the welding) according to the prevailing temperature field. Therefore only the lower part of the vessel has been manufactured of prototypic RPV-steel (16MND5 or SA-533B1, cf. Table 2-3), while in the cylindrical part the steel 15Mo3 was used, which is weaker but made a much cheaper construction possible.

From the geometrical, thermal and mechanical parameters statements can be derived about the scalability of the experiments in comparison with the prototypic scenario. But it must be taken into account, that of course thermal, mechanical and geometrical dimensions cannot be scaled in the same way to a LWR-scenario. Table 2-2 gives an overview about the scaling factors. The FOREVER-tests have been designed in comparison to a smaller reactor than the KONVOI, which is considered here. In fact, the in-

Figure 2-2: FOREVER-vessel with displacement sensors

Figure 2-3: FOREVER-vessel at failure time

ternal radius of the prototypic reactor, for which FOREVER was scaled, was 10 times the experimental radius. The KONVOI radius dimension is larger, while the wall thickness stays at 150 mm. Therefore the membrane stress scaling can not be in line here, even without consideration of the ablation.

Table 2-2: Scaling factors of different physical dimensions between the FOREVER-experiments and a PWR of the German KONVOI type

Parameter	FOREVER	KONVOI	Scaling
Geometry			
Vessel shape	hemispherical lower head fixed to a cylinder		
Internal radius [m]	0.19	2.5	1:12.5
Wall thickness of lower head [m]	0.015	0.15	1:10
Melt volume [m^3]	0.014	32.5	1:2300
Surface-volume ratio [m^{-1}]	24	1.8	1:0.08
Material properties			
Density of wall (steel) [kg/ m^3]	7850	7850	1:1
Density of melt (corium) [kg/ m^3]	2500	8000	1:3.2
Thermal boundary conditions			
Total heat generation in the pool [MW]	0.038	29.6	1:780
volumetric heat generation density [MW/m^3]	2.7	0.91	1:0.33
internal Rayleigh-number [-]	10^{10}	10^{17}	1:10^7
wall surface heat flux at homogeneous distribution [kW/m^2]	112	500	1:4.5
theoretical temperature difference over vessel wall without melting/ablation [K]	56	2500	1:45
temperature difference over vessel wall with melting/ablation [K]	56	1200	1:21
Mechanical loading			
theoretical stress induced by the temperature difference with melting/ablation [MPa]	11	227	1:21
Weight of melt and vessel [Mg]	0.065	310	1:4800
Membrane stress by weight [MPa]	0.034	1.26	1:37
Internal pressure [MPa]	2.5	2.5	1:1
Membrane stress by pressure [MPa]	32	42	1:1.3

Figure 2-4: Cut vessel after the test

The Figures 2-2 to 2-4 show different stages of the experiment.

2.2 Analysis of the experimental data

Die Table 2-3 shows an overview of all conducted FOREVER-experiments. There have been 9 FOREVER-tests, the thermal and mechanical measurement data were digitally recorded. The measurement data of all FOREVER-experiments (except of C1 and EC3a) have been processed. As an representative example for other FOREVER-tests Figure 2-5 shows the distribution of the thermocouples in EC-3b. In Figure 2-6 the according temperature development is shown in an EXCEL-diagram. The values of failed thermocouples were omitted. The experimental data of the measured displacements of the external vessel wall of the FOREVER-vessels have been processed in an analogous way. More Figures of the experiments can be found in annex A1.

Table 2-3: Overview of all conducted FOREVER-tests (VF: vessel failure; HAZ-US: Heat Affected Zone – Upper Side)

| Test	Date	LH-Steel	Melt Level (at beginning)	Aim / Scope (VF: vessel failure)	crack shape
C1	02/1999	15Mo3	at welding line	test overall experimental setup, no VF	-
C2	06/1999	16MND5	at welding line	increased power, heater failure, no VF	-
EC1	03/2000	16MND5	above welding line	VF in HAZ-US of welding line	rough
EC2	11/2000	16MND5	below welding line	new heater design, VF clearly below welding	rough
EC3a	05/2001	16MND5	at/above welding line	penetrations, high melt level, VF at welding line	rough
EC3b	08/2001	16MND5	below welding line	penetrations, low melt level, VF below welding line	rough
EC4	02/2002	SA533B1	below welding line	no penetrations, VF below welding line + earlier than expected	sharp
EC5	06/2002	16MND5	at/below welding line	gap cooling and in-vessel melt coolability tests, no gap observed, no VF	-
EC6	12/2002	16MND5	at/below welding line		-
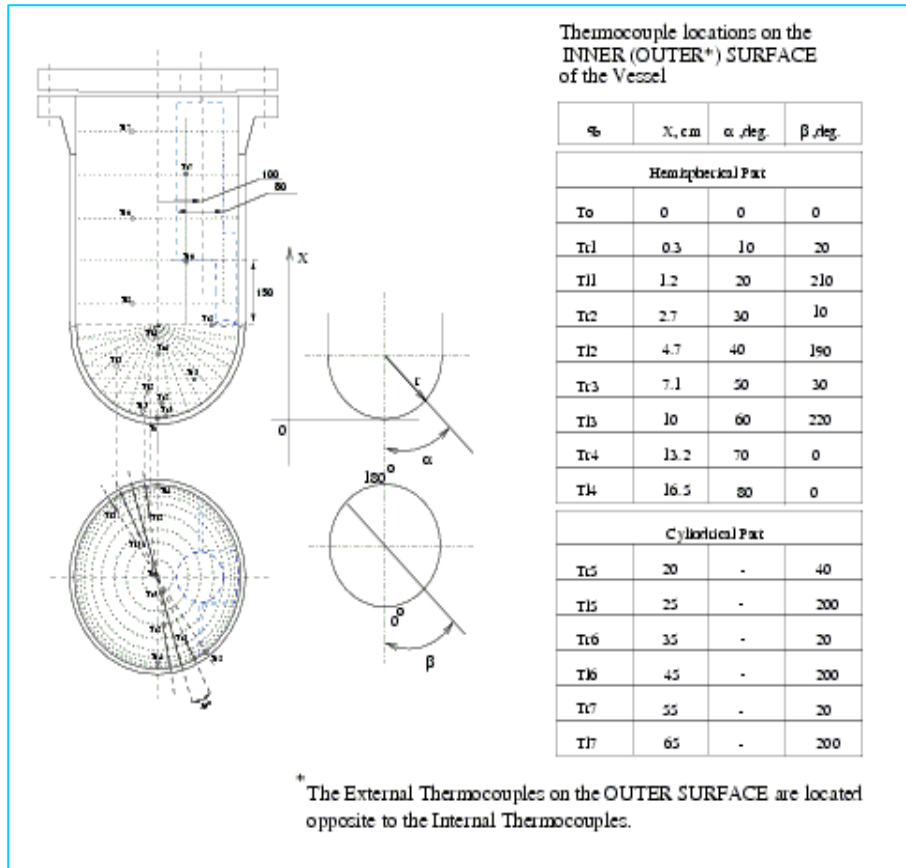
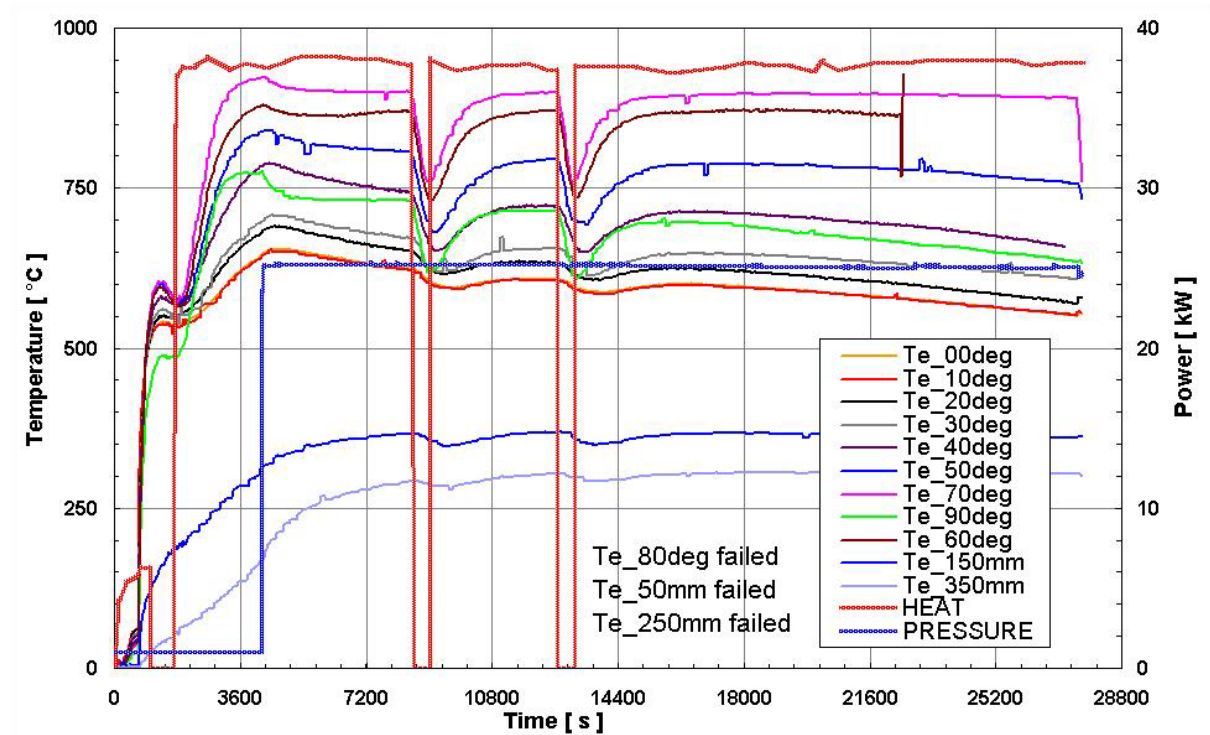**Figure 2-5**: Positions of the thermocouples in FOREVER-EC3b

Figure 2-6: Measured temperature distribution at the external vessel wall (experiment EC3b)

3   Evaluation of the temperature field
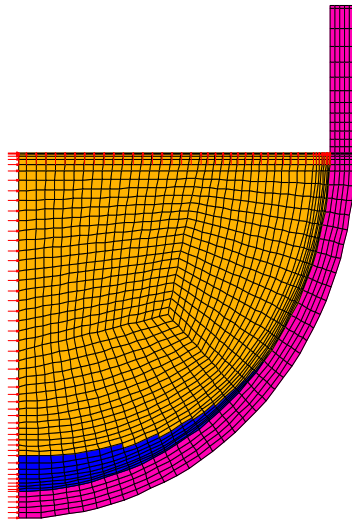
3.1   Calculation by means of CFD

Figure 3-1: Element plot of the CFD-model with different material regions
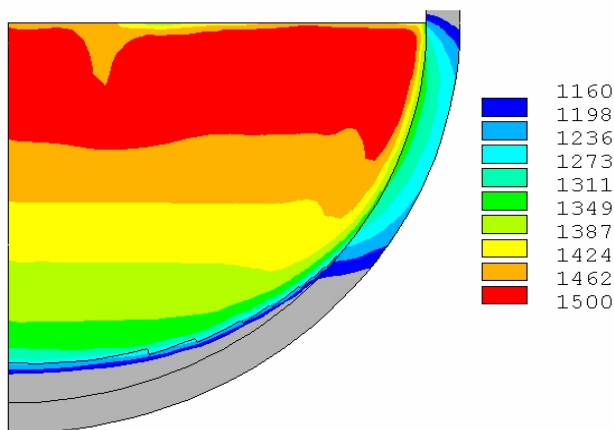

Figure 3-2: Calculated temperature field [K] for melt and vessel wall

To consider the convection of the oxidic melt and the heat transfer to the lower head, the vessel wall and the solidified or liquid melt are simulated with thermal or fluid elements. This approach has been described in a previous publication [Willschuetz et al. 2001]. Figure 3-1 shows an element plot of the CFD-model applied in the ANSYS/FLOTRAN module. The different materials are represented by different colours. The vessel wall (steel) is magenta, the region of liquid melt is orange and the crust is blue.

The time dependent thickness of the crust depends on the temperature of the corresponding elements. If the temperature of all nodes of the element lies below the solidus temperature, the material number is changed and therefore the element no longer belongs to the liquid fluid area but to the solid body area. This process goes the opposite direction in case of temperatures above the liquidus temperature. The hysteresis included in this model is physically not precise, but the numerical model is reasonable and stable and gives in comparison to the FOREVER-tests very satisfying results. A typical temperature field is given in Figure 3-2. Temperatures below 1160 K are represented in grey to emphasize the stratification in the fluid layer.

3.2   The effective conduction convection model (ECCM)

With regard to the further general model development the CFD-model has several demerits. On the one hand there are doubts that the CFD-calculations with the turbulence models available today will give reasonable results for prototypic scenarios with Rayleigh numbers of up to 10^{14} to 10^{16} [Dinh and Nourgaliev 1997]. On the other hand CFD-runs require a high effort in computational power, which makes it difficult to perform many variation calculations. Finally it was observed in prior test runs, that the CFD-model becomes unstable in case of changing geometry, as it is necessary for fully coupled simulations. It was mainly not possible to get any results in these runs.

But for the mechanical calculation the detailed temperature distribution within the melt is not needed. It is sufficient, if a model is available for the heat fluxes at the melt region boundaries by applying suitable empirical correlations.

The model described in the following is a heat conduction model with region dependent and partially anisotropic heat conductivities. It encompasses the whole FOREVER-vessel and considers radiative heat transfer between the internal structures and the combined radiation and convection on the vessel outside.
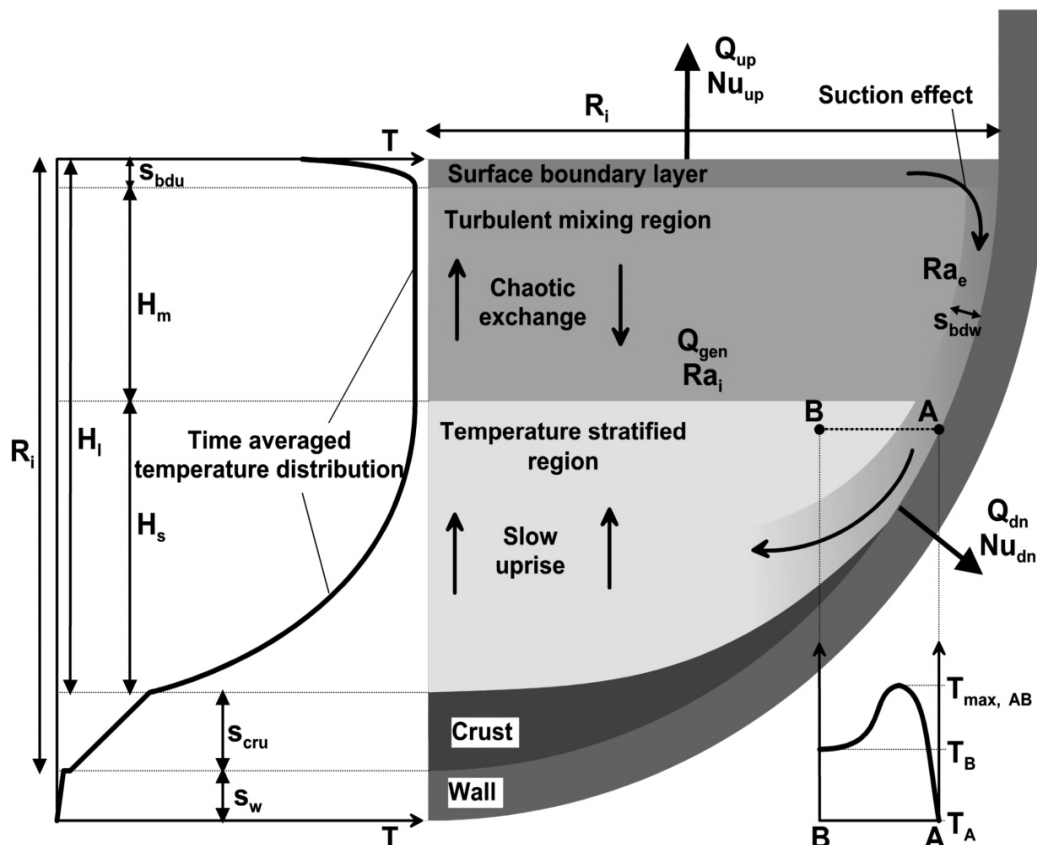
Figure 3-3: Principal scheme of a hemispherical melt pool with internal heat sources in a lower head and heat release over all surfaces and boundaries

Starting from the model development of Bui [Bui 1998] and the experimental observations and correlations of Bernaz [Bernaz 1998] and Helle [Helle und Kymäläinen 1998] it is possible to develop an Effective-Convection-Conduction-Model (ECCM). For that purpose the processes and phenomena within a hemispherical melt pool - as shown in Figure 3-3 – are analysed. The time averaged temperature distribution along the vertical symmetry axis is given in the left part of the figure. Coming from above the melt pool shows first a very thin temperature boundary layer of the thickness s_{bdu}. This thickness is enlarged for clarification. Its value can be estimated by using the upper Nusselt-number with the correlation:

$$s_{bdu} = \frac{h_l}{Nu_{up}}$$

Eq 3-1

Herein h_l is the height of the liquid melt region. The upper Nusselt-number is calculated according to the correlation of Bernaz [Bernaz 1998]:

$$\mathrm{Nu}_{up} = 0.382 \cdot \mathrm{Ra}_i^{0,233}$$ **Eq 3-2**

and the Rayleigh-number is calculated as:

$$\mathrm{Ra}_i = \frac{g \beta q_V H^5}{\nu a \lambda}$$ **Eq 3-3**

with h_l as characteristic height (H). According to this the theoretical boundary layer thickness is in the range of 2.5 mm in case of the FOREVER-arrangement and lies below 1 mm for the prototypic case. Within the boundary layer the nominal conductivity is considered. In the prototypic case a separate modelling of the boundary layer is neglected.

At the bottom side of the boundary layer the turbulent mixing region is beginning. This region is characterized in the corresponding experiments by a homogeneous temperature, if the chaotic temperature fluctuations resulting from cold plumes, which are falling down from the pool surface, are averaged over time. This region is modelled with the approach of Bui [Bui 1998] with a very high effective conductivity to account for the high turbulence mixing regime:

$$\lambda_{um} = \lambda_0(T) \cdot Nu_{up}$$ **Eq 3-4**

In case of FOREVER there are effective conductivities of several hundred W/mK. For the prototypic case the values are nearly reaching 10 000 W/mK. The height h_m of this region depends on the height of the liquid melt pool h_l as it has been observed by Bernaz:

$$h_m = 0.35 \cdot h_l$$ **Eq 3-5**

Underneath the turbulent mixing region the stratified temperature region is located, which is characterized by an approximately parabolic temperature distribution in the vertical direction (cf. Figure 3-3). The modelling of this region is performed contrary to the thermo-fluiddynamic reality, but with conservation of the experimentally observed heat fluxes at the melt pool boundaries.

The properties and relations in the lower part of the pool are influenced by the strong convective movement along the vessel wall. This convection region starts in the area of the upper free boundary layer and due to its suction effect it causes stable fluiddynamic conditions in the outer zones of the turbulent mixing zone and the upper boundary layer. The stream lines of this convection regime continue downwards, parallel to the vessel wall. At the entrance into the stratified layer a special effect is observed: due to the flow momentum of the downwards streaming fluid it can penetrate into an environment of lower temperatures and therefore higher density despite its own higher temperatures and lower density. This effect is visualized by the temperature distribution along the line between the highlighted points A and B. Starting from point A, where the lowest temperature at this considered elevation level prevails, the temperature is rising towards the centre of the downwards flowing stream. The temperature reaches a maximum in the centre of the stream, where the highest down flow velocities are to be found. From there the temperature approaches the temperature level of the corresponding elevation level. In [Bolshov et al. 2001] the temperature differences between wall (T_A) and pool (T_B) and between pool (T_B) and maximum temperature ($T_{max,AB}$) were assumed to be of the same range. The temperature level of the discussed temperature curve is in turn dependent on the elevation. The deeper the considered position of the points A and B, the deeper are the characteristic temperatures T_A, T_B and $T_{max,AB}$, whereas T_B is developing as shown to the left in the figure. Going to lower positions the shape of the curve becomes more

flat, i.e. the temperature maximum becomes relatively smaller in comparison with the overall temperature level. Concurrently the width of the stream, respective to the higher temperature bulk, becomes larger. Finally the originally strong vertical convection flow disappears horizontally in the lower part of the stratified region, as it is shown in Figure 3-3.

Within the temperature stratified region the melt is slowly rising upwards. While rising the melt heats itself up due to the internal heat sources. This process is correlated indirectly with the down flow at the vessel wall. The mass flow, that is available at each elevation level for the buoyancy, is coupled to the mass flow, that is supplied to all elevation levels below the considered elevation level. Which mass flow is fed to which elevation level, is dependent on the original flow momentum of the downward convection stream and on the density differences between the hot stream centre and the cold ambient fluid. Larger density differences cause higher buoyancy forces against the convection stream and thereby control the "swivel in" process and the distribution of the stream onto the according elevation levels. If an elevation level gets an insufficient amount of fluid, the temperature will rise due to the internal heat sources and the difference between the temperatures T_B and $T_{max, AB}$ respectively T_A becomes smaller. For this reason the density difference and the buoyancy force are reduced and the convection stream returns with its initial momentum to deeper elevation levels.

The considered processes form an equilibrium system and affect themselves. They assemble as an implicit problem, but for the ECC-Model it can be stated that the temperatures T_B and T_A are coupled to each other and therefore the heat flux into the melt pool boundary is coupled to the corresponding height position of the vertical axis. This interrelationship is accounted for in the model by an anisotropic heat conductivity. The vertical conductivity in the stratified region refers to the nominal conductivity of the fluid. But the horizontal conductivity in the lower melt pool is calculated according to Eq. 3-4 by:

$$\lambda_x = \lambda_0(T) \cdot Nu_{dn} \qquad \textbf{Eq 3-6}$$

The lower Nusselt-number is determined analogously to the upper (cf. Eq. 3-2) according to the correlation stated in [Bernaz 1998]:

$$\mathrm{Nu}_{dn} = 2.2\,\mathrm{Ra}_i^{0,174} \qquad \textbf{Eq 3-7}$$

For the FOREVER-scenario there result Nusselt-numbers of approximately 120 and a horizontal heat conductivity of 360 W/mK. For the prototypic case there are Nusselt-numbers of approximately 2 000 and conductivities of 5 000 W/m/K.

The sideward boundary layer thickness to the vessel wall is calculated analogously to the upper boundary layer thickness using the Nusselt-number and the dimension of the pool:

$$s_{bdw} = \frac{r_i}{Nu_{dn}} \qquad \textbf{Eq 3-8}$$

With this correlation, thicknesses of about 1 mm are determined for both the FOREVER and the prototypic dimensions. The conductivity within the boundary layer corresponds to the nominal temperature dependent conductivity.
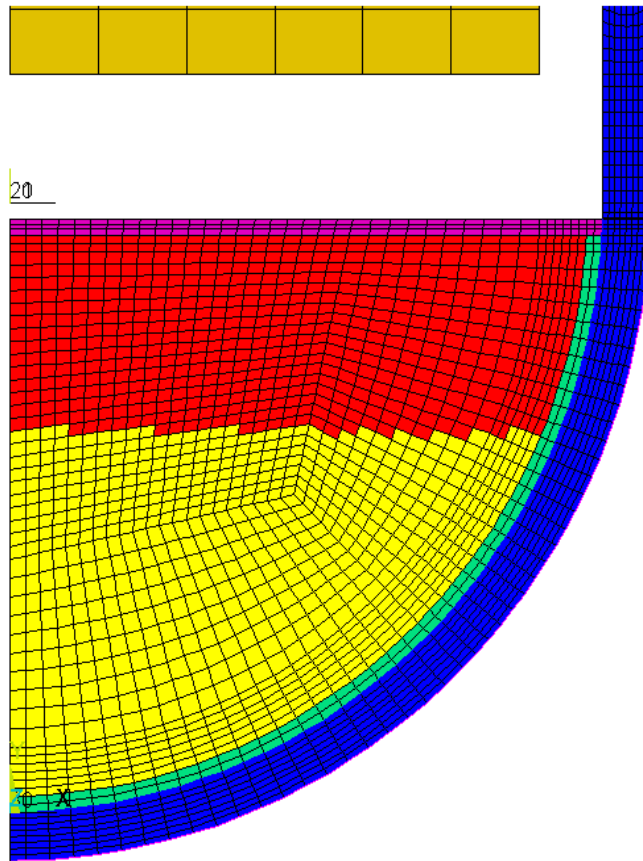
MATERIAL DISTRIBUTION after 0 s

Figure 3-4: Material zones at the beginning of a coupled calculation with ECCM

Figure 3-4 shows the initial division into the different regions for a FOREVER-calculation. In the FE-model different fixed material numbers are allocated to the according regions. In addition to the 4 melt pool regions the vessel wall is represented in blue (steel) and the insulation, which was used on top of the melt pool in the tests, is represented in orange.

The temperature stratified region is bounded at the bottom by a crust, if the according material properties and temperatures prevail. This crust has very low heat conductivities in case of oxidic melts, and therefore a very high temperature gradient is established over the crust thickness s_{cr} (cf. Figure 3-3). Between the crust and the vessel wall the formation of a gap is possible. But also without a gap there can be a thermal contact resistance. This lead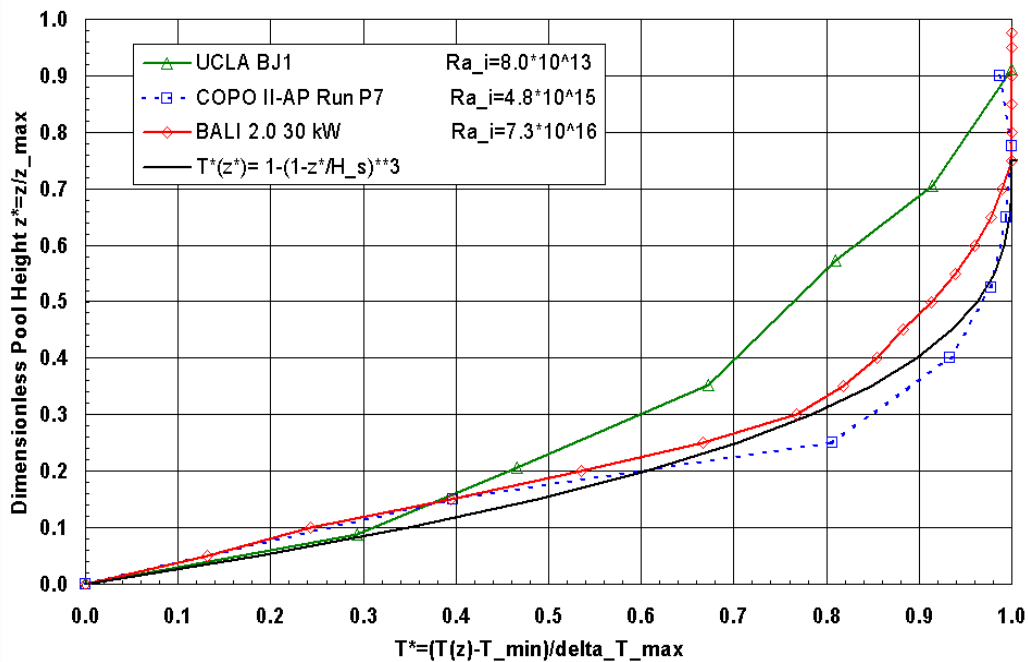s to a local temperature offset. In the considered simulations a rather small resistance of 10^{-6} K/W is modelled, because at least the post test examinations of the FOREVER-tests showed, that the melt at the bottom centre, where a crust must have been existing for the whole test, was adhering firmly to the vessel wall.

In all scenarios, also in those experiments where no crust is established at the bottom, there is an imaginary adiabatic surface with a similar shape as the upper crust surface in Figure 3-3. This surface can lie inside or outside of the crust and characterises the lower melt volume, whose internal heat generation is completely released by conduction towards the lower boundaries only. This surface is not of practical interest for CFD- or ECCM-simulations, but in some analytical works it is used for estimations of temperature and heat flux distributions.

There is a quite small temperature drop over the vessel wall thickness s_w since the heat conductivity of the steel is much higher than that of the crust. At this point the discussion about the principal temperature distribution along the vertical vessel axis is finished.

During the simulations of the temperature distributions it was observed that it is useful to consider another correlation, which became obvious in different experiments. Figure 3-5 shows the distribution of the dimensionless temperature over the dimensionless height of the fluid pool in 3 experiments [Asfia und Dhir 1996, Bernaz 1998, Helle und Kymäläinen 1998]. This height corresponds to the vertical axis of a hemispherical pool. This graphical demonstration has been chosen to make possible a comparison between different experiments with different dimensions and temperature levels.

Figure 3-5: Dimensionless temperature against dimensionless height for different experiments for the simulation of a hemispherical fluid pool with internal heat sources and dimensionless coupling equations for the ECC-model in the FE-simulation

The internal Rayleigh-number of each experiment is given in the graph. The curves confirm the temperature distribution as shown in Figure 3-3 within the stratified and the turbulent mixing region. Additionally in Figure 3-5 a function of 3rd degree is given, which corresponds especially for the experiments with the higher Rayleigh-numbers to the observed temperature distribution. z* refers to the quotient from the actual height position and total height (cf. h_l in Figure 3-3). H_s corresponds to the height of the stratified region (cf. h_s in Figure 3-3). This function is additionally used in the ECC-model, to couple the nodes along the vertical pool axis within the stratified region. The nodes within the turbulent mixing zone are also coupled, so that they have the same temperature.

The comparison of the ECC-model with a CFD-run is given in chapter 6.1. It is demonstrated that the ECC-model leads to an adequate temperature distribution within the vessel wall.

3.3 Radiation and convection at the free surfaces

Radiative heat transfer and convection at free surfaces are the mechanisms for the release of the heat generated in the melt. They provide the boundary conditions for the CFD-analysis or the ECCM-analysis. Due to the high temperatures in the considered experiments and in the prototypical scenarios the heat transfer processes are governed by the radiative transfer. It occurs inside and outside of the vessel.

The Stefan-Boltzmann-law is the starting equation for the heat transfer due to radiation:

$$q_{rad} = \sigma_{SB} \cdot \varepsilon \cdot (T_s^4 - T_{amb}^4) \qquad \textbf{Eq 3-9}$$

Herein σ_{SB} is the black body radiation constant or Stefan-Boltzmann-constant, ε is the coefficient of emission of the considered surface, T_s is the surface temperature and T_{amb} is the ambient temperature.

The heat transfer by convection at free surfaces can be described by:

$$q_{conv} = \alpha_B \cdot (T_s - T_{amb})$$ **Eq 3-10**

where the heat transfer coefficient α for gases like Argon or air lies in the range of 10 W/m²K.

In the frame of the performed investigations radiative heat transfer and convection prevail together at the free surfaces, because neither inside nor outside is vacuum. Contrary to the convective heat transfer, where the driving temperature difference has a linear influence, the temperature of a radiating surface goes with the 4th power, if the resulting heat flux is considered. Estimations according to the equations 3-9 and 3-10 show, that at surface temperatures above approximately 600 °C the heat flux by radiation becomes much stronger than the heat transfer by free convection with gases like air or Argon.

In the FE calculations all radiating surfaces are assumed to be grey. Additionally the validity of the Kirchhoff law is supposed: the emissivity and the absorbtivity are not dependent on the wavelength and they are equal.

The largest uncertainty for the modelling of the heat radiation results from the uncertainty about the emissivity and the absorbtivity. At the same time the emissivity of the radiating surfaces has a strong impact onto the distribution of the heat fluxes inside and outside of the vessel. For this reason the resulting temperatures and therefore indirectly the mechanical behaviour and the failure time are coupled to the emissivity. On account of this the coefficients for the radiation model are to be considered as essential material properties. From variation calculations for the FOREVER tests it could be concluded that the emissivity coefficient for the oxidized respective the carburised external vessel surface was in the range between 0.7 and 0.8. For the vessel inside the coefficient could have been slightly higher (0.8 to 0.9). In the standard calculations therefore a value of 0.75 was applied outside and a value of 0.85 was used inside.

3.4 Thermal material properties

The material properties used for the thermo-fluiddynamic calculations like viscosity, density and heat conductivity are provided to the ANSYS-code for the necessary materials in a temperature range from 275 to 3000 K. For those ranges where no data were available the properties were interpolated or estimated and compared with similar materials. This applies especially to the range above the solidus temperature of the steel. The same applies for the oxidic melt, the insulation material and the Argon gas used in the FOREVER-tests. Indeed the material data for the last-mentioned materials are not as detailed and not as important as for the steel 16MND5. But it is not expected that there are any negative consequences to the reliability of the calculated thermal results.

The data for the prototypic melt are oriented to values in [Kolev 1996] and represent a simplified material behaviour. A detailed modelling of the single melt components, possible mixing, demixing or chemical processes was on the one hand not possible due to missing experimental data. On the other hand it would have made the overall model "overcomplicated", i.e. it would make it rather complicated to get any solution and if a solution is obtained, it is difficult to distinguish the effects to their reasons.

In the calculations a homogeneously mixed melt is simulated, whose properties are mainly described according to uranium dioxide, because uranium dioxide will be the prevailing component in the corium pool. Solely for the solidification range the tem-

perature levels have been lowered intentionally, because this should account for the formation of eutectics and additionally lead to a conservative loading of the vessel wall since liquid melt allows a much higher heat flux than solidified melt.

Table 3-1 gives an overview of some typical material properties. The complete temperature dependent material data are prepared for the macro language APDL (ANSYS Parametric Design Language) of the FE-code. The listed latent heats of fusion are modelled as fictitious heat capacities over the assumed solidification interval.

Table 3-1: Thermo-fluiddynamic properties of the FOREVER-melt and the assumed prototypic corium

Material property	Symbol/Unit	Test melt	Corium
Solidus temperature	T_S [K]	1 250	1 950
Liquidus temperature	T_L [K]	1 300	2 000
Latent heat of fusion	h_m [kJ/kg]	460	260
Reference temperature for the following properties:	T [K]	1 400	2 200
Density	ρ [kg/m^3]	2 500	8 000
Volumetric expansion coefficient	β [1/K]	$9.04 \cdot 10^{-5}$	$1.0 \cdot 10^{-4}$
Heat conductivity	λ [W/m K]	2	2.5
Heat capacity	c_p [J/kg K]	2 200	530
Dynamic viscosity	ν [Pa s]	0.1	0.0045

4 Structure mechanical modelling

4.1 Axis symmetric mesh of the vessel

The lower vessel head is modelled with structural elements considering the material behaviour at high temperatures. For this purpose the FE code ANSYS® is used (revisions 6.1, 7.1 and 8.1) with supplemental routines (UPFs) for creep and damage modelling.

The mesh is – like in the thermal model – axisymmetric. The node positions and the element geometries of the vessel wall exactly correspond to those of the thermal model. Thus an easy transfer of the temperature loads from the thermal model is possible.

The number of elements over the wall thickness varies on the meridian line. In the strongly loaded range of the hot focus 8 element layers are used in case of FOREVER simulations; in the moderately loaded ranges above and below the hot focus 4 element layers are used. The ANSYS element type PLANE182 is used for meshing.

4.2 Loads

The following loads are considered within the mechanical calculation:

- Internal pressure (in the case of the FOREVER experiments ca. 25 bar)

- Gravity (dead weight of melt and vessel)

- Temperature field in the vessel wall

The internal pressure and the gravity loads cause primary stresses, which are not relieved by the deformation of the vessel wall, but are even increased due to wall thickness reduction. In the case of the FOREVER geometry, the contribution of the weight to the primary stresses is negligible compared to the contribution of the internal pressure (cf. Table 2-2).

Unlike to this the temperature gradients cause secondary stresses, which is relieved by viscoplastic deformation. Since in the FOREVER tests the maximum temperature in the vessel wall is below the melting temperature of steel, the vessel would not fail without internal pressure.

Contrary to this, in the prototypic scenario the vessel failure could happen also without internal pressure, because the contribution of the weight is significant. Moreover the maximum temperature is above melt temperature of steel.

In the FE model, the internal pressure is applied as a surface load. It has to be regarded that two phenomena lead to an increasing primary stress with ongoing deformation: 1. the enlargement of the surface subjected to pressure load and 2. the reduction of the wall thickness.

The weight of the vessel is considered by an accelerated reference coordinate system while the weight of the melt is modelled as an equivalent surface load. The temperature field is sequentially transferred from the transient thermal calculation (chapter 3; see also chapter 5 - coupling).
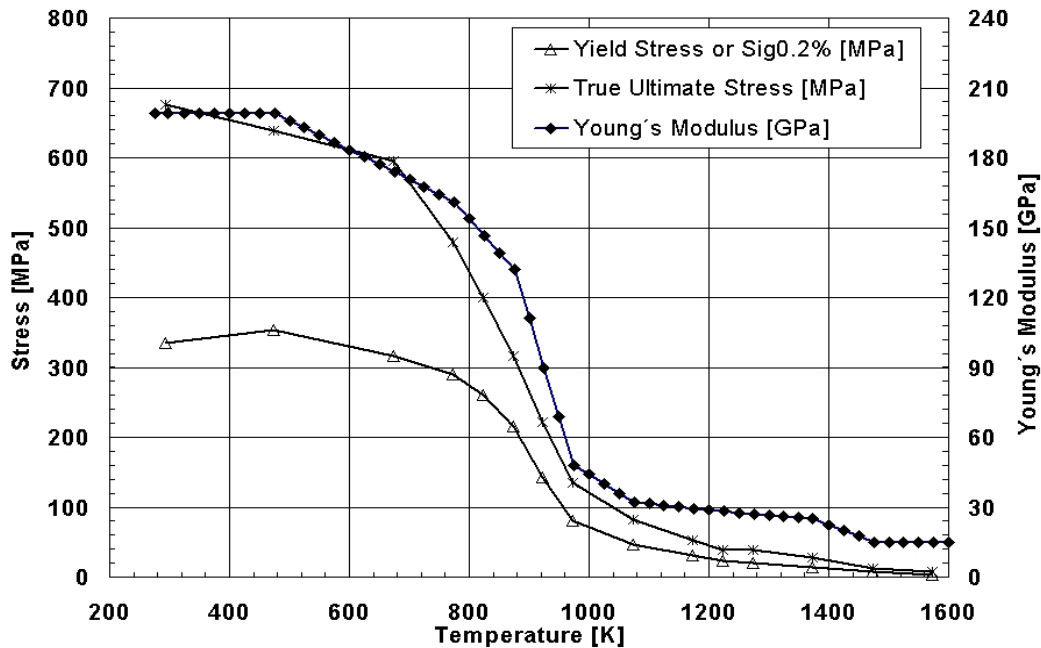
Figure 4-1: Yield strength, true ultimate stress and Young's modulus (right axis) versus temperature

4.3 Elastic and viscoplastic material properties

Three parts of the deformation of the material have to be taken into account: elastic deformation, creep and plasticity. The creep (also denoted as viscoplasticity) is a time dependent process coming into play at elevated temperatures (in case of steel above 500 °C), however, occurring at arbitrary low stresses. Contrary to this the plasticity is a prompt process – occurring only above a stress threshold (yield strength). Plasticity can occur already at room temperature, however, the yield strength increases with decreasing temperatures. Both deformation parts can occur simultaneously. They are coupled via the geometrical softening (e.g. by increase of primary stress due to deformation induced wall thickness reduction).

The elastic deformation is small compared to the creep and plastic deformation, but it causes the stresses. The elastic material properties are assumed to be isotropic and can therefore completely be characterised by the temperature dependent Young's modulus and the constant Poisson number (v=0.3). The Figure 4-1 shows the temperature dependent properties Young's modulus, yield strength and tensile strength for the material 16MND5.

The generation of the plastic and viscoplastic material data base is premised on the experimental results of the REVISA project of the 4th framework programme [Mongabure and Desmet 1999; Ikonen 1999]. In this project as well tensile tests as creep tests were performed in the temperature range from 600 °C to 1300 °C for the French RPV steel 16MND5.

In these tests the nominal stresses (tension force divided by initial cross section) and the nominal strain (increase of length divided by initial length) are measured. In the FE simulation the true stress and strain are needed. The conversion is done according to the well known equations:

$$\varepsilon = \varepsilon^{tr} = \ln(1 + \varepsilon^{nom})$$

$$\sigma = \sigma^{tr} = \sigma^{nom} \cdot (1 + \varepsilon^{nom})$$

Eq 4-1

In the following we refer to the true values if the index "tr" is not explicitly given.

4.3.1 Generation of the creep data base

The creep behaviour of steel is usually described by analytical formulae (creep laws) containing a number of free parameters depending on the approach [Altstadt, 2003]. The following creep law is often used:

$$\dot{\varepsilon} = d_1 \cdot \sigma^{d_2} \cdot \varepsilon^{d_3} \cdot \exp\left[-\frac{d_4}{T}\right]$$

Eq 4-2

In this equation the strain rate $\dot{\varepsilon}$ is expressed in terms of true stress σ, the accumulated true creep strain ε and the current temperature T. Since the exponent d_3 is negative for most of the materials, equation 4-2 is called strain hardening representation ($\ddot{\varepsilon} < 0$). The coefficients ($d_1 \ldots d_4$ in Eq. 4-2) are used to adapt the creep laws to a number of creep tests, each performed at constant nominal load and temperature. However, in practice it is often difficult to achieve a satisfying adjustment for a wide range of temperatures and stresses with only one set of coefficients. Instead it appears that the coefficients itself are dependent on the temperature or on the stress level. An additional drawback of the analytical description (Eq 4–2) is connected with the fact, that only the primary creep stage can be described with one coefficient d_3. However, it is necessary to capture also the secondary creep stage ($\ddot{\varepsilon} = 0$) and the tertiary creep stage ($\ddot{\varepsilon} > 0$) in the model.

Therefore an extension of creep modelling was developed for the FE-Code ANSYS® [Altstadt 2003, Altstadt und Mössner 2000]. This development is based on the User Programmable Features (UPF) of ANSYS allowing the link of additional FORTRAN routines to the code. The Compaq® Visual Fortran Compiler (Rev. 6.6A) was used for programming and for generating the customized ANSYS-executable on a Windows2000® platform.

The realisation of the creep modelling starts from a generalised form of the strain hardening representation:

$$\dot{\varepsilon}^{cr} = f(\varepsilon^{cr}; \sigma; T)$$

Eq 4-3

This is valid for primary, secondary und tertiary creep. The relation Eq (4–3) is transferred into the ANSYS database by means of a number of discrete pairs of the form

$$\begin{bmatrix} \varepsilon_{(1)} & \dot{\varepsilon}_{(1)} \\ \vdots & \vdots \\ \varepsilon_{(n)} & \dot{\varepsilon}_{(n)} \end{bmatrix}_{T=cnst;\sigma=const}$$

Eq 4-4

Several of such sets for different temperature and stress levels can be combined, originating directly from creep tests or generated by a combination of different analytical formulas for primary, secondary und tertiary creep. The complete creep data base then is as follows:

$$
\begin{array}{|ccc|c|ccc|}
\hline
& T_1 & & \cdots & & T_K & \\
\hline
\sigma_{1,1} & \cdots & \sigma_{1,M1} & \cdots & \sigma_{K,1} & \cdots & \sigma_{K,MK} \\
\hline
\varepsilon_{1,1}^{frac} & \cdots & \varepsilon_{1,M1}^{frac} & \cdots & \varepsilon_{K,1}^{frac} & \cdots & \varepsilon_{K,MK}^{frac} \\
\hline
N_{1,1} & \cdots & N_{1,M1} & \cdots & N_{K,1} & \cdots & N_{K,MK} \\
\hline
(\varepsilon_{1,1,1};\dot{\varepsilon}_{1,1,1}) & \cdots & (\varepsilon_{1,M1,1};\dot{\varepsilon}_{1,M1,1}) & \cdots & (\varepsilon_{K,1,1};\dot{\varepsilon}_{K,1,1}) & \cdots & (\varepsilon_{K,MK,1};\dot{\varepsilon}_{K,MK,1}) \\
\vdots & \ddots & \vdots & \ddots & \vdots & \ddots & \vdots \\
(\varepsilon_{1,1,N};\dot{\varepsilon}_{1,1,N}) & \cdots & (\varepsilon_{1,M1,N};\dot{\varepsilon}_{1,M1,N}) & \cdots & (\varepsilon_{K,1,N};\dot{\varepsilon}_{K,1,N}) & \cdots & (\varepsilon_{K,MK,N};\dot{\varepsilon}_{K,MK,N}) \\
\hline
\end{array}
$$

Eq 4-5

The first index refers to the temperature, the second index to the stress and the third to the strain. K is the number of temperature levels, MK the number of stress levels within the K-th temperature level and N the number of strain rate-strain pairs for the m-th stress level within the K-th temperature level.

The UPF routine user01 is used to realize the creep data input into ANSYS. The data must be provided by the user as a set of ASCII files (for each temperature-stress level one file). To realize the calculation of the creep strain increment according to the non-standard creep law, the UPFs usercr.f (explicit algorithm) and usercreep.f (implicit algorithm) were modified and linked to the customized ANSYS executable. In these routines the scalar creep strain increment $\Delta\varepsilon^{cr} = \dot{\varepsilon}^{cr} \cdot \Delta t$ is determined from the creep data base by non-linear interpolation:

$$
\begin{aligned}
\Delta\varepsilon^{cr} = \big[& w_1 \cdot \dot{\varepsilon}_{L;L;L} + w_2 \cdot \dot{\varepsilon}_{L;L;H} + w_3 \cdot \dot{\varepsilon}_{L;H;L} + w_4 \cdot \dot{\varepsilon}_{L;H;H} \\
+ & w_5 \cdot \dot{\varepsilon}_{H;L;L} + w_6 \cdot \dot{\varepsilon}_{H;L;H} + w_7 \cdot \dot{\varepsilon}_{H;H;L} + w_8 \cdot \dot{\varepsilon}_{H;H;H} \big] \cdot \Delta t
\end{aligned}
$$

Eq 4-6

where the weight factors w_1 to w_8 are determined as follows:

$$w_1 = \frac{(e^{-q_L/T_H} - e^{-q_L/T}) \cdot (\sigma_{L;H}^{r_L} - \sigma^{r_L}) \cdot (\varepsilon_{L;L;H} - \varepsilon)}{(e^{-q_L/T_H} - e^{-q_L/T_L}) \cdot (\sigma_{L;H}^{r_L} - \sigma_{L;L}^{r_L}) \cdot (\varepsilon_{L;L;H} - \varepsilon_{L;L;L})}$$

$$w_2 = \frac{(e^{-q_L/T_H} - e^{-q_L/T}) \cdot (\sigma_{L;H}^{r_L} - \sigma^{r_L}) \cdot (\varepsilon - \varepsilon_{L;L;L})}{(e^{-q_L/T_H} - e^{-q_L/T_L}) \cdot (\sigma_{L;H}^{r_L} - \sigma_{L;L}^{r_L}) \cdot (\varepsilon_{L;L;H} - \varepsilon_{L;L;L})}$$

$$w_3 = \frac{(e^{-q_H/T_H} - e^{-q_H/T}) \cdot (\sigma^{r_L} - \sigma_{L;L}^{r_L}) \cdot (\varepsilon_{L;H;H} - \varepsilon)}{(e^{-q_H/T_H} - e^{-q_H/T_L}) \cdot (\sigma_{L;H}^{r_L} - \sigma_{L;L}^{r_L}) \cdot (\varepsilon_{L;H;H} - \varepsilon_{L;H;L})}$$

$$w_4 = \frac{(e^{-q_H/T_H} - e^{-q_H/T}) \cdot (\sigma^{r_L} - \sigma_{L;L}^{r_L}) \cdot (\varepsilon - \varepsilon_{L;H;L})}{(e^{-q_H/T_H} - e^{-q_H/T_L}) \cdot (\sigma_{L;H}^{r_L} - \sigma_{L;L}^{r_L}) \cdot (\varepsilon_{L;H;H} - \varepsilon_{L;H;L})}$$

$$w_5 = \frac{(e^{-q_L/T} - e^{-q_L/T_L}) \cdot (\sigma_{H;H}^{r_H} - \sigma^{r_H}) \cdot (\varepsilon_{H;L;H} - \varepsilon)}{(e^{-q_L/T_H} - e^{-q_L/T_L}) \cdot (\sigma_{H;H}^{r_H} - \sigma_{H;L}^{r_H}) \cdot (\varepsilon_{H;L;H} - \varepsilon_{H;L;L})}$$

$$w_6 = \frac{(e^{-q_L/T} - e^{-q_L/T_L}) \cdot (\sigma_{H;H}^{r_H} - \sigma^{r_H}) \cdot (\varepsilon - \varepsilon_{H;L;L})}{(e^{-q_L/T_H} - e^{-q_L/T_L}) \cdot (\sigma_{H;H}^{r_H} - \sigma_{H;L}^{r_H}) \cdot (\varepsilon_{H;L;H} - \varepsilon_{H;L;L})}$$

$$w_7 = \frac{(e^{-q_H/T} - e^{-q_H/T_L}) \cdot (\sigma^{r_H} - \sigma_{H;L}^{r_H}) \cdot (\varepsilon_{H;H;H} - \varepsilon)}{(e^{-q_H/T_H} - e^{-q_H/T_L}) \cdot (\sigma_{H;H}^{r_H} - \sigma_{H;L}^{r_H}) \cdot (\varepsilon_{H;H;H} - \varepsilon_{H;H;L})}$$

Eq 4-7

$$w_8 = \frac{(e^{-q_H/T} - e^{-q_H/T_L}) \cdot (\sigma^{r_H} - \sigma_{H;L}^{r_H}) \cdot (\varepsilon - \varepsilon_{H;H;L})}{(e^{-q_H/T_H} - e^{-q_H/T_L}) \cdot (\sigma_{H;H}^{r_H} - \sigma_{H;L}^{r_H}) \cdot (\varepsilon_{H;H;H} - \varepsilon_{H;H;L})}$$

The quantities without index are the actual values of the current element integration point. The indexed quantities are the values from the creep data base Eq. (4-5). They form the smallest intervals which the actual quantities are enclosed in. The meaning of the indices is L: low bound (largest data base value which is smaller than the actual integration point value) and H: high bound (smallest data base value which is greater than the actual integration point value). The first index refers to the temperature, the second index to the stress and the third to the strain.

$$T_L \leq T \leq T_H$$
$$\{\sigma_{L;L}; \sigma_{H;L}\} \leq \sigma \leq \{\sigma_{L;H}; \sigma_{H;H}\}$$
$$\{\varepsilon_{L;L;L}; \varepsilon_{L;H;L}; \varepsilon_{H;L;L}; \varepsilon_{H;H;L}\} \leq \varepsilon \leq \{\varepsilon_{L;L;H}; \varepsilon_{L;H;H}; \varepsilon_{H;L;H}; \varepsilon_{H;H;H}\}$$

Eq 4-8

The parameters r and q follow from:

$$q_L = \frac{\ln(\dot{\varepsilon}_{H;L;L}/\dot{\varepsilon}_{L;L;L})}{1/T_L - 1/T_H} \quad ; \quad q_H = \frac{\ln(\dot{\varepsilon}_{H;H;L}/\dot{\varepsilon}_{L;H;L})}{1/T_L - 1/T_H}$$

$$r_L = \frac{\ln(\dot{\varepsilon}_{L;H;L}/\dot{\varepsilon}_{L;L;L})}{\ln(\sigma_{L;H}/\sigma_{L;L})} \quad ; \quad r_H = \frac{\ln(\dot{\varepsilon}_{H;H;L}/\dot{\varepsilon}_{H;L;L})}{\ln(\sigma_{H;H}/\sigma_{H;L})}$$

Eq 4-9

More details can be found in [Willschütz et al 2001] and [Altstadt 2003].

Describing the creep behaviour, the most difficult part is the tertiary creep stage. The creep laws, or alternatively the creep data base, in FE algorithms must be based on true stress and true strain. However, usual creep tests are load controlled (force applied to the tension bar is constant). Consequently, the true stress is not constant during the test because of the uniform reduction of the cross section in the early test

stage and because of the necking later on. The increasing creep strain rate observed in the late test phase is a consequence of two effects:

1. geometrical creep acceleration due to reduction of cross section and necking

2. decreasing material creep resistance due to micro structural changes (e.g. micro cracks, creep cavities)

In FE-models, the geometrical creep acceleration is automatically considered if the large strain option is activated (ANSYS command: NLGEOM,ON). To describe the material tertiary creep there are two basic options: i) to use a creep law or a creep data base with $\ddot{\varepsilon} > 0$ (e.g. for $d_3 > 0$ in the case of Eq. 4-2); ii) to use a creep strain rate that is coupled to the material damage. In the second option Eq. 4-3 is modified to:

$$\dot{\varepsilon}^{cr} = \tilde{f}(D; \varepsilon^{cr}; \sigma; T) = \frac{1}{1-D} \cdot f(\varepsilon^{cr}; \sigma; T) \qquad \textbf{Eq 4-10}$$

with D being the damage (section 4.4). Using the creep data base, the creep strain increment is evaluated according to:

$$\Delta\varepsilon^{cr} = \frac{1}{1-D} \cdot \left[w_1 \cdot \dot{\varepsilon}_{L;L;L} + w_2 \cdot \dot{\varepsilon}_{L;L;H} + w_3 \cdot \dot{\varepsilon}_{L;H;L} + w_4 \cdot \dot{\varepsilon}_{L;H;H} \right.$$
$$\left. + w_5 \cdot \dot{\varepsilon}_{H;L;L} + w_6 \cdot \dot{\varepsilon}_{H;L;H} + w_7 \cdot \dot{\varepsilon}_{H;H;L} + w_8 \cdot \dot{\varepsilon}_{H;H;H} \right] \cdot \Delta t \qquad \textbf{Eq 4-11}$$

In this case the creep data base itself (Eq. 4-5) does not consider tertiary creep, but the continuation of the secondary stage ($\ddot{\varepsilon} = 0$) is assumed; the material creep acceleration is realized by the damage coupling, i.e. by the factor $(1-D)^{-1}$.

4.3.2 Modelling of the plastic material behaviour

For the plasticity the multi-linear isotropic hardening model of the ANSYS code is used (MISO-option). For 12 temperature levels from room temperature to 1600 K the plasticity is represented by a curve consisting of 6 linear sections. The stress-strain curves of the tensile tests of the REVISA project are used for this purpose.

However, some modifications of the measured curves are necessary. The plasticity in the FE model is a prompt process as mentioned above. Contrary to this the tensile tests in the REVISA tests were performed at a constant nominal strain rate of $\dot{\varepsilon} = 1\% \cdot \min^{-1}$ for tests below 1000 °C (test specimen length: 50 mm, displacement rate: 0.5 mm/min) and $\dot{\varepsilon} = 1.18\% \cdot \min^{-1}$ for 1000 °C and higher (test specimen length: 85 mm, displacement rate: 1.0 mm/min). This is too slow for a separation of creep and plasticity. At these low strain rates the duration of the tensile test is relatively high and therefore a significant creep strain will be present at rupture time. This is especially true for higher temperatures. Thus, the tensile test is partly a stress relaxation test [Willschütz und Altstadt 2002]. In the creep tests significantly higher strain rates can be observed than the values for the tensile tests mentioned above. As a consequence of this, the maximum true stresses observed in the creep test are even higher than the tensile strength observed in the tensile test at the same temperature, since the deformation resistance increases with higher strain rates.

Therefore the following constructions procedure is used for the stress-strain curves to be used in the FE model:

- Point 1: true strain $\varepsilon = 0.0005$ assuming a pure elastic deformation, i.e. the according stress follows from $\sigma_{el}(T) = E(T) \cdot 0.0005$.

- Point 2: Stress at strain of $\varepsilon = 0.002$ from the true stress-strain curve of the tensile test

- Point 3: Stress at strain of $\varepsilon = 0.01$ from the true stress-strain curve of the tensile test

- Point 4: Stress at strain of $\varepsilon = 0.05$ from the true stress-strain curve of the tensile test

- Point 5: Highest true stress observed before necking (either from the creep test or from the tensile test) at the according true strain (uniform elongation)

- Point 6: Maximum stress at the fracture strain observed in the tensile test. Since the amount of necking cannot be seen from the experimental data, the true fracture strain is determined under the assumption of an uniform elongation (Eq 4-1). The maximum stress follows from a slight increase of the stress value used for point 5.

As an example Figure 4-2 represents the relations at 800 °C. The dotted black curve (▪) shows the modelled stress-strain relation of the code. The modelled tensile strength of about 120 MPa is significantly higher than tensile strength observed in the REVISA tensile test (ca. 80 MPa), because the highest true stress in the creep test was about 120 MPa (see curve "REVISA 65MPa Creep Test" in Figure 4-2). In this example the creep strain rate was about $\dot{\varepsilon} = 0.01\,\mathrm{min}^{-1}$ at a true strain of about $\varepsilon = 0.25$. This corresponds very well with the intersection point "A" shown in Figure 4-2. Shortly before the rupture of the creep specimen a creep strain rate of about $\dot{\varepsilon} = 0.1\,\mathrm{min}^{-1}$ was reached. The corresponding figures of the stress-strain curves of the other temperature levels are shown in the appendix (Figures A-14 to A-26).
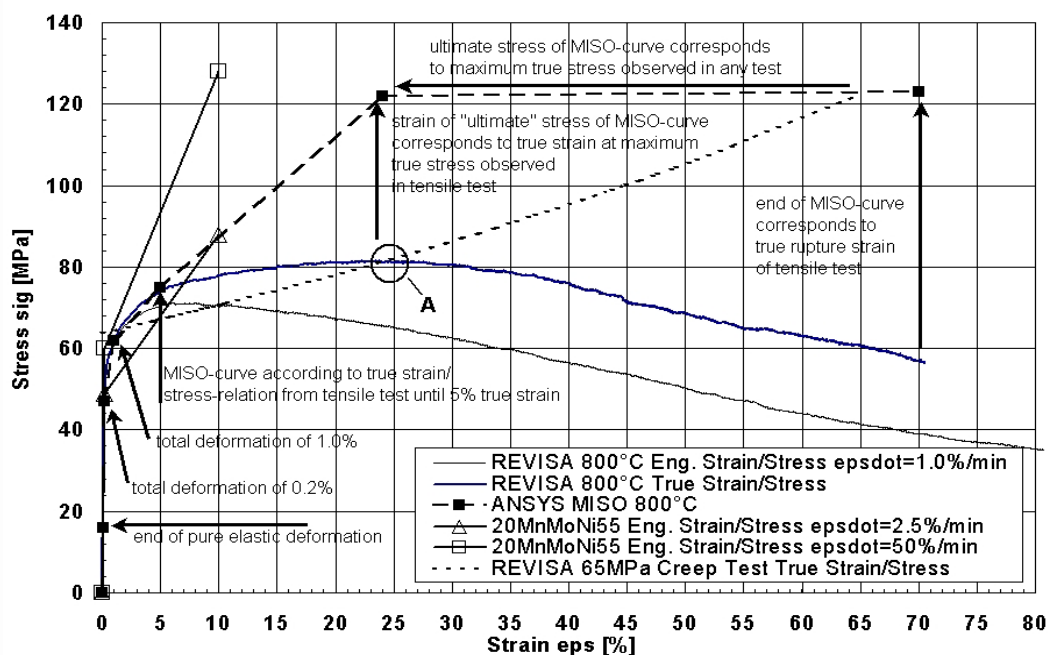
Figure 4-2: Construction of the stress-strain curve at T = 800 °C

4.3.3 Validation of the material data base

The material data base has been gradually validated during and after its development and implementation by:

i)   the application to each of the REVISA tests from 600 °C was done in parallel to the development of the data base (1D-validation for 16MND5).

ii)   the application to the RUPTHER-14 test (2D, small scale, 16MND5) and

iii)   the application to the MPA-Meppen test (2D, large scale, 20 MnMoNi 5 5)

Within the validation it was also investigated, whether there is a significant difference between the RPV steels 16MND5 (French standard) and 20 MnMoNi 5 5 (German standard) – which are chemically very similar – or whether it is possible to use one material data base for these materials. Both steels are oriented to the ASTM standard for the American RPV steel SA 533 B. The chemical compositions are equivalent, while the heat treatments exhibit slight differences. Table 4-1 gives an overview of the chemical compositions. EC-3b und EC-4 are the FOREVER tests from Table 2-3. The table also contains the materials of the LHF and OLHF tests performed in the U.S.A. [Chu et al 1999, Mongabure 2000]. All heats comply with the ASTM standard, with the exception of a slightly increased Ni content in case of 16MND5 and 20 MnMoNi 5 5.

Table 4-1: Chemical composition of RPV steels according to the ASTM-standard and in different experiments

Weight-%	C	Si	Mn	P	S	Cr	Ni	Mo	Cu
SA 533 B (ASTM min)	0.000	0.130	1.070	0.000	0.000	…	0.370	0.410	…
SA 533 B (ASTM max)	0.250	0.450	1.620	0.035	0.035	…	0.730	0.640	…
RUPTHER (16MND5)	0.170	0.251	1.440	0.004	0.002	0.200	0.750	0.510	0.010
EC-3b (16MND5)	0.138	0.230	1.190	0.009	0.004	0.251	0.523	0.466	0.091
EC-4 (SA 533 B)	0.155	0.252	1.120	0.012	0.001	0.046	0.417	0.424	0.028
Meppen (20MnMoNi5.5)	0.210	0.240	1.480	0.008	0.005	0.200	0.800	0.520	0.070
LHF (SA 533 B)	0.170	0.200	1.220	0.006	0.010	0.100	0.670	0.550	0.009
OLHF(SA 533 B)	0.172	0.286	1.290	0.013	0.001	0.046	0.520	0.490	0.021

In Table 4-2 the heat treatment data and the mechanical properties at room temperature are given for the heats of the RUPTHER experiment [Mongabure und Desmet 1999] and of the MPA-Meppen experiment [Obst et al 1988].

Table 4-2: Heat treatment and mechanical properties at RT for 16MND5 and 20 MnMoNi 5 5; WC – Water cooling , AC – Air cooling, OC – Oven cooling

Material	16MND5 (RUPTHER)	20 MnMoNi5 5 (MPA Meppen)
Quenching	885 °C (8.7 h); WC	920°C (6.5h); WC
Tempering	644 °C (9 h); AC	657 °C (9 h); AC
Stress relieving	623 °C (6.3 h); OC	no information
Microstructure	bainitic	bainitic
Yield strength (at RT)	473 ... 488 MPa	567 ... 624 MPa
Tensile strength (at RT)	620 ... 724 MPa	635 ... 726 MPa
Elongation (at RT)	25%	22%
Necking (bei RT)	73%	64 ... 69 %

Due to the different heat treatments the strength of 16MND5 is slightly lower than that of 20 MnMoNi 5 5, as a countermove 16MND5 exhibits a slightly higher ductility.

The post test calculations of the creep tests are shown in the appendix A2. In consideration of the large scatter in the creep behaviour even within specimens of the same heat attention was paid to the fact that the creep data base describes all creep tests of the REVISA program conservatively with respect to the failure time.

Figure 4-4 shows two creep tests of the MPA-Meppen experiment and a comparable creep test of the REVISA project as well as the according simulation using the creep data base. It can be seen that the scatter within the same heat is in the same order of magnitude as the difference between 16MND5 and 20 MnMoNi 5 5.

As a matter of principle, individual creep tests can be simulated with high agreement if the creep data base is adjusted accordingly. This is demonstrated in Figure 4-4. The tertiary creep stage was modelled by different approaches (ref. to section 4.3.1). The best agreement could be obtained by the damage coupling (Eq 4-10, light blue curve). It can also be seen that only the geometrical creep acceleration is not sufficient for describing the tertiary creep stage correctly (green curve). With respect of the mentioned large scattering of the experimental creep curves, the exact adjustment of all REVISA tests was not intended when developing the creep data base.
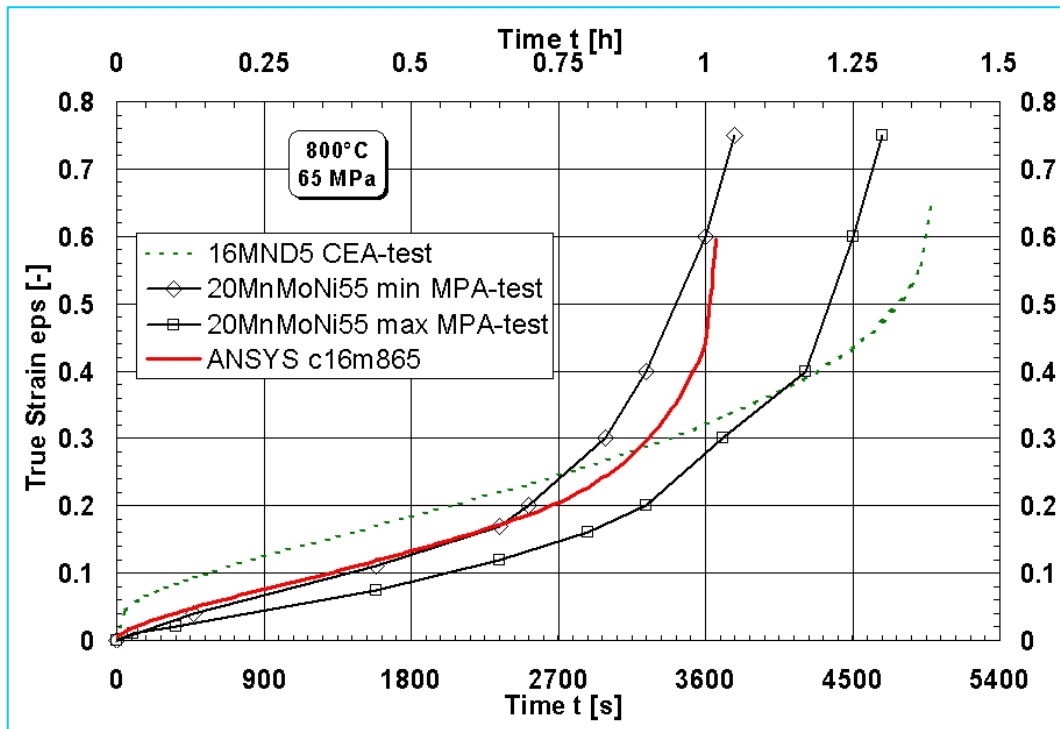
Figure 4-2: Creep tests for 20MnMoNi55 and 16MND5 and post test calculation with ANSYS.
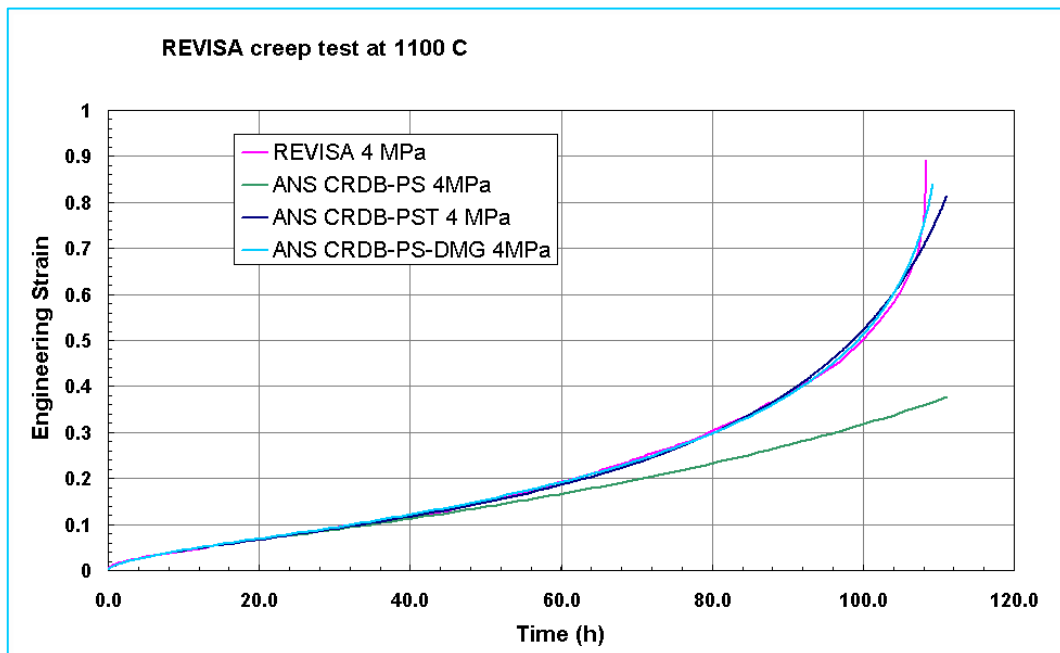
Figure 4-3: Creep test at 1100 °C and nominal stress 4 MPa of the REVISA project and ANSYS-calculation with different models for the tertiary stage

4.3.3.1 RUPTHER post-test-calculations

The considered RUPTHER-14 experiment was conducted by CEA in France [Mongabure and Desmet 1999]. Figure 4-5 shows the main geometrical data of the experiment, which can be regarded as axisymmetric.

The test pipe of 16MND5 was 270 mm long and 88.9 mm in diameter. The wall thickness was 2 mm. Due to the centred external heating coil the resulting vertical temperature profile had its maximum in the vertical centre, too. Therefore the maximum displacement and the failure can be expected at the vertical centre as shown in Figure 4-6.

Figure 4-7 shows the planned loading history and the central diameter increase of the RUPTHER-14 experiment. After increasing the pressure to 8 bar the temperature was increased to 1000 °C at the hot spot. This regime was kept until 18,000 s, when the pressure was slightly reduced to reach a level of 6 bar after 25,200 s. However, the tube failed earlier: at 22,180 s. Though different boundary conditions and slight temperature changes were applied, it was not possible to get numerical results for the time dependent diameter increase showing exactly the same behaviour as measured. The calculations rupt02 to 05 differ in the slightly changed temperature (+5 K, -5 K respectively) and the assumed rupture strain in rupt02 was reduced to 50 %, while it was normally 60 %. Especially the strong radius increase just after reaching the high temperature level at 1,800 s and the accelerated creep at the pressure reduction stage can not be represented by the code.

It is supposed that the reasons for this discrepancy could rather be some uncertainties in the measuring data of the experiment than the numerical approach. The temperatures might have been higher in the wall - especially at the beginning of the high temperature level - than the thermocouples show, because they are mounted on the wall (see also the discussion in section 6.1). Additionally a distance change between the tube and the induction coil can cause an interaction between pipe deformation and local heating power density. This could be considered for the last stage, when the pressure was dropping, but the creep process accelerated. Another reason can be the scale of the experiment. A wall thickness of 2 mm is relatively thin and small deviations from the design state – either geometrical or material – have a large influence. However, altogether the agreement of experiment and simulations is quite satisfying.
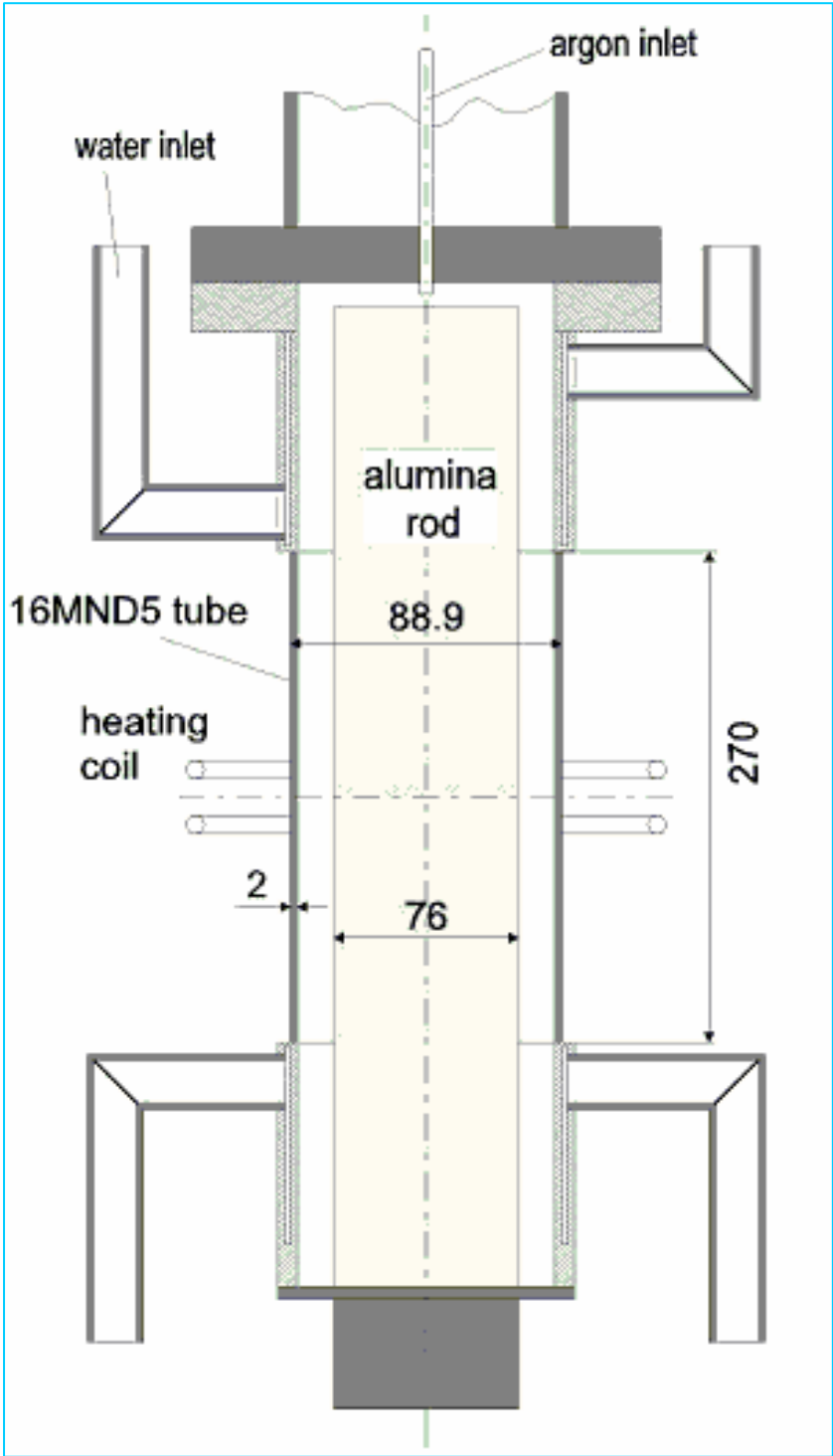
Figure 4-4: Scheme of the RUPTHER-14 experiment
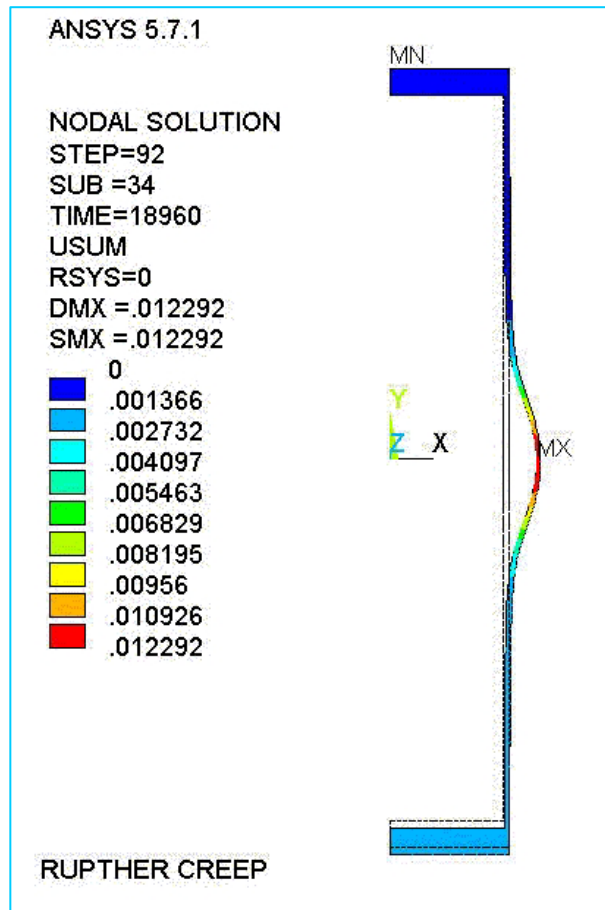
Figure 4-5: Displacement [m] of the pipe; ANSYS simulation of the RUPTHER-14 experiment
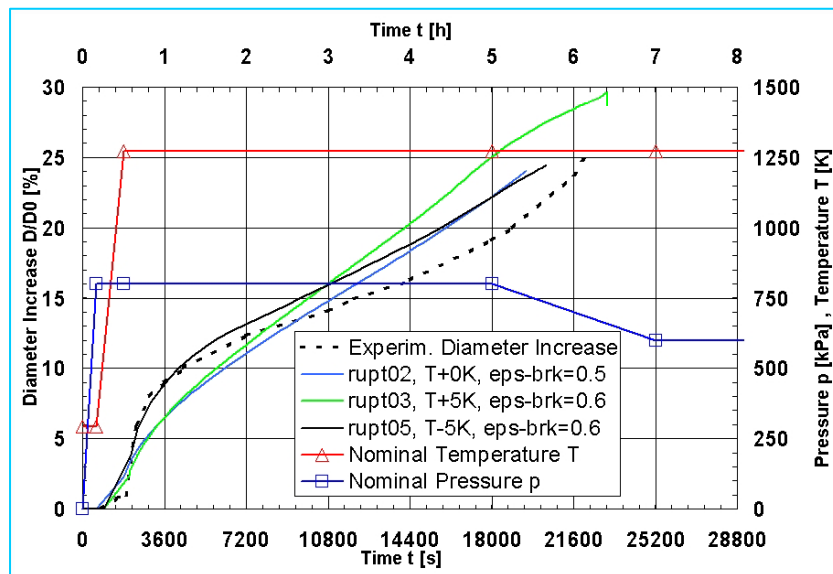
Figure 4-6: Measured diameter increase versus time and calculated diameter increase for different material parameters; right axis temperature and pressure vs. time

4.3.3.2 MPA-Meppen post-test-calculations

The considered MPA-Meppen test was performed at a test site of the German army in Meppen, Germany [Obst et al 1988]. Figure 4-8 shows the principal configuration of this tube failure experiment. In comparison to the RUPTHER test the MPA structure is a rather thick pipe with a wall thickness of 47 mm in the failure region. The vertically positioned test pipe was 2 700 mm long and had an internal diameter of 700 mm. Several external heating coils were placed vertically around the pipe and the resulting vertical temperature profile had its maximum in the vertical centre with a measured maximum at the end of the test of 735 °C. Instead of the French steel 16MND5 the German steel 20MnMoNi55 was used.
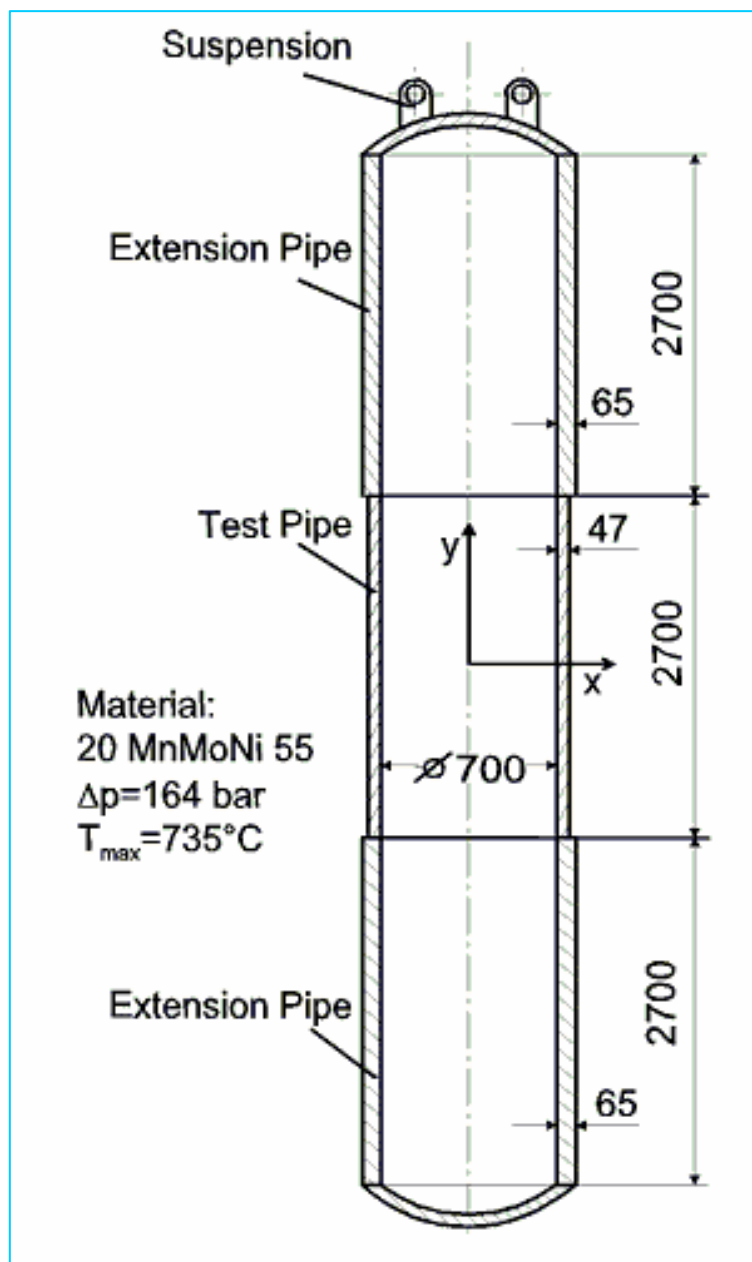
Figure 4-7: Geometry of the MPA-Meppen experiment

Therefore the maximum displacement and the failure site can be expected at the vertical centre. The loading history of the MPA-Meppen test is given in Figure 4-9. Starting with a pressure of 120 bar, the pressure was increased to 165 bar and the temperature was increased in three stages to 735 °C at the hot spot. This regime was kept until failure. Because temperatures around 700 °C were only achieved during the last 1,200 s significant deformation is also only recorded for this period. Figure 4-10 shows the comparison of the radius development between the test and different calculations for the last stage. The calculations UR1 to UR3 differ only in their temperature field, which has been shifted by ΔT=5 K up or down.
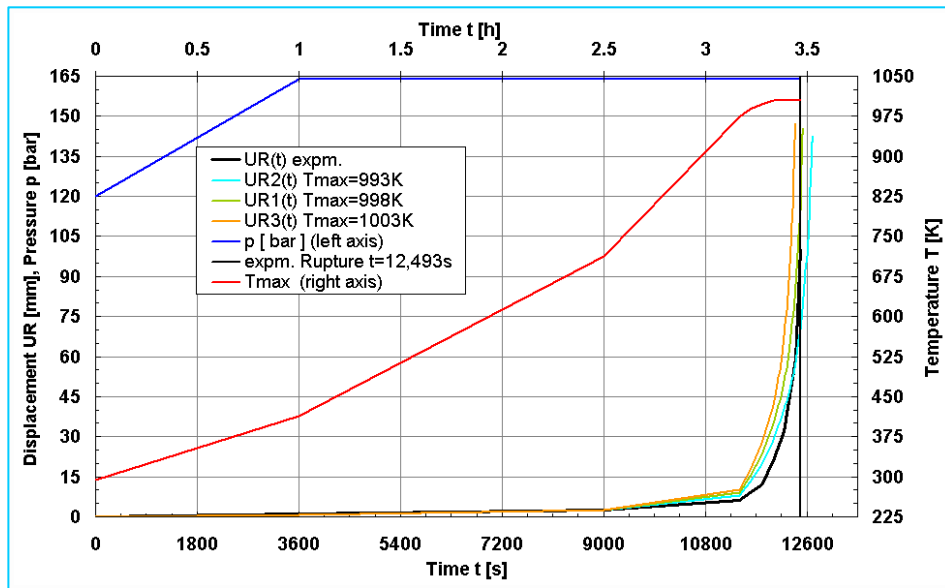
Figure 4-8: Loading history of MPA-Meppen test and comparison of the measured and calculated radius increase
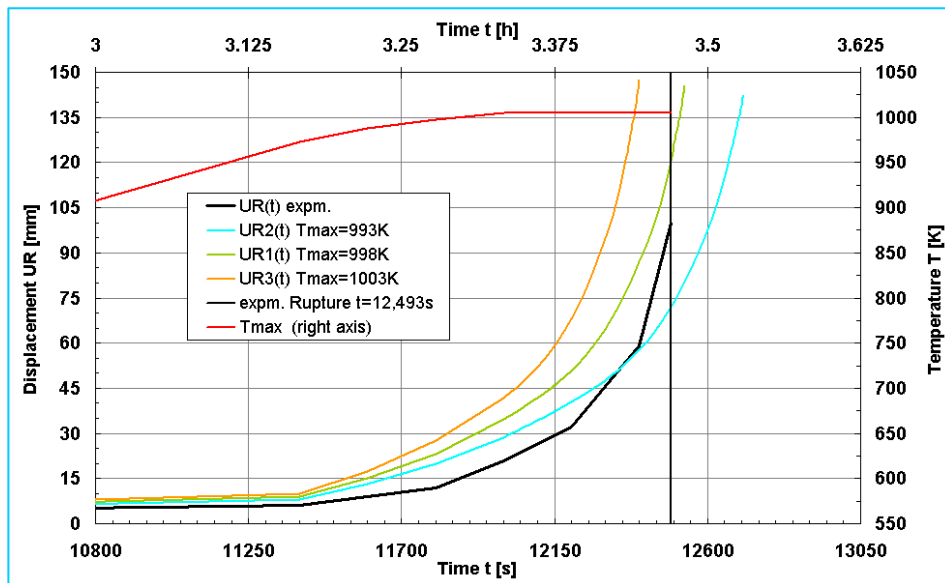
Figure 4-9: Comparison of the radius development during the last stage of the MPA-Meppen test

The results of the FE calculation are quite satisfying also in this case. The time dependency of the results implicates a slight uncertainty with respect of the temperature level.

4.4 Modelling of material damage

The material damage due to significant creep strains and plastic strains is modelled by a damage measure D, which is incrementally accumulated at the end of a load step or substep of the FE analysis. The damage increment is:

$$\Delta D = \left[\frac{\Delta\varepsilon_{eqv}^{cr}}{\varepsilon_{frac}^{cr}(\sigma, T)} + \frac{\Delta\varepsilon_{eqv}^{pl}}{\varepsilon_{frac}^{pl}(T)} \right] \cdot R_{v} \qquad \textbf{Eq 4-12}$$

with $\varepsilon_{frac}^{cr}(\sigma, T)$ being the creep fracture strain of the uniaxial creep test at constant stress and temperature and $\varepsilon_{frac}^{pl}(T)$ the plastic fracture strain (true strain) of the tensile test. R_{v} is a function, which considers the damage behaviour in dependence on the triaxiality of the stress tensor [Lemaitre 1996]:

$$R_{v} = \frac{2}{3} \cdot (1 + v) + 3 \cdot (1 - 2v) \cdot \left(\frac{\sigma_{h}}{\sigma_{eqv}} \right)^{2} \qquad \textbf{Eq 4-13}$$

where σ_{h} is the hydrostatic stress and σ_{eqv} is the von-Mises equivalent stress. The accumulated damage is:

$$D = \sum_{i=1}^{ldstep} \Delta D_{i} \qquad \textbf{Eq 4-14}$$

In the FE analysis a damage is calculated for each element. If the element damage reaches the value of D = 1, the element is deactivated by multiplying its stiffness matrix by a factor of 10^{-6}. The element's load vector is zeroed. The UPF UELMATX.F is used for this operation. FORTRAN routines are also developed for the initialisation of the damage calculation and for the post processing of the damage [Altstadt 2003].

5   Coupling of thermal und mechanical calculation

5.1   Problem

The description of the influence of the thermal dynamic and the mechanical processes on each other is a substantial goal of the modelling. The influence of the thermal conditions on the mechanical behaviour is obvious:

- The elastic and viscoplastic material properties are temperature dependent

- Temperature gradients lead to hindered thermal expansion and thereby to thermal stresses in the vessel wall

However, there is also a feedback from the mechanical behaviour to the thermal behaviour, which should be taken into account:

- Due to the viscoplastic vessel wall deformation the melt pool geometry is changed and the melt level is decreased.

- Due to the viscoplastic deformation there is a decrease of the wall thickness (and thereby of heat resistance).

- The vessel deformation leads to an increase of the surface of the vessel wall and thereby to the increase of the heat releasing surface. The total surface of the melt pool is also enlarged by the radial vessel expansion.

Therefore a full sequential and recursive coupling of the thermal and the mechanical model is necessary.

For the realisation of the coupling in the FE code ANSYS® the so called physical environments are used [Ansys 2003]. A physical environment denotes a complete submodel for solving a problem of a field of physics (e.g. mechanics, thermal hydraulics, electromagnetics).

The boundary conditions and loads within such a model (environment) consist of base loads and coupled loads. Loads which are not linked to another analysis are base loads. In our case the internal heat generation rate is a base load within the thermal model since it is not dependent on the mechanical solution. Analogously the pressure is a base load in the mechanical submodel.

Contrary to the base loads, the coupled loads result from a previous solution of a different model (environment). In our case the temperature load – obtained from the thermal solution – is a coupled load in the mechanical analysis.

As already discussed in chapter 3, the CFD simulation is too expensive for the thermal environment of the coupled model. Moreover, the available turbulence models are not suitable for the prototypic configuration. Therefore the ECCM is used within the thermal submodel.

5.2   Programming realisation

5.2.1   General model definition

The macro language APDL (ANSYS Parametric Design Language) is used for the programming of the simulation of the in vessel melt retention. During the development of the coupled model it has been experienced that – instead of principally two necessary submodels (thermal and mechanical) – three environments (submodels) are required to successfully simulate the IVR processes:

- thermal submodel for the calculation of the temperature field (SM1)

- mechanical submodel for the calculation of the viscoplastic vessel deformation (SM2)

- mechanical submodel for the calculation of the melt pool deformation (SM3)

Two mechanical submodels are necessary because within the mechanical solution very different material properties and material models have to be considered. With only one mechanical submodel the convergence of the solution could not be achieved. The liquid melt is mainly described by its compressibility, the resistance against shear is very low. Contrary to that, in the steel wall all stress components can arise, the resistance against compression and shear is high. The simultaneous consideration of melt and steel wall in one solution step thus would lead to a badly conditioned overall stiffness matrix. The mechanical solution is therefore realised in two steps (two submodels). This procedure has been proved to be numerically much more stable.

Before the definition of the submodels a general model has to be generated – the so called general physics environment (GPE). Within this GPE the geometry, the local coordinate systems, the mesh, the material attributes etc. are defined. The element types of the submodels have to compatible to each other concerning their shape and node number. The zones of the GPE (areas in case of the 2D model) are characterised by attributes, which contain information on materials, parameters constants and element types to be connected with the zone. Figure 5-1 shows an element plot for the simulation of a FOREVER experiment. The different material zones are shown in different colours: steel (blue), melt (dark green), insulation (orange) and the blurred zone (light green). The blurred zone contains several internals, the support for the heater, the insulation, the thermocouples and some loose glass wool. As mentioned the different materials correspond to the different zones, with the exception of the horizontal vessel flange (also steel like the vessel). It is connected with a separate zone since it is only active in the thermal submodel.

Because of the changing geometry it is necessary to define various node groups which can be accessed independently from their current position. This is especially true for the load application in the transient thermal model.

Within the single submodels the zones, which are active during the according analysis, are meshed with the appropriate elements while the inactive zones are filled with null elements. The definition of the null elements is done in the pre-processor. In the solution the null elements are not considered. Therefore they are not comparable with the deactivated elements, whose contributions to the matri-

Figure 5-1: Element plot of a FOREVER-Model with differently coloured material zones

ces are minimized, but which are always present (see section 4.4).

5.2.2 Thermal model (SM1)

For the calculation of the temperature field all zones of the model are meshed with thermal elements, i.e. there are no deactivated elements and no null elements. The adequate modelling of the thermal processes in the FOREVER vessel or within an LWR requires some features to be fulfilled by the elements. In the following the physical requirements, the solution strategies and the used element types are described:

Figure 5-2: Shape and position of the superelement

- The heat conduction in the vessel wall, in the insulation and in the blurred zone is calculated with 2D thermal elements (PLANE55). It is possible to omit the insulation and the blurred zone, which leads to a large empty space in the vessel. This option is foreseen for the prototypic scenario.

- The melt pool zone with inner heat generation is also meshed by 2D thermal elements (PLANE55). Additional routines control the anisotropic material properties (cf. Section 3.2).

- At the interface between melt and vessel wall a tangential relative motion must be possible. This is realised by contact and target elements (CONTA171 and TARGE169). These elements are used as well in the thermal submodel as in the submodel for melt pool deformation. For this purpose their DOFs, their parameters and their options are modified according to the corresponding submodel.

- Because of the changing geometry of the empty space (internal white zone in Figure 5-1), the view factors for the radiation model are changing between the corresponding elements. Therefore the superelement for heat radiation is newly created at the beginning of each thermal analysis. Figure 5-2 shows the shape and the position of the superelement at the beginning (dark) and at the end (light) of a calculation for the FOREVER scenario. The global coordinate system is shown on the lower left. The origin of this coordinate system corresponds to the lowermost internal position of the undeformed vessel. Figure 5-2 shows also the coordinate system no. 20, whose origin corresponds to the centre of the undeformed vessel sphere (cf. Figure 5-1). Its vertical position is at the connection of sphere and cylinder. If the insulation and the blurred zone are not modelled, the empty radiation space is formed by the vessel lid, the vessel wall and the melt pool surface.

- At the outer vessel surface, heat radiation and convection are considered. Since the thermal elements (PLANE55) allow only one boundary condition at their free surface, the nodes of the outer surface were additionally meshed with „surface effect elements" (SURF151). These elements consider the heat exchange with an environment of constant temperature. In case of a dry environment a convective boundary condition with a fixed HTC and constant ambient temperature is applied. In case of external flooding, a heat flux density depending on the over temperature is applied.
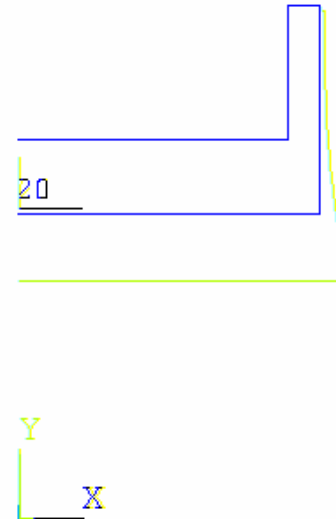
5.2.3 Mechanical model for the vessel deformation (SM2)

Within the viscoplastic analysis of the vessel wall only the spherical lower head and the cylindrical part of the vessel are meshed. The used 2D structural 4-node elements are suited for the implicit solution of creep and plasticity considering large strain and deflection. The elements in the remaining zones are null elements.

Figure 5-3 shows the nodes, the pressure load and the symmetry boundary conditions at the vessel axis and at the upper boundary. The colour gradient of the shown pressure load results from the consideration of the weight of the liquid melt. In addition to the mechanical base loads the current temperature from the latest thermal analysis is applied as coupled load. Further details can be found in chapter 4.
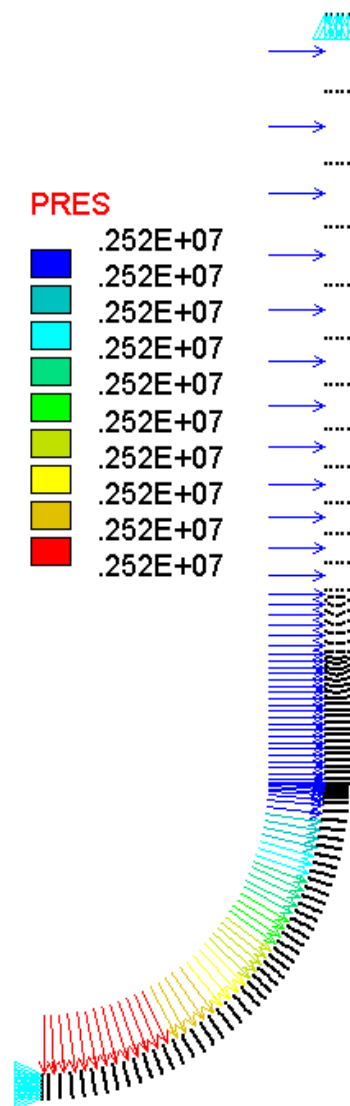
Figure 5-3: Node plot with pressure- and displacement boundary conditions

5.2.4 Mechanical Model for melt pool deformation (SM3)

A second mechanical submodel has been developed to simulate the melt level drop and the deformation of the melt pool as well as a possible gap formation between

melt crust and vessel wall. Based on the latest mechanical solution for the vessel wall, the contour of the inner vessel surface is modelled by target elements (TARGE169). In Figure 5-4 the elements, which are not wetted due to the decreased melt level, are represented in the upper right range as free grey line. The remaining target elements from the melt level downwards until the south pole are covered by the pink coloured hyper-elastic structural elements (HYPER56), which are representing the melt volume. The spherical surface of the melt elements is connected to contact elements (CONTA171), which are the counterparts to the target elements. The original geometry of the elements is represented by the wire mesh plot. All the other elements in the zone of the vessel wall and of the internals are declared as NULL elements.
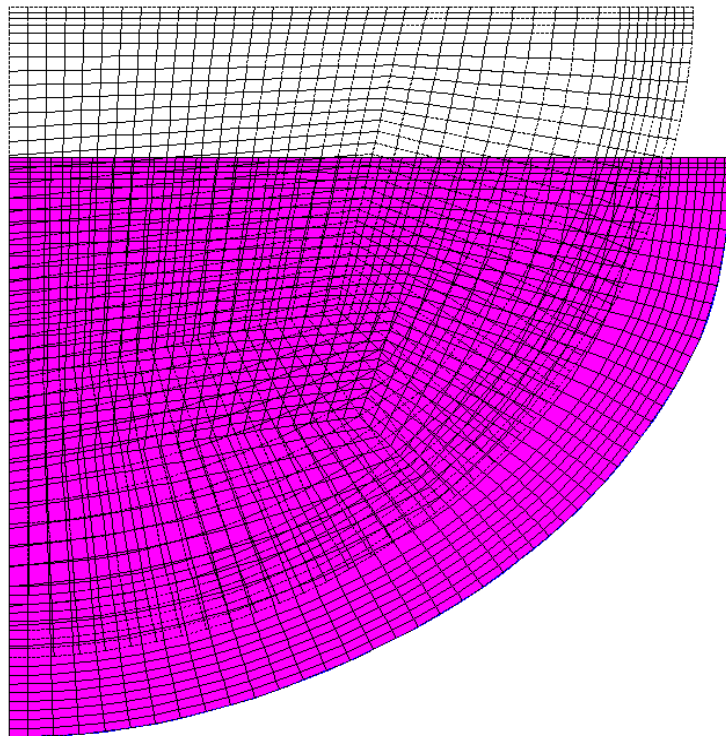
Figure 5-4: Element plot of the melt deformation submodel at the beginning (wire mesh) and at failure time (pink)

The mesh representing the deformed melt zone is adopted for the next thermal analysis. In this thermal analysis all the elements described in section 5.2.2 are activated again.

5.2.5 Summary of element types and models

In the Table 5-1 an overview is given for the element types used in the coupled model. At first the element types with temperature degree of freedom (DOF) are listed, then the types with displacement DOFs and finally the element types with DOFs depending on the particular submodel.

Table 5-1: Element types used in the coupled model

Element type	DOF	Node number
LINK32, 2D heat conduction bar	Temperature T	2
MATRIX50, heat radiation superelement	Temperature T	varying
PLANE55, 2-D thermal element	Temperature T	4
SURF151, 2-D surface effect element	Temperature T	2
HYPER56, 2-D hyper-elastic structural element	Displacement UX, UY	4
PLANE182, 2-D structural element	Displacement UX, UY	4
TARGE169, 2-D target element	Temperature T; Displacement UX, UY	2
CONTA171, 2-D surface to surface contact element	Temperature T; Displacement UX, UY	2

From Table 5-2 it can be seen which element types are active in a specified submodel and in a specified zone. The element type LINK32 (Table 5-1) is not directly used in a submodel, but comes indirectly into the thermal submodel via the heat radiation superelement (MATRIX50).

Table 5-2: Usage of the elements within the different submodels and zones

Model zone	Thermal submodel (SM1)	Mechanical submodel (SM2)	Melt pool deformation submodel (SM3)
Melt	PLANE55	NULL	HYPER56
Melt boundary to the vessel	CONTA171	NULL	CONTA171
Vessel boundary to the melt	TARGE169	NULL	TARGE169
Vessel wall (cylinder and sphere)	PLANE55	PLANE182	NULL
Vessel wall (flange / upper head)	PLANE55	NULL	NULL
Internals (FOREVER only)	PLANE55	NULL	NULL
Empty space in the vessel	MATRIX50	NULL	NULL
Outer surface of the vessel	SURF151	NULL	NULL

5.2.6 Course of a coupled analysis

Figure 5-5 shows the general structure of the coupled analysis. Based on the generation of the GPE the thermal, the mechanical and the melt deformation submodels are defined. Then a stationary temperature field is calculated for the undeformed vessel geometry. The calculated temperatures are separately stored for each node, since a reuse of the matrices is not possible after the mesh deformation in the mechanical submodels. After storing all the information of the thermal environment this submodel is left.

After switching to the mechanical submodel (SM2) a solution for the thermal expansion of the vessel is done considering also the deadweight of vessel and melt. The mesh of the vessel wall is shifted to the calculated node positions (UPCOORD command). Though the target elements defines as NULL elements in the mechanical submodel (SM2), their positions are also corrected since the corresponding nodes of the inner wall surface are shifted. After storing all the information of the mechanical environment this submodel (SM2) is left.

After switching to the submodel SM3, the melt pool deformation is calculated considering the new contour of the inner vessel wall, the weight of the melt and the internal pressure. The mesh of the melt is then shifted to the calculated node positions

(UPCOORD). After storing all the information of the mechanical environment for the melt deformation this submodel (SM3) is left.

Having a solution for each submodel corresponding to a real time of about 100 s, the algorithm enters a solution loop. Within this loop at first the transient temperature field is calculated (SM1), then the transient viscoplastic solution (SM2) and finally the melt deformation (SM3). Within the thermal solution two load steps are necessary. In the first one the externally stored temperature field of the last solution is transferred to the new geometry, while the second one comprises the actual transient solution of the current time step. Before the solution within the mechanical submodel (SM2) the shift of the mesh is cancelled, since the real deformation history is related to the initial node positions of the mechanical submodel SM2. Within the melt deformation submodel (SM3) a static solution is always performed.

The maximum damage of the vessel wall elements is used as an exit criterion from the solution loop. If the maximum damage exceeds the value of 1 the transient solution is stopped. In case of the FOREVER calculation a final solution step is done at T = 300 K, which provides the cancellation of the thermal strain. This makes possible the comparison of the wall thickness reduction with measurements at cut vessel segments after the test.
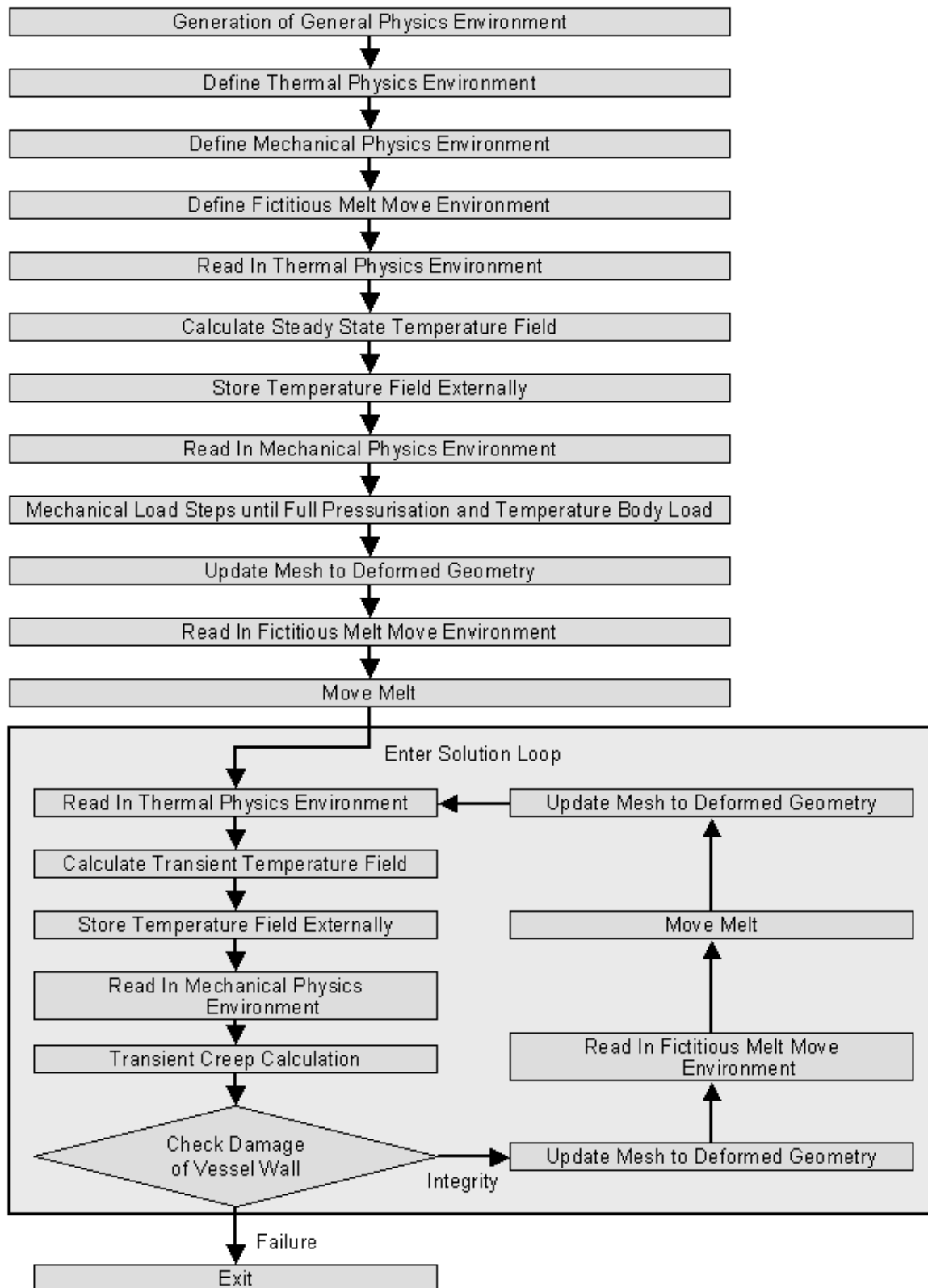
Figure 5-5: Scheme of the recursive coupling

5.3 Influence of coupling to vessel failure

To illustrate the influence of the recursive sequential coupling to the simulation, the failure times of a reference scenario (cf. section 7.1.1) with and without coupling are compared. The reference scenario is based on the FOREVER geometry (chapter 2) with the planned value for internal pressure (25 bars), heating power (38 kW) and melt volume (14 l). In Table 5-3 the input parameters of the reference calculation are summarized. These values correspond to those in the scaling discussion (chapter 2).

Table 5-3: Input parameters for the reference calculation

Parameter	Symbol / Unit	Value
Heating power	Q [kW]	38
Outer radius of the heat releasing zone	r_{WFZ} [m]	0.135
Internal vessel overpressure	p_i [bar]	25
Melt volume	V [m3]	0.014
Internal and external emissivity coefficient	ε [-]	0.75
Initial global time step width	Δt_g [s]	300

At the beginning of the calculation with recursive coupling the highest temperature in the vessel wall is 1357 K without consideration of thermal expansion. After the first feedback a stationary temperature field is obtained with 1320 K being the maximum wall temperature. This means that there is a drop of the maximum wall temperature of 37 K due to the change of the geometry, which is mainly characterised by the increase of melt pool surface, the increase of outer vessel surface and the increase of the inner empty space for heat radiation.

Subsequently the maximum wall temperature further drops until it reaches 1289 K at the failure time of 21 150 s. This temperature drop is caused by the effects already mentioned above, which are further increasing, and additionally by the wall thickness reduction leading to a lower thermal resistance of the wall.

In the calculation with the simple coupling the effect of temperature decrease is not considered since the initially calculated temperature field is maintained until failure time. The maximum wall temperature is therefore always 1357 K. The resulting failure time is 8550 s, which is less than half the failure time of the recursively coupled reference calculation.

In addition to the pure temperature effect this acceleration is also caused by the position of the hot focus. In the recursively coupled calculation the hot focus sinks to lower polar positions what leads to a less harmful stress state since the distance to the cylinder-sphere transition gets larger. The comparison shows that the simple (one way) coupling provides very conservative failure times.

5.4 Gap formation

In the fully coupled model there are contact elements between melt and vessel wall. These contact element not only allow for tangential relative displacements between melt and vessel but also the development of a gap (different normal displacements).

Such a gap can theoretically develop if the solidified melt (crust) cannot follow with the radial widening of the vessel. It depends crucially from the viscoplastic properties of the melt crust whether a gap is actually generated or not. If a new gap is to develop, the crust should have to exhibit a higher strength than the vessel steel. This is

rather improbable at least for the FOREVER configuration, where the temperature level is not in a range in which vessel wall ablation could occur.

In the FOREVER tests EC5 and EC6 (Table 2-3) it was intended to provoke a gap formation by flooding of the melt surface. But a gap formation could not be achieved in any of the tests. Because of these experimental findings the FE modelling of the gap formation has not been further followed up.

6   Model validation based on the FOREVER-Experiments

6.1   Validation of thermal calculations

As an example, Figure 6-1 shows the temperature distribution at the vessel outside in the experiments FOREVER-EC2, EC3b and EC4 at those times when a relatively high and constant temperature level has been recorded. For comparison the temperatures of the FLOTRAN-CFD calculation and of a coupled calculation (cf. chapter 5) with the ECCM-approach are represented, too. In both calculations it was assumed that the melt level is 10 mm below the welding line. The ECCM results differ slightly from the CFD results and it can be stated, that the ECC-model represents the temperatures in the vessel wall in a more adequate manner.

Qualitatively the measured and calculated curves agree. Especially the position of the hot focus is represented correctly by the code. The quantitative comparison between the curves does not seem to be satisfactory at the first view. However, the reason for the deviation does not lie in an incorrect calculation, but in the position where the thermocouples measure the temperature.

Since the thermocouples are fixed on the outer surface of the vessel with clamps, they can not measure exactly the vessel surface temperature. Due to the direction of the heat flux the measured temperature is lower than the temperature at the surface. Even due to their own thickness the thermocouple readings must show lower temperatures than the vessel surface temperatures. On the vessel inside the situation is vice versa: the thermocouples (protected by surrounding pipes within the melt pool) must show higher temperatures than the temperatures at the vessel inner surface. This systematical measurement error becomes obvious especially at high heat fluxes, i.e. it is rather significant for the hot focus region in the FOREVER-experiments.
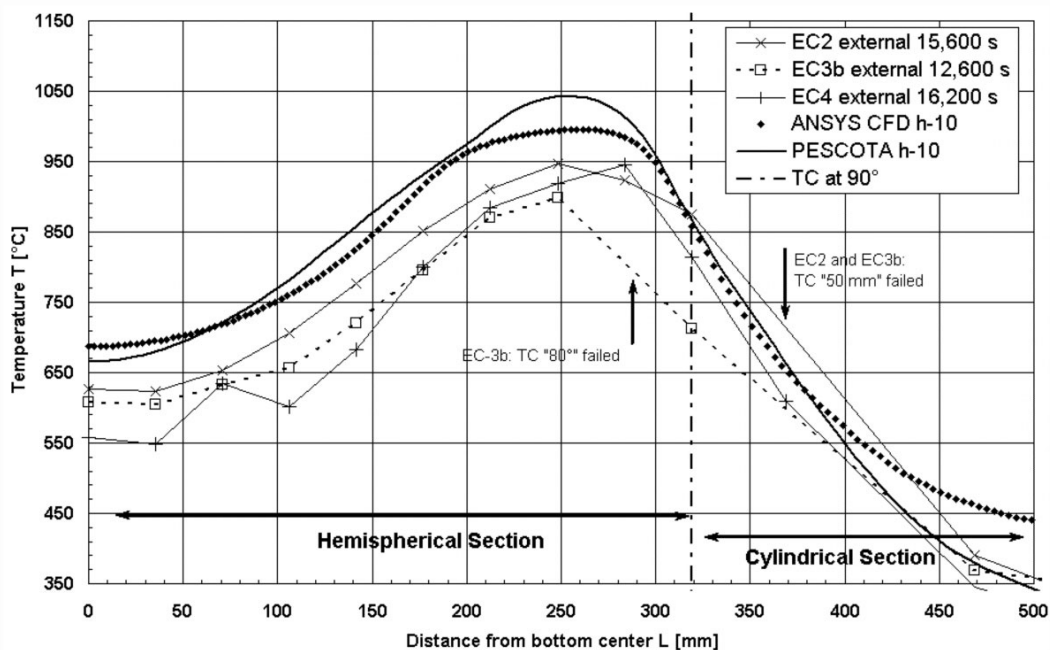
Figure 6-1: Course of temperature at the outer vessel wall: measured temperatures of the experiment FOREVER-EC2, EC3b and EC4, and calculated temperatures from the FLOTRAN-CFD-calculation and from the PESCOTA-ECCM calculation

For the internal temperature measurement within the protection tubes, which lost their wall contact at some positions, the data have to be checked even more careful, because the temperature boundary layer of the melt has a high gradient. The temperature changes are in the range of 200 K within some 2 mm distance to the wall in the hot focus region. This corresponds to the difference between the measurement and the calculation (cf. Figure 3-2 and 6-1).

To asses this systematic temperature difference, a FE-model in the dimension of the FOREVER-vessel has been developed. Figure 6-2 shows the stationary temperature field of the model, if a heat flux of 140 kW/m² is imposed on the internal vessel wall. The model uses rotational and vertical symmetry. The whole extension of the thermocouple and its fixation is modelled with 3 mm, where an ideal heat transfer is assumed within the whole structure of wall, clamp and thermocouple. No contact resistance is modelled between the components. All material properties are based on the steel 16MND5. The resulting temperature difference between the centre of the thermocouple (point A in Figure 6-2) and the vessel surface in a sufficient distance (point B), where no disturbance due to the thermocouple is assumed, is more than 20 K. The real temperature difference in the experiments should be even larger, because the contact resistance between the components is not considered in the model.
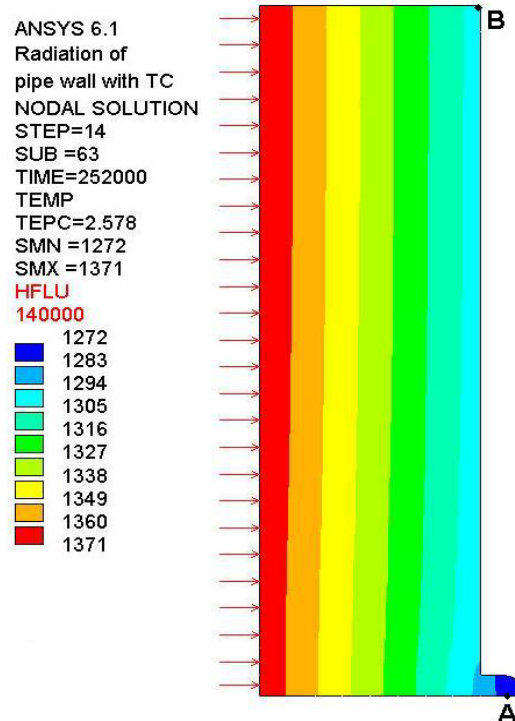
Figure 6-2: FE-model for the assessment of the systematic measurement error in the experiments with thermocouples fixed on clamps at the external surface. Temperatures in K, heat flux in W

6.2 Validation of the mechanical calculations

The pre- and post-test calculations for the different FOREVER-test have been compared with the experimental data. Metallographic observations on specimen of the vessels of FOREVER-C2 and EC2 were compared with the calculated damage of the FE-model. There are results available for the time dependent vessel displacements, creep strains and material damage for the tests FOREVER-C2, EC-1, EC-2, EC-3b, EC-4, EC-5 und EC-6 (cf. chapter 2). In the following the results for FOREVER-EC-2, EC3b and EC4 are discussed.

Figure 6-3 shows the calculated and the measured vertical displacement of the vessel south pole over time for the test EC2. Additionally the time dependency of the applied heating power and the internal vessel pressure are represented (right axis). The time t = 0 s corresponds to the start of the vessel pressurization in the experiment. The curves of pressure and power show, that the experiment was not running as scheduled at the beginning. At first there was only the half electrical power available (approx. 18 kW), because of a misfit of the generator. But to initiate vessel creep

anyway, the pressure was increased from 25 bar to some 40 bar. Parallel different actions were undertaken to eliminate the short current at higher power between the heater and the vessel. The shut down times were not too long to cause a freezing of the whole melt. After the time t = 12 900 s the experiment was running with the scheduled values for power and pressure. This is the time point, which correlates with the beginning of the calculations.
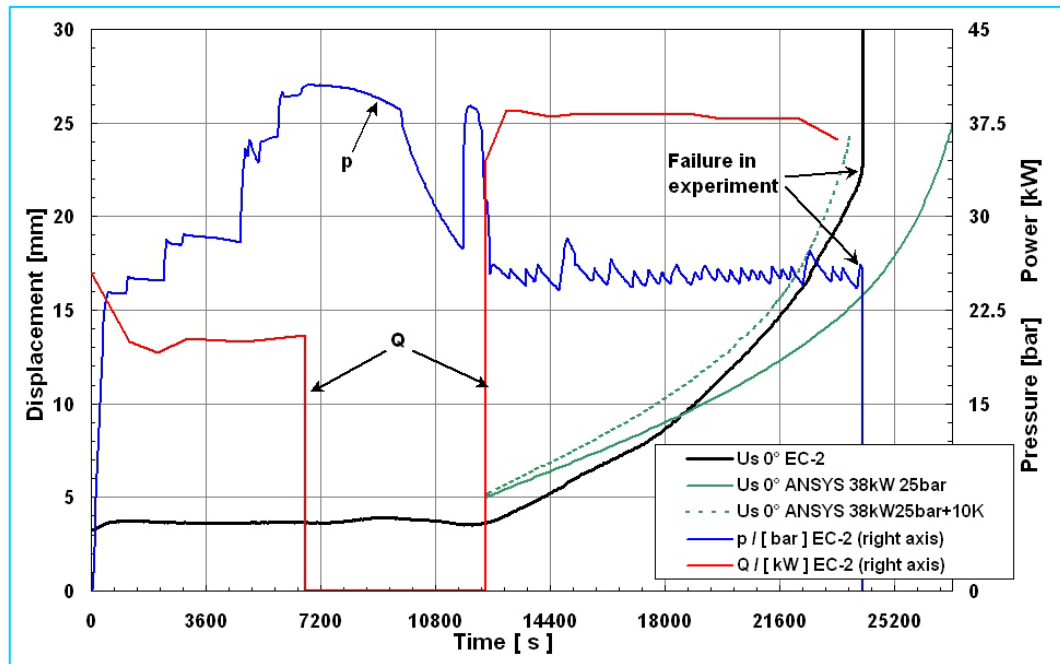
Figure 6-3: Heat generation, pressure and measured and calculated displacement of the vessel south pole in the experiment FOREVER-EC-2

Comparing the failure times a good prediction capability of the code can be stated (pre-test run: failure after 14 600 s after start of creep, experiment: failure 11 800 s after start of creep, cf. Figure 6-3). The non-conservativity of the pre-test run can be explained by the transients in power and pressure, which were not modelled. For the simple post-test calculation the overall temperature level was increased by 10 K, and this leads to a rather good agreement between experiment and calculation. This makes also obvious that a small temperature change of 10 K in the hot focus, where the temperature level is clearly above 1000 K, has a strong influence to the failure time. This is a consequence of the high temperature sensitivity of the creep strain rate.

A very good agreement between prediction and experiment was achieved for the failure position. The calculation showed the failure site some 50 mm below the welding line between cylinder and hemisphere. In the experiment the crack occurred some 60 mm below the welding. The horizontal size of the crack was approximately one third of the vessel perimeter.

Figure 6-4 shows the distribution of the creep strain (left) and of the material damage (right) at the calculated failure time. The maximum strain is to be found at the vessel inside in the area of the hot focus, while the maximum damage occurs at the vessel wall outside. This results from the high triaxiality of the stress state in this region (cf. Eq. 4-12 and Eq. 4-13).

Metallographic post test investigations with specimens from the failed vessel (performed at the Institute of Safety Research of the FZR) have shown, that the spatial distribution of the damage (visible in the shape of creep pores) agrees qualitatively well with the damage prediction of the applied damage evolution model (cf. Figure 6-5 and Figure 6-6). The applied model predicts a failure starting from the vessel outside as it has been proved by the experiment.
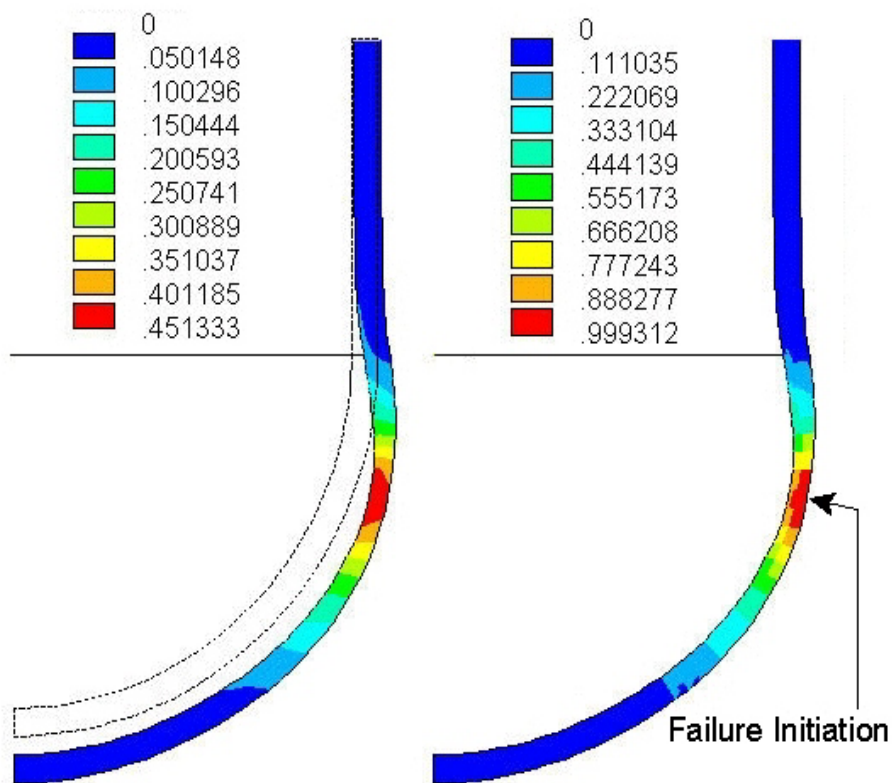
Figure 6-4: Distribution of the equivalent creep strain (left, max. 0.45) and the damage (right, max. 0.9993) at calculated failure time of t = 4:05h (38 kW, 25 bar, Experiment EC2)
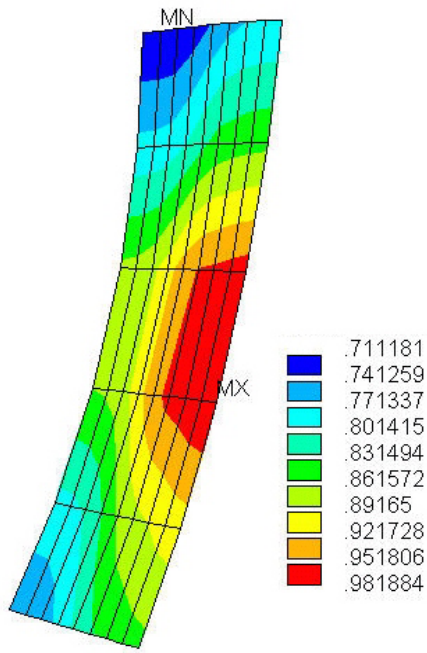
Figure 6-5: Calculated damage distribution
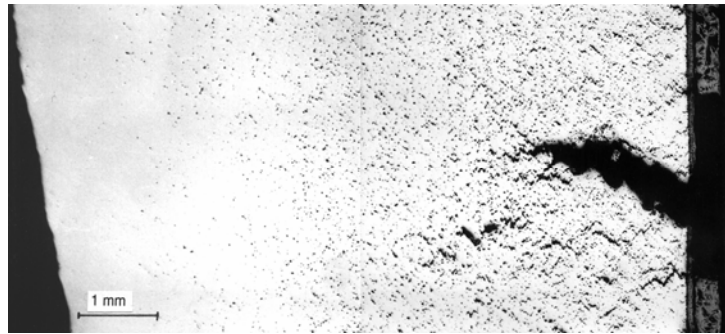
Figure 6-6: Metallographic photography of the FOREVER-EC2 vessel steel in the area of the failure position: left inside, right outside
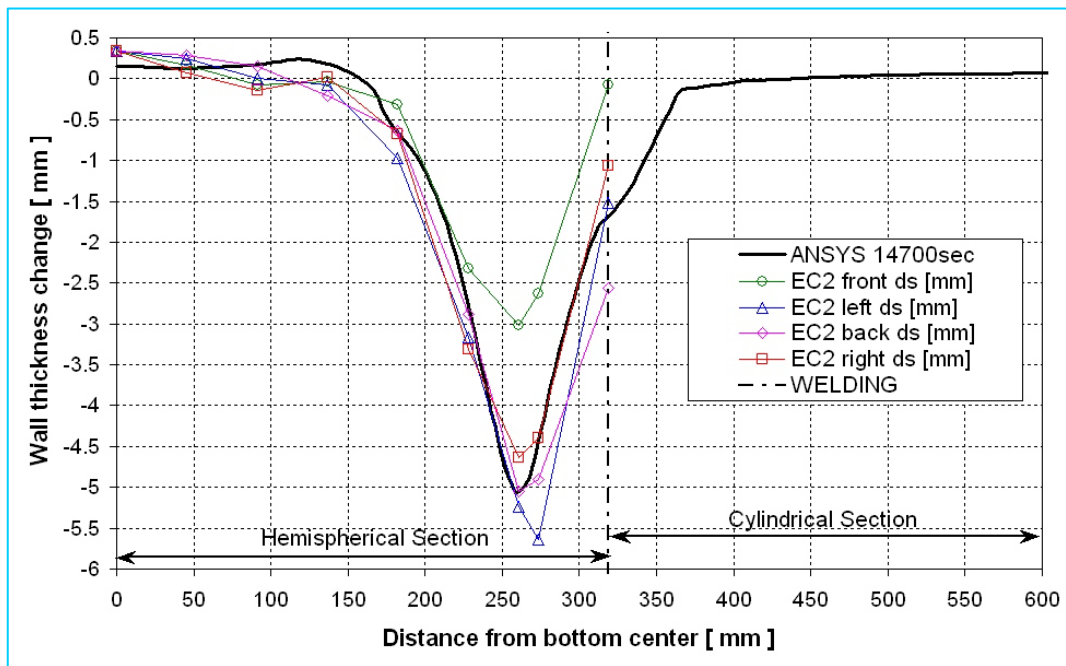
Figure 6-7: Wall thickness change at failure time of the experiment EC2 along the meridian line of the vessel

The wall thickness reduction during the test is another criterion for the comparison between experiment and calculation. Figure 6-7 shows as well the wall thickness change recorded for four different azimuthal positions along the meridian (each with a offset of 90°) as the wall thickness change obtained from the simulation. Also for this comparison a rather good agreement is found between the calculation and three of the four given experimental curves. The experimental curve "EC2-front" shows a smaller wall reduction. This can be correlated to the manufacturing tolerances of the vessel lower head, which was deep drawn (forged). At this position a slightly thicker wall caused a higher strength and therefore a smaller creep strain rate is implied.

In the lower part of the hemisphere a slight wall thickness increase is observed. This comes from the oxidization of the vessel surface which goes along with the decarburisation inside the surface. The developed oxide layer must be subtracted from the residual wall, since it does not contribute to the strength of the vessel. In the ANSYS calculation the reason for the thicker wall comes from the thermal expansion, since the wall thickness has been evaluated from the "hot failure state".

The results given in the Figures 6-3 to 6-7 come from the FE-model without full recursive coupling between thermal and mechanical model. The sinking of the melt pool has been set "by hand" prior to the transient calculation according to the general experience.

After the completion of the fully coupled model (cf. chapter 5), further post test calculations have been performed for the test EC2. In these calculations the original melt level at the beginning of the experiment has been applied, and the melt drop is calculated by the program itself. In the fully coupled model, much more parameters can be chosen by the user. In numerous variation calculations it has been observed, that the assumed values for the emissivity for the internal enclosure and for the external surface have a rather large influence to the temperature field and therefore to the failure time.

Figure 6-8 shows the displacement of the vessel south pole for two different calculations and of the measurement of the experiment EC2 over time. The two calculations only differ by their emissivity for the external vessel wall. One calculation assumes 0.7, the other 0.75. The lower value leads to higher temperatures and therefore to an earlier failure. The difference of the emissivity coefficients leads to a failure time difference of nearly one hour for the two calculations. One calculation can be regarded as conservative, while the other is non-conservative in comparison with the experimental failure time.
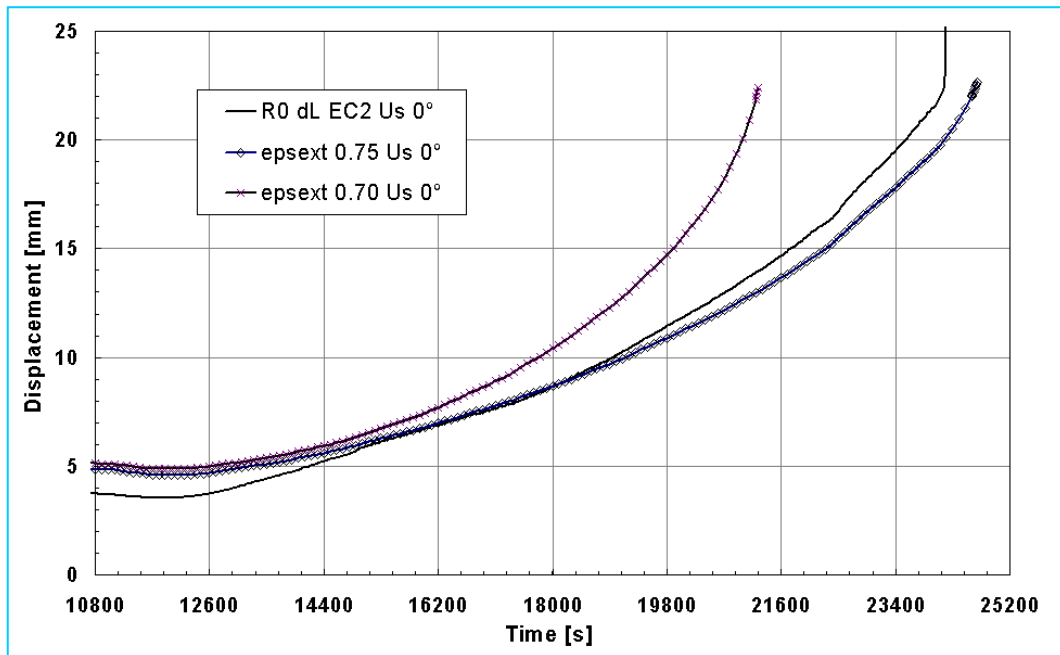
Figure 6-8: Measured and calculated displacement of the vessel south pole in the experiment FOREVER-EC-2. Calculation with the fully coupled model and different emissivity coefficients
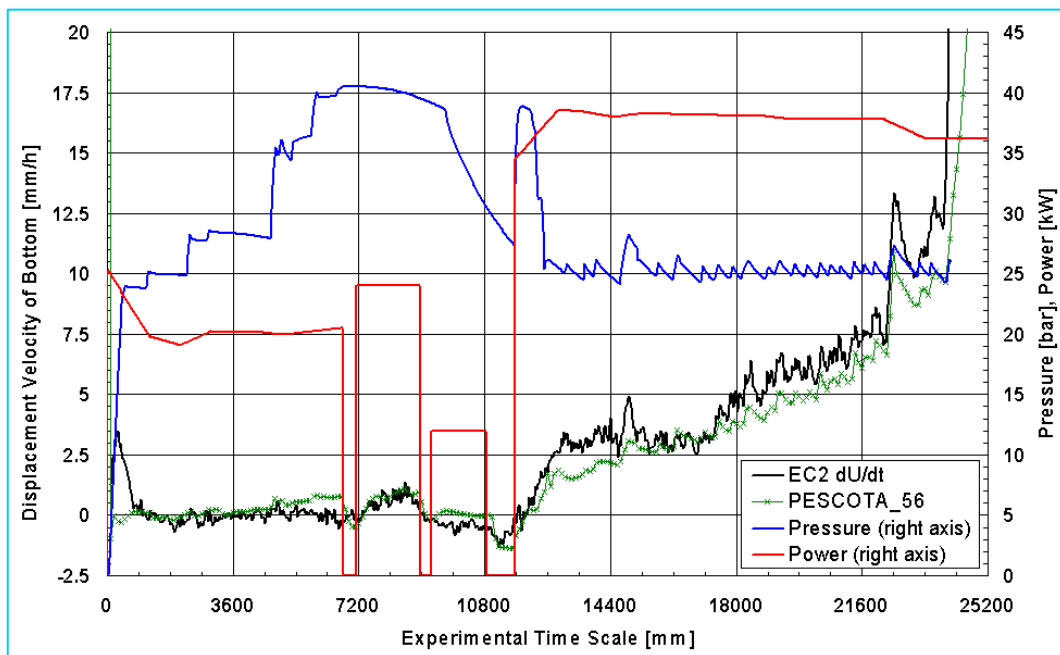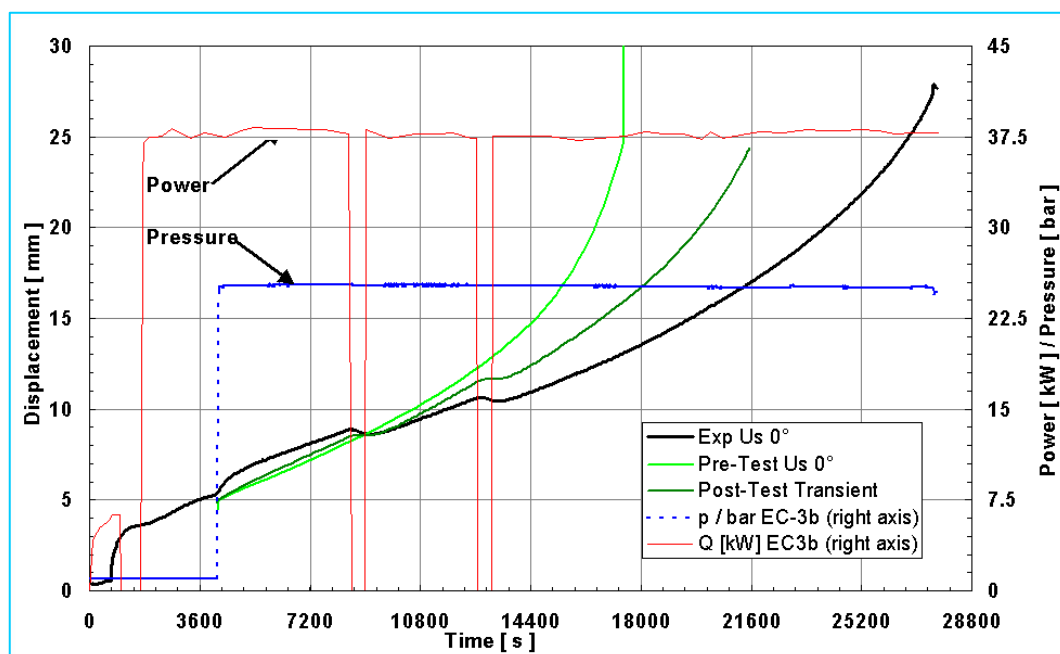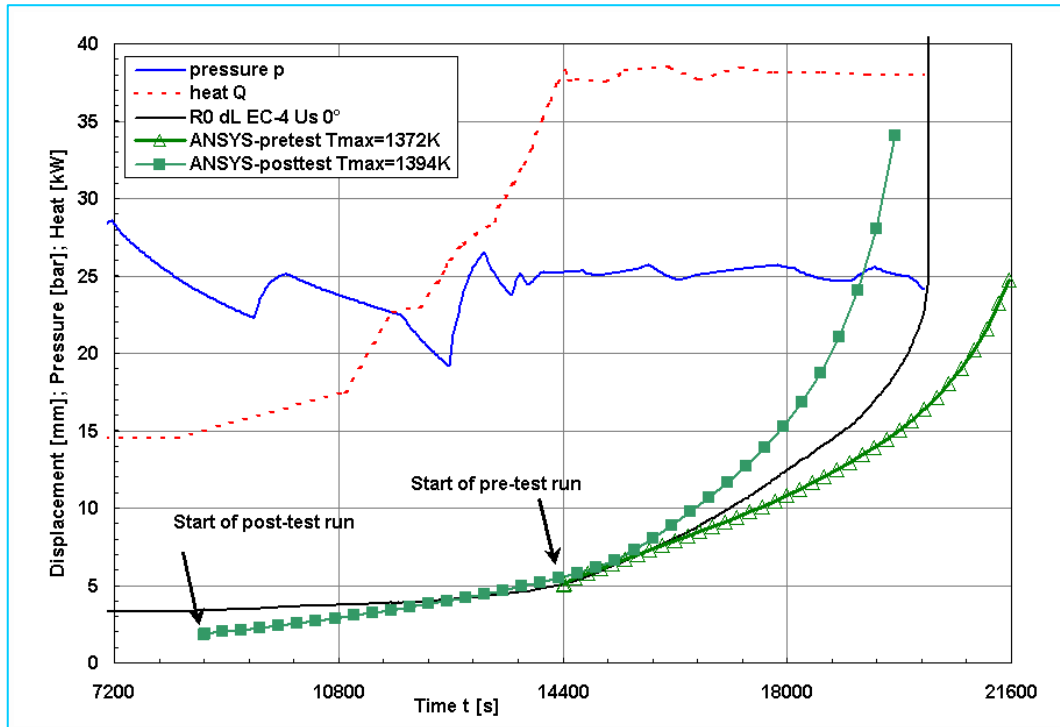

**Figure 6-9**: Heating power, pressure and measured or calculated displacement velocity of the vessel south pole in the experiment FOREVER-EC-2. Calculation with the fully coupled model

In these calculations the real pressure and heating power behaviour which occurred during the test have been applied. This can be seen very clearly in Figure 6-9, where the displacement velocity of the vessel south pole is represented over time. The velocity curves show a high sensitivity even to small pressure changes. It can be stated, that in principle the fully coupled model is able to describe or predict the vessel deformation exactly. Uncertainties concerning the failure time result mainly from not exactly known material parameters.

In the following the results for the FOREVER-experiments CE3b and EC4 are compared and discussed (cf. Table 2-3). In the Figures 6-10 to 6-11 are the measured and the calculated displacements of the vessel south pole for these experiments together with the heating power and the internal pressure given over time.

Figure 6-10: Heating power, pressure and measured and calculated displacement of the vessel south pole in the experiment FOREVER-EC3b

Figure 6-11: Heating power, pressure and measured and calculated displacement of the vessel south pole in the experiment FOREVER-EC4
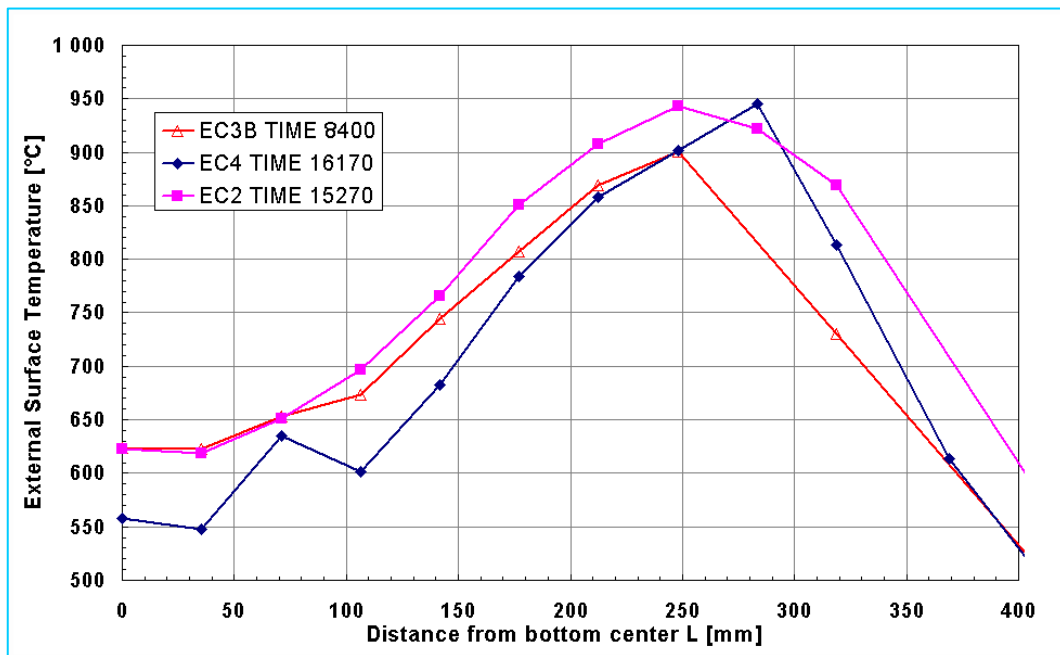
Figure 6-12: Comparison of the external wall temperatures in the experiments EC2, EC3b and EC4

For the experiment EC3b both the pre-test calculation and the post-test calculation result in an earlier failure than the experiment has shown. In the post-test calculation the real time dependence of the heating power and the pressure have been applied, while the pre-test calculation assumed the planned constant pressure and heating power. The fact that both calculations are too conservative, leads to the possible conclusion that either the creep resistance of the vessel steel (16MND5, cf. Table 4-1) was significantly higher than modelled by the creep data base or that the thermal calculation gave a temperature field with slightly over predicted temperatures. The latter reason could come from a damaged insulation above the melt pool (cf. Figure 2-1). That would result in a higher heat flux from the melt surface and an overall temperature drop. For this hypothesis hints can be found within the temperature measurements. Figure 6-12 shows the external wall temperatures of the vessel along a meridian line for the tests EC2, EC3b und EC4 at those times, where in each experiment the highest temperatures were observed. The experiment EC3b shows the lowest temperatures for the hot focus region, despite of the fact that the nominal heat generation was nearly the same for all experiments.

For the experiment EC4 (material SA 533 B, cf. Table 4-1) the pre-test calculation was slightly non-conservative, i.e. the predicted failure time is a little bit too late compared with the experiment. With a slight increase of the average temperature level by some 20 K a conservative behaviour of the calculation was achieved. It has to be remembered here, that the creep data base has been developed from creep tests for the French steel 16MND5 (cf. chapter 4.3.1).

The calculations for EC3b and EC4 have been performed with the model without recursive coupling between vessel deformation and temperature field. The coupled model was not yet available when the calculations were done. In this frame the discussion of experiment EC2 above in this chapter has to be considered.

It is very interesting to investigate and to compare the creep failure behaviour of the vessels in the tests EC3b and EC4. Already at the test site at the KTH in Stockholm it was found that the shape of the opening of the EC4-test at the failure site was remarkably different from the other FOREVER tests. In EC3b a rough crack surface was found at the failure site while in EC4 a rather ductile behaviour was observed resulting in nearly blade-like edges on both sides of the vessel opening. Figure 6-13 and 6-14 from the metallographic investigation show this different shape as a crack cross section side view (notice the different magnification). For these photographs the original sections from the vessel were cut to small cubes and the appropriate side was polished and etched. While in EC3b the failure shape shows a relatively slight wall thickness reduction with a strong development of pores (Fig. 6-13), the photography of the EC4 specimen shows opening sides with a very thin residual wall thickness (blade like, extreme reduction) and there are no pores visible (Figure 6-14). Thus the steel of experiment EC4 has a much higher ductility. The crack was observed in the hemispherical part approximately 7 cm below the weld. At the crack position the wall thickness decreases from 15 mm pre-test thickness to approximately 0.2 mm and the crack surface is smooth. Near the crack there are only a few pores. The failure occurred in the region of high temperatures and high deformation. In both tests and for both steels a fine bainitic structure was prevailing prior to the experiment. Due to the temperature history during the experiment the microstructure changed mostly into coarse bainite and, depending on the temperature distribution in the vessel wall, different parts are of coarse polygonal or banded ferrite.
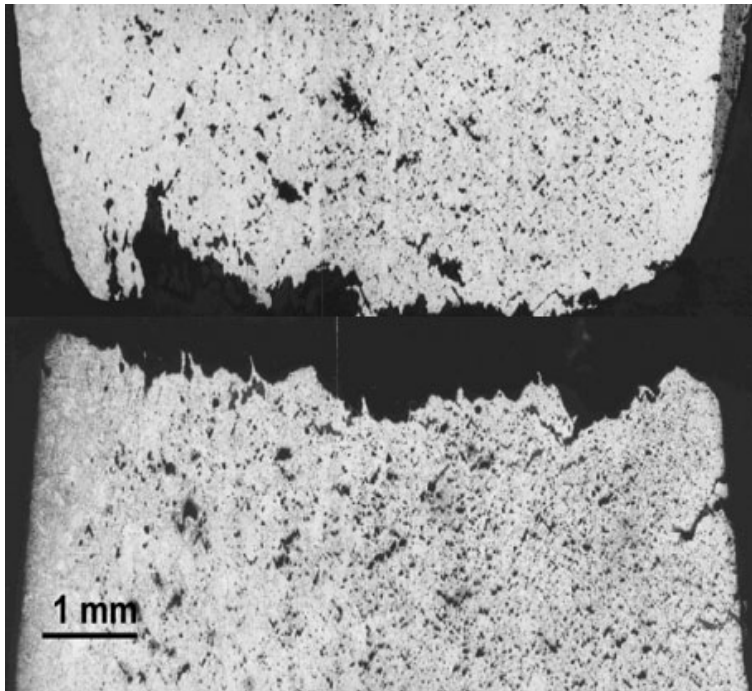
Figure 6-13: Photography of the microstructure of EC-3B at crack, etched samples. Full residual wall thickness is shown: left – inside, right outside
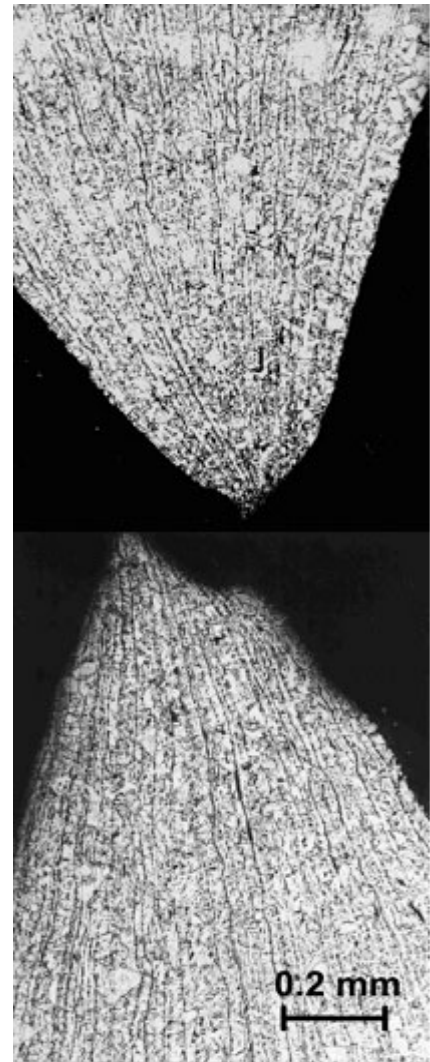

Figure 6-14: Microstructure of EC-4 at crack, etched samples. Left – inside, right - outside
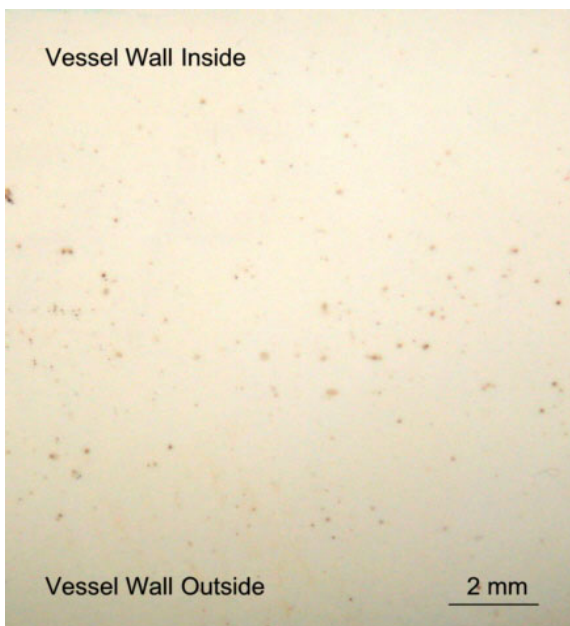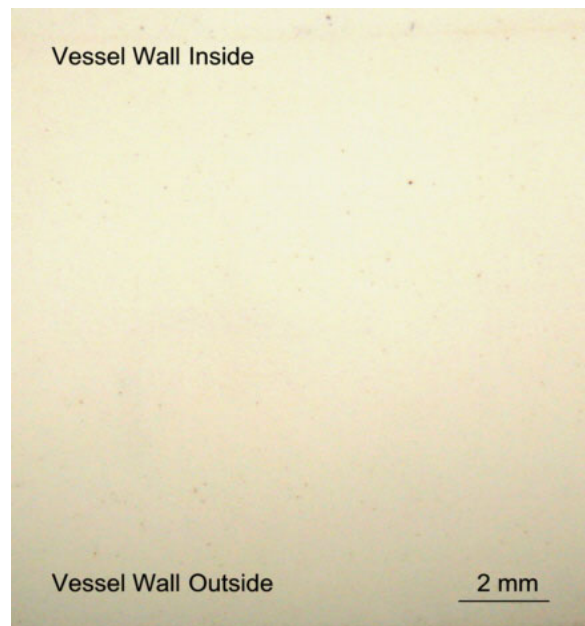

Figure 6-15: Baumann-replica EC3b

Figure 6-16: Baumann-replica EC4

The reason for the different ductility is not understood. But there is a hypothesis, that the sulphur content plays a major role [Mongabure 2000]. The comparison of the sulphur content of the two steels (cf. Table 4-1) shows, that in EC3b a higher sulphur content was present. The Figures 6-15 and 6-16 show Baumann-replica of wall section specimen of the two tests EC3b and EC4. The Baumann-replica reveals the distribution of sulphur segregations within the considered steel specimen. The Baumann-replica is made as follows: photo paper (bromine silver pa-per) is imbued with 5%-sulphuric acid, then the steel surface is imprinted for some minutes onto the paper and finally the paper is normally fixed and soaked. After this procedure the sulphur segregations appear brown. The comparison of both replica shows, that the lower head steel of EC3b, made of the French 16MND5 RPV-steel, contains some sulphur segregations. In the lower head of EC4, made from the American A533B RPV-steel, sulphur segregations are hardly to be found. This is in accordance with the chemical composition given in Table 4-1.

For comparison the results of creep tests of specimen from the LHF/OLHF-experiments are shown. The investigations were made by CEA [Mongabure 2000] and they lead also to the conclusion that a higher sulphur content goes along with a lower ductility. The Figures 6-17 and 6-18 show specimens of creep tests with temperatures between 700 °C and 900 °C and different nominal stresses. Considering the LHF-material (sulphur content 0.01 wt.-%, Figure 6-17) a lower ductility can be recognised than for the OLHF-material (sulphur content 0.001 wt.-%, Figure 6-18). This effect becomes more pronounced at higher temperatures (above the austenitisation point). Figure 6-19 shows the creep tests for the both steels at temperatures of 993 °C and 990 °C and nominal stresses of 18.8 MPa and 18.4 MPa. The figure shows the nominal and the true strains over time. It can be observed, that the OLHF-steel with the lower sulphur content is not only more ductile but has also a higher creep resistance. The failure time of the OLHF-specimen is more than twice (8:13 h) as long as the failure time of the LHF-material.

Even if these examples (EC3b and EC4) are extremes, this discussion shows, that the scatter of the material behaviour is an unavoidable uncertainty, which has to be taken into account for the model based prediction of the failure times for vessels under creep and plasticity conditions.
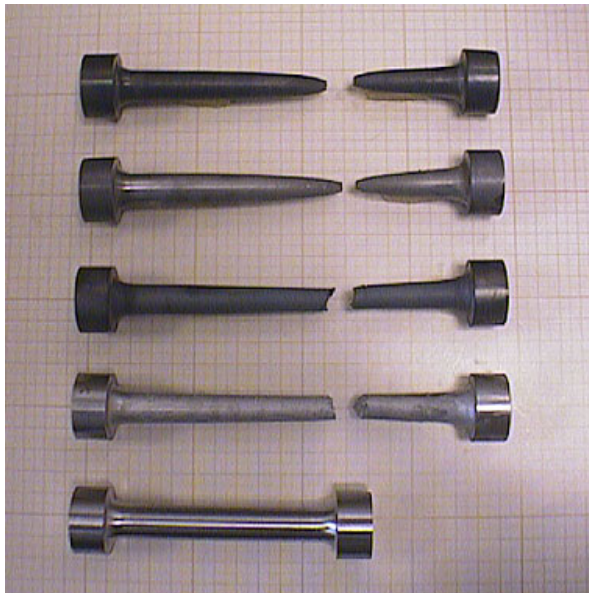
Figure 6-17: Specimens of LHF-material from creep tests at different nominal stresses at 720 °C (No. 1 and 2 from above) and 990 °C (No. 3 and 4 from above); [Mongabure 2000]
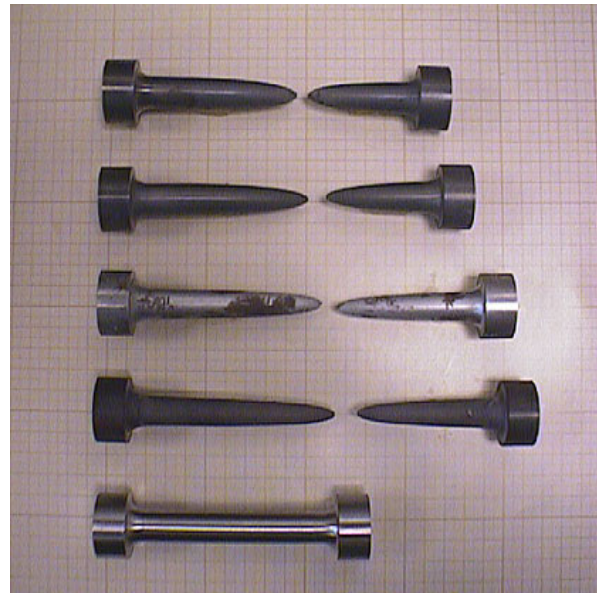
Figure 6-18: Specimen of OLHF-material from creep tests at different nominal stresses at 700 °C (No. 1 and 2 from above) and 990 °C (No. 3 and 4 from above); [Mongabure 2000]
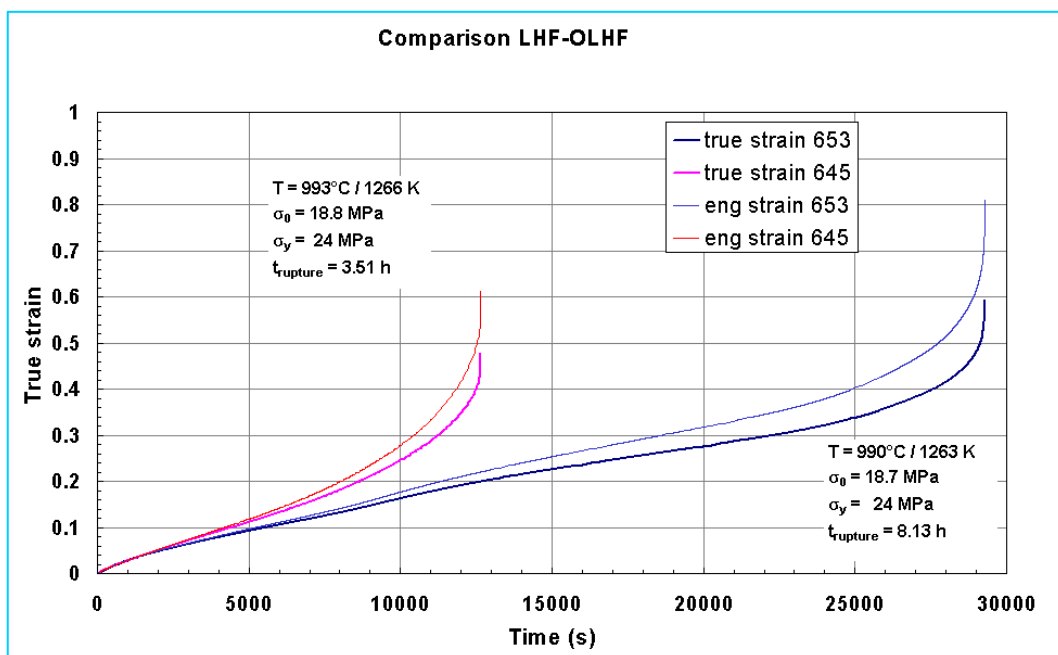
Figure 6-19: Nominal and true creep strain over time of a LHF-test and of an OLHF-test

7 Consideration of a prototypic scenario

Despite of the extensive validation work for the thermal and mechanical modelling approaches and for the coupled simulation it is obvious, that the analysis of a prototypic scenario will involve large uncertainties.

On the one hand there are – beside the scaling ratios – substantial differences between the design of the scaled experiments and a LWR. With respect of the FOREVER-setup, the insulation fixed above the melt and the locally restricted heat generation zone within the melt have to be mentioned here. These differences in the design can be considered in the model easily. In the frame of a sensitivity analysis the impact of these scaling-independent shortcomings of the FOREVER-setup is discussed.

On the other hand there are principal – scaling dependent – differences. Due to these differences for certain phenomena, which play an important role for the prototypic case, an exact validation is perhaps impossible. As mentioned in chapter 2, the main difference between FOREVER and the prototypic case is the partial ablation of the vessel wall in the latter case. In chapter 7.2 the modelling of this process is described.

The considerations on the prototypic scenario following in chapter 7.3 should therefore be regarded as based on the current knowledge and on current code development stage, which has to be further improved.

7.1 Sensitivity studies at the 1:10 Model

When converting the simulation model from the FOREVER-scenario to a prototypic KONVOI-scenario with a completely relocated core and without reflooding, many input parameters are changing simultaneously. The results of the prototypic case are quite different from the FOREVER-results. It will not always be possible to assign a certain effect to its cause. Therefore the FOREVER-model has been changed towards a prototypic model stepwise. Additionally, in going this "evolutionary way" from the FOREVER-model to the prototypic case it was possible to check out the newly implemented single models or boundary conditions separately for their reliability and plausibility.

Therefore in a first step information about the consequences of single important model changes is gathered in a transferability investigation. For this purpose a FOREVER reference scenario is defined and calculated. In comparison to this reference scenario the first significant model change considers the removal of internals like insulation and heating equipment. Another change concerns the heat release zone. In all these investigations the geometrical scale of 1:10 is preserved, thus only influences of the design are highlighted, but not the scaling influences.

7.1.1 Reference calculation

For the reference calculation those boundary conditions have been selected, which were designated for the FOREVER-experiments: a constant heat generation rate of 38 kW in the melt pool and after reaching a stationary temperature field a differential pressure load of 25 bar (cf. chapter 5.3).

The results of the reference calculation are listed in Table 7-1 together with the results of the sensitivity analysis. Due to the time dependent expansion of the vessel there is a changing temperature field – despite the fact of a constant heat generation

rate. The maximum vessel wall temperature amounts to 1 357 K at the beginning and drops to 1 289 K during the calculation at the failure time of 21 150 s.

The maximum external vessel wall temperature and the maximum internal wall temperature can be found approximately at the same height. The difference between both temperatures corresponds indirectly to the maximum heat flux, which is, however, calculated from the hot spot surface temperature, the ambient temperature, the HTC and the emissivity.

The temperature at the centre of the melt pool surface gives an orientation about the general circumstances for the radiative heat transfer to the upper part of the vessel. But the temperature is not a reliable indicator for the total heat flow from the melt surface. In the reference calculation the temperature drops after the first thermal expansion from 1608 K to 1536 K, but the heat release from the melt surface increases from 9.26 kW to 11.93 kW. This reverse trend can be explained by the increase of the melt surface and the enlargement of the empty space above the melt due to the melt level drop. Thus a higher heat flow at a lower temperature is possible.

7.1.2 Vessel without internals

For the prototypic scenario it is assumed that the core is nearly completely relocated to the lower head. Therefore it can be supposed that there is a large hollow space above the melt pool. This constellation is not represented by the FOREVER-tests, because there was an insulation above the melt to protect the upper internals and to limit the required heat generation rate.

If the FOREVER-vessel is simulated without internals, clearly lower temperatures can be expected when all other boundary conditions are unchanged. This is approved by the values for the maximum wall temperature of 1 279 K and 1 211 K for the beginning of the calculation (Table 7-1). The first value refers to the unexpanded vessel, the second to the thermally expanded vessel. Due to the large empty space within the vessel above the melt the corresponding temperatures of the "no-internals" scenario are more than 100 K lower than in the reference scenario. But the total heat flux is clearly increased in both cases: before and after the thermal expansion of the vessel.

Due to the lower temperatures the failure time is more than four times longer than in the reference calculation. The following temperature drop down to 1 207 K is then comparably moderate. This can be explained by a change of the ratio between the radiative heat flux from the melt surface and the heat flux through the vessel wall. Without insulation the part of the heat flux released from the melt surface is significantly increased. Since the increase of the melt surface is mainly caused by the thermal expansion – and not so much by the viscoplastic deformation of the vessel wall – the first temperature drop is much larger than the second one.

7.1.3 Homogeneous heat release in the whole melt

Another model change is related to the heat release. In the experiment the heat was generated by the electrical resistance of the looped heater rod immersed into the melt pool. The spatial region, where the heater loops were located, was a spherical space smaller than melt pool. The heater region was made smaller to avoid a short current between the heater rod and the vessel wall. In the FE-model for the FOREVER-tests the heat generation was modelled as homogeneously distributed in the smaller hemisphere within which parts of the heater are located: the so called "heat release zone". The good agreement of the calculation results with the experi-

mental results justifies this approach. Especially for the temperature field within the vessel wall the approach is validated.

Unlike to this, in the prototypic case the heat release is assumed to be uniformly within the homogeneously mixed melt region. If a uniformly distributed heat release within the whole melt is assumed for the FOREVER-scenario, a lower heat generation density than before has to be taken. Therefore the heat release in the very bottom layer causes a higher heat release through this relatively cold part of the vessel wall. As it could be expected, the maximum temperatures in the vessel wall are lowered. The values of 1 349 K and 1 309 K at the beginning of the calculation shown in Table 7-1 are slightly lower than in the reference calculation. Also the corresponding melt pool surface temperatures and heat fluxes are lower than in the reference scenario, since a larger part of heat is released through the bottom. The subsequent temperature drop during the coupled simulation is somewhat greater than in the reference run, because the effect of the higher heat release through the lower parts of the vessel is becoming stronger the deeper the melt level drops. The reason is, that the heater element in the FOREVER-tests is fixed to the upper part of the vessel. The more the lower head and the melt level are lowering the smaller becomes the heat releasing zone and the larger becomes the vertical distance between the heater and the vessel south pole. The failure time in case of the uniformly distributed heat release is prolonged approximately by 20 % due to the lower temperatures in the hot focus.

7.1.4 Combination of homogeneous heat release and missing internals

The combination of the 2 discussed model changes concerning the heat release area and the missing internals should give even lower temperatures and therefore later failure times. The calculated maximum wall temperatures are 1 274 K and 1 199 K at the beginning of the analysis. The melt pool surface temperatures and heat fluxes lie just below the values of the calculation without internals but with the smaller heat release zone. The maximum wall temperature is dropping only slightly to 1 195 K until vessel failure. The failure time is more than 100 000 s.

7.1.5 Summary of the Sensitivity studies

Table 7-1 summarizes the results of the transferability calculations. Additionally the results of the calculation with the one-way coupling are shown (section 5.3) to underline the importance of the sequentially coupled model. For the one-way coupling the temperature field is not changing since there is no feedback from the mechanical calculation to the thermal calculation.

It can be stated that especially the effect of a large hollow enclosure space above the melt leads to a significant temperature drop and thereby to clearly later failure times. As the figures indicate, the change of the geometry and the boundary conditions causes quite different temperatures in conjunction with the changing heat fluxes through the vessel wall and from the melt pool top surface respectively. In principle it becomes clear once more, that temperature changes of a few percent in the area of the hot focus can lead to very large failure time changes in the time to failure.

Table 7-1: Summary of the variation calculations of the sensitivity analysis

Quantity	Stage	Reference calculation	One-way coupling	No internals	Homog. heat	No internals Homog. heat
$T_{W,max}$ [K]	initial	1357	1357	1279	1349	1274
	ther. exp.	1320	1357	1211	1309	1199
$T_{W,ext,max}$ [K]	initial	1282	1282	1215	1276	1211
	ther. exp.	1250	1282	1155	1249	1145
$q_{W,max}$ [kW/m²]	initial	124.2	124.2	101.1	121.7	99.9
	ther. exp.	112.6	124.2	85.5	112.3	80.8
$T_{MS,center}$ [K]	initial	1608	1608	1485	1583	1465
	ther. exp.	1536	1608	1392	1518	1370
$Q_{MS,max}$ [kW]	initial	9.26	9.26	13.58	8.80	12.96
	ther. exp.	11.93	9.26	17.20	11.32	16.34
$T_{W,max}$ [K]	at failure	1289	1357	1207	1272	1195
Failure time [s]		21 150	8 550	87 000	25 100	104 000

7.2 Modelling of the vessel wall ablation

The main difference of the prototypic scenario compared to the FOREVER set-up is the significantly higher temperature level. This requires the additional modelling of the vessel wall melting process (ablation). The ablation is considered separately in the thermal and in the mechanical model (cf. chapter 5). Prior to the solution step, in both submodels those elements are selected which have at least one node with a temperature above the solidus temperature of the steel. These elements get the material properties of the adjacent melt region for the thermal solution.

In the mechanical submodel, the molten vessel wall elements get a fictitious material property. The main difference compared to the non-molten vessel wall elements is the Young's modulus, which is reduced by several orders of magnitude. This guarantees, that the mechanical properties of the overall model are corresponding to the non-molten vessel parts, while simultaneously the deformation of the FE-grid is calculated for the molten region, too. Figure 7-1 shows the part of the lower head of the mechanical model. Molten elements are represented in dark colour. In the area of the hot focus the wall thickness reduction due to ablation is slightly less than half of the original vessel thickness. Solidification processes at later times are not considered. On reason is that especially the mechanical material properties of re-solidified areas are unknown.
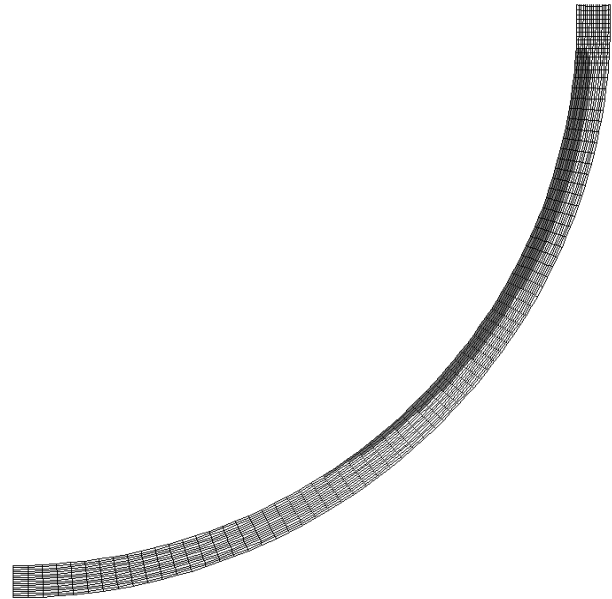
Figure 7-1: Section of the mechanical model under consideration of the ablation. Dark elements are molten

7.3　The prototypic scenario

For the prototypic scenario a pressure water reactor of the size of a SIEMENS-KWU KONVOI-type is considered at a fuel burn-up as high as possible. The RPV of KONVOI-plants is made of the steel 22 NiMoCr 3 7. For this steel a creep data base has recently developed at the MPA Stuttgart. A consideration of these data could not be realized in this current work. This is foreseen in the frame of the future work. Generally the steel 22 NiMoCr 3 7 shows a higher strength as the steels 20 MnMoNi 5 5 or 16MND5, therefore an application of the CDB developed for this weaker steels is considered as conservative.

Subsequently four cases can be distinguished for the prototypic scenario:

- dry low pressure scenario

- dry high pressure scenario

- low pressure scenario with external flooding

- high pressure scenario with external flooding

Already a simple hand calculation shows, that the RPV-wall will fail thermally in any case in the dry scenarios under the considered boundary conditions. For the dry low pressure scenario an analysis has been performed with the coupled model. The result confirms the simple estimation: the wall will fail solely due to the thermal loading, i.e. the wall will melt through completely due to the high temperatures corresponding to the heat flux.

However, with the current model no predictions can be made concerning the failure time, because the model is not suited for highly transient thermal processes. Instead, a stationary thermal solution is searched for the beginning of the calculation. It is known from earlier analyses, that the temperatures in the melt pool can reach values of up to 3000 K [Park and Dhir 1992]. This temperature level was not reached, instead of this maximum a value of 2650 K was calculated. The reasons for this could be on the one hand that a stationary solution has not been reached and on the other hand the relatively high emissivity coefficients. Because of the results for the dry low pressure scenario an analysis of the high pressure scenario without external flooding becomes unnecessary.

For the scenario with external flooding, a heat flux was applied to the external vessel surface in dependence on the excess temperature against the contacting water. The correlation conforms to the Nukijama curve [VDI 2003]. The critical heat flux was not reached in any flooding scenario, i.e. the external vessel wall temperatures lie in a small range between 373 K and 398 K despite large
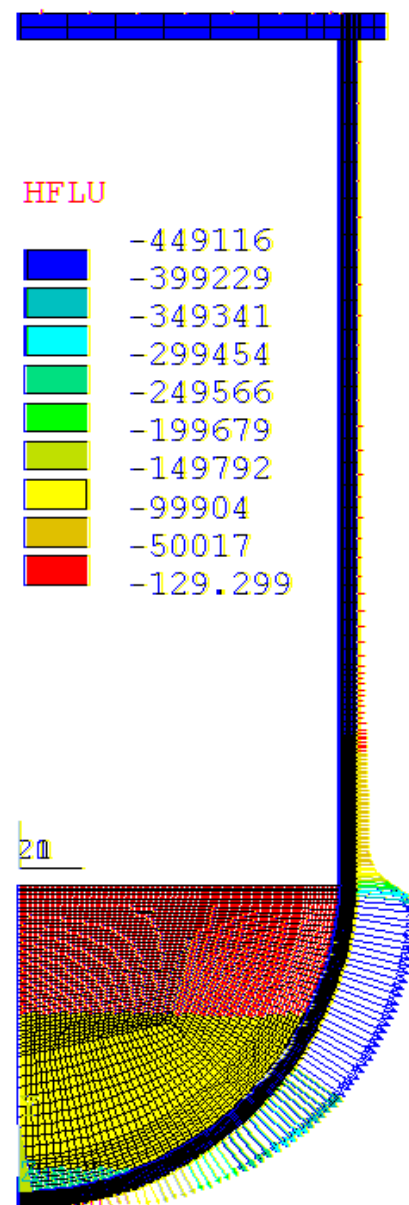
Figure 7-2: Material zones and resulting heat flux [W/m²] at beginning of the prototypic scenario with external flooding

variations of the local heat flux. Contrary to the FOREVER-simulations, where a constant heating power was intended, for the prototypic scenario the consideration of the decreasing decay heat generation becomes necessary. For the analyses discussed here a time dependency as shown in Figure 7-3 is modelled [Kuczera 1993].

For the low and medium pressure scenario constant differential pressures over the RPV-wall between 0 and 25 bar have been assumed. Figure 7-2 shows the element plot of the thermal analysis model. The resulting heat flux at the vessel outside at the beginning of the analysis is represented additionally. The local heat fluxes are calculated iteratively for each load step. The high heat flux in the area of the hot focus is clearly visible. The maximum values are around 450 kW/m². At the lower head south pole and at the high vessel locations in the cylindrical part the resulting heat fluxes are below 50 kW/m².
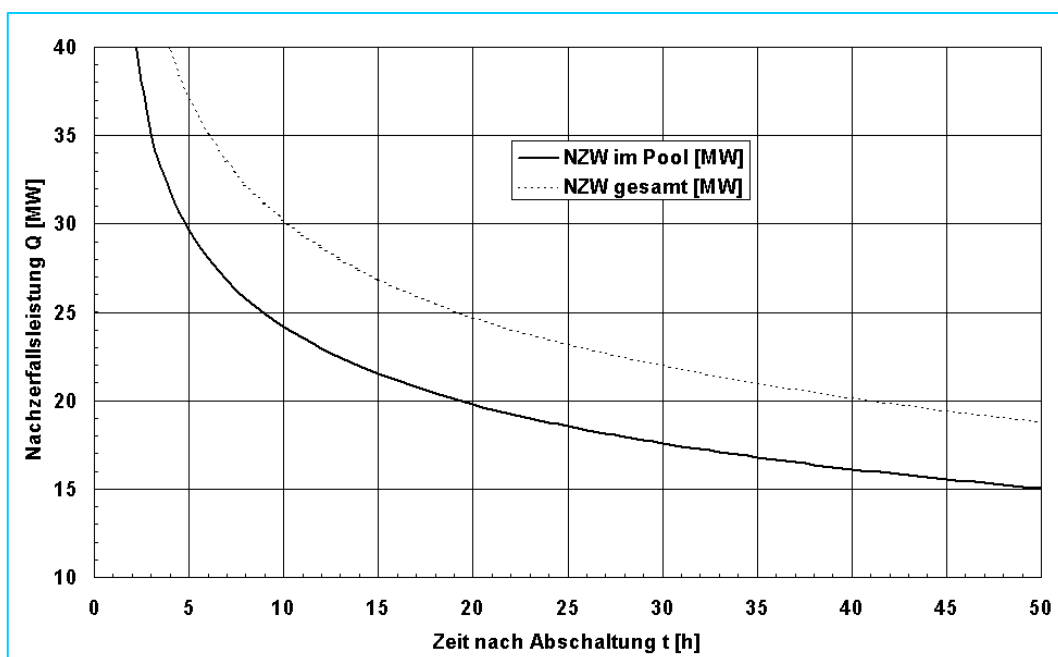
Figure 7-3: Development of the total decay heat generation and of that part which is released within the melt pool (dimensions of a KONVOI-reactor at high burn-up) versus time

TEMP

373.026
608.975
844.923
1081
1317
1553
1789
2025
2261
2497
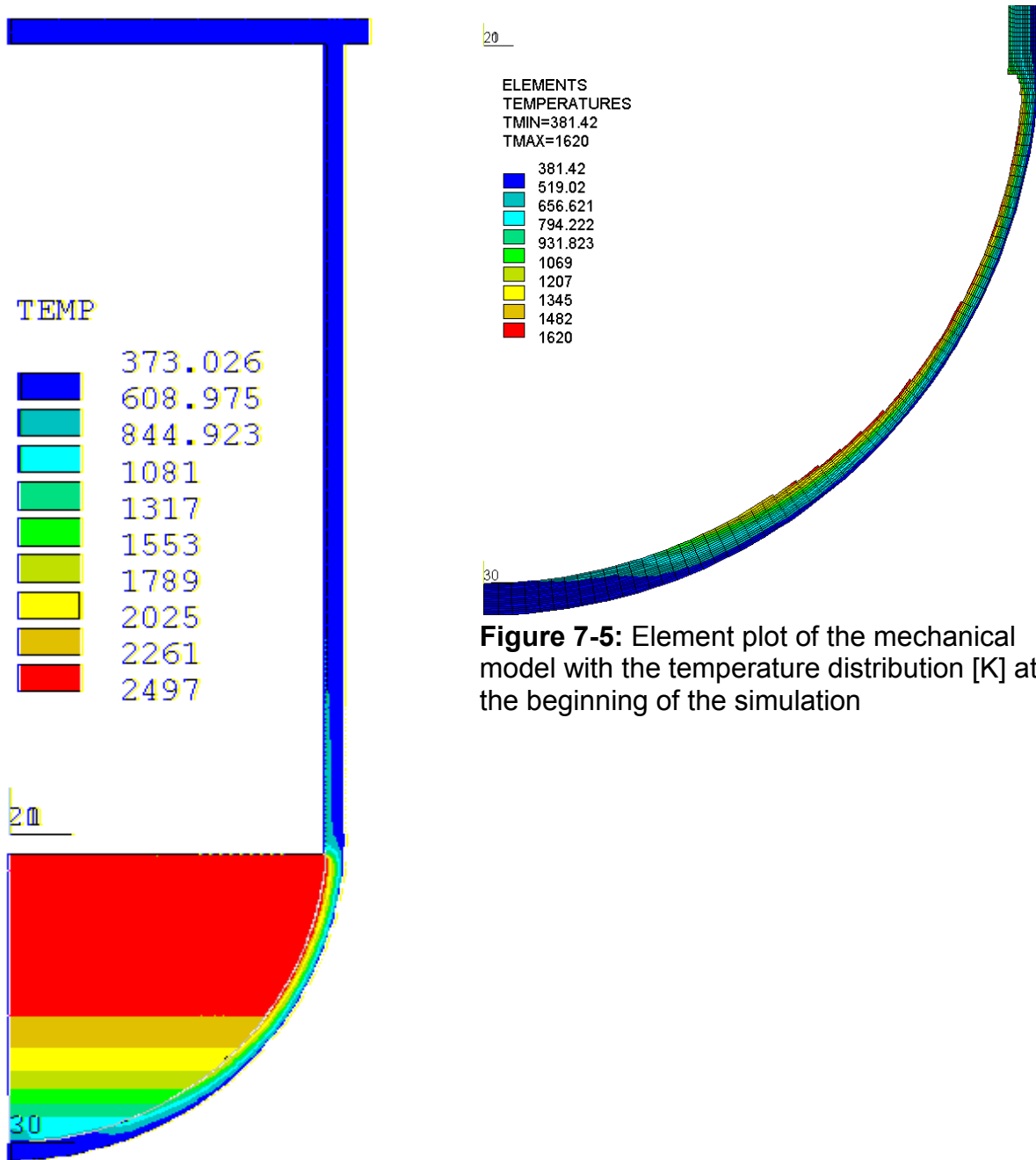
Figure 7-4: Temperature distribution [K] of the whole model at the beginning of the simulation

ELEMENTS
TEMPERATURES
TMIN=381.42
TMAX=1620

381.42
519.02
656.621
794.222
931.823
1069
1207
1345
1482
1620

Figure 7-5: Element plot of the mechanical model with the temperature distribution [K] at the beginning of the simulation

In Figure 7-4 the resulting temperature field is shown for the whole thermal model. The calculated temperature fields are nearly independent of the pressure load. The already known influence of the emissivity coefficient becomes stronger at higher temperatures. For the analyses discussed here a coefficient of 0.8 was assumed.

In the mechanical calculations it was observed, that the residual wall thickness is sufficient to withstand the resulting mechanical loads permanently even at a differential pressure load of 25 bar. Therefore in the following the 25-bar-scenario is discussed. Figure 7-5 shows the residual wall profile of the mechanical model. The sharp decrease of the wall thickness at the height of the melt level is clearly visible. The prevailing temperature distribution is shown in the figure, too.

After the first transient coupling a maximum displacement of approximately 27 mm is calculated (cf. Figure 7-6). The equivalent stress reaches maximum values of 465 MPa at the vessel outside in the upper area of the hot focus. Even at the prevailing temperatures of less than 600 K this causes a clear transgression of the yield stress and therefore goes along with plastic strain and a damage of the material. Figure 7-8 shows the damage distribution within the lower head. The highest damage of 8.3 % occurs in the upper zone of the hot focus inside the vessel wall and is caused by creep and plasticity.
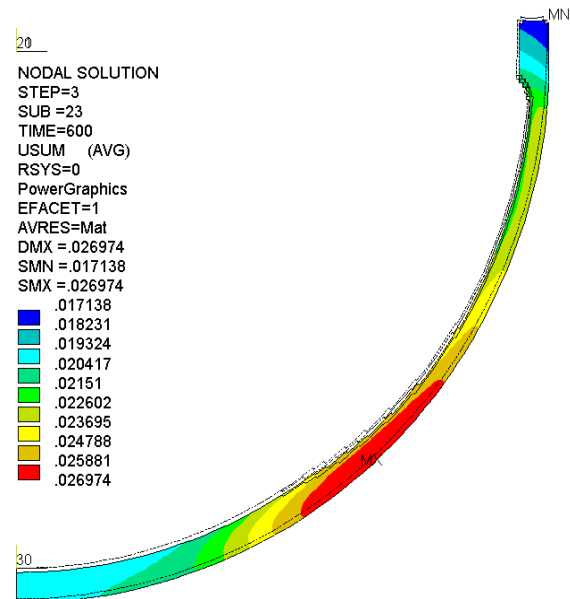
Figure 7-6: Displacement after 600 s

According to the general experience there are no relevant creep processes in the considered RPV steel at temperatures below 700 K. The developed creep data base comprises temperatures above 870 K. In between these two temperatures minor creep processes can take place, however, the stresses would have to be close to the ultimate stress to cause a failure in a time range as considered here (less than 50 h). Creep processes in this temperature range are therefore considered not to be relevant. Instead the plasticity is considered for temperatures from 20 °C.

Figure 7-7 shows the equivalent creep strains for the externally flooded 25 bar scenario at a time of 600 s. Because of the temperature distribution creep takes place only at the area of the vessel inside. The creeping is a typical relaxation process: As soon as the stresses are relocated from the areas with high temperatures into the cooler outer wall region with a much higher strength no further significant creep takes place. Figure 7-9 shows for comparison the creep strain after 25 h. In conjunction with the analysis of the damage distribution after 25 h shown in Figure 7-10, it can be stated, that a successful In-Vessel melt retention in the lower head for a KONVOI-scenario with external flooding and a constant pressure of 25 bar seems possible.

The maximum wall temperature within the mechanically relevant vessel wall parts drops from originally 1620 K to 1100 K after 25 h. This low temperature implies, that after the ablation process at the beginning a solidification must take place at the inner wall surface. However, these solidification processes are not considered for the mechanical strength of the vessel.

It should be mentioned again, that it was considered for this analysis, that at least the heat flux according to the Nukijama-curve can be released from the vessel wall outer surface. It is also presumed that the generated steam mass flow can be released from the reactor pit.

For the high pressure scenario at this time no concluding remarks can be made since the calculations could not be conducted until the desired solution time of at least 25 h, because after the first time steps the plastification becomes rather strong, which is combined with numerical instabilities. The investigations and calculations for this scenario are still going on.
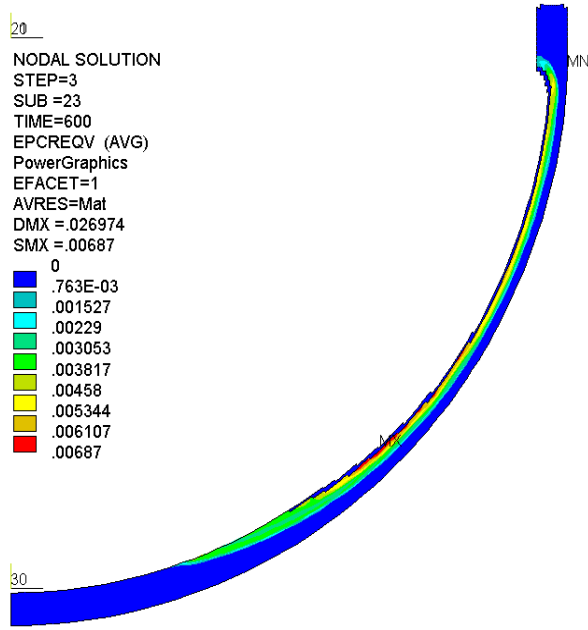
Figure 7-7: Creep strain after 600 s
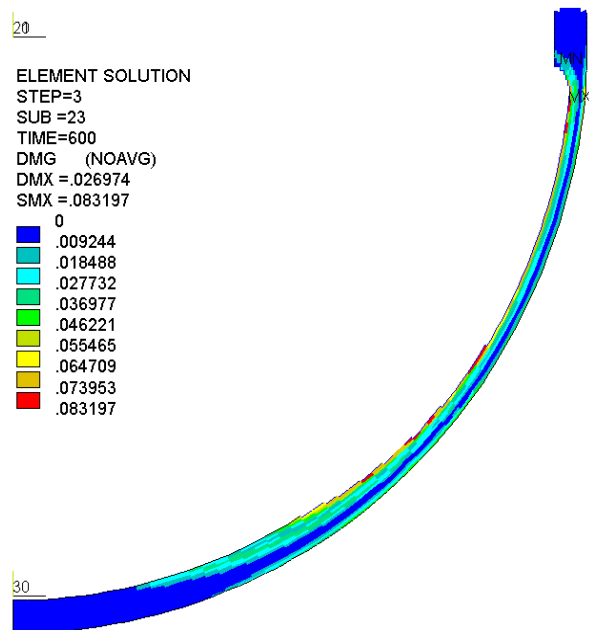
Figure 7-8: Damage after 600 s
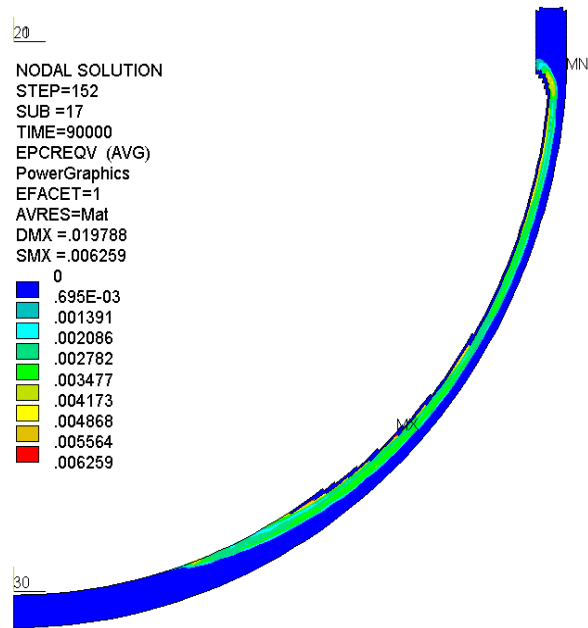
Figure 7-9: Creep strain after 25 h
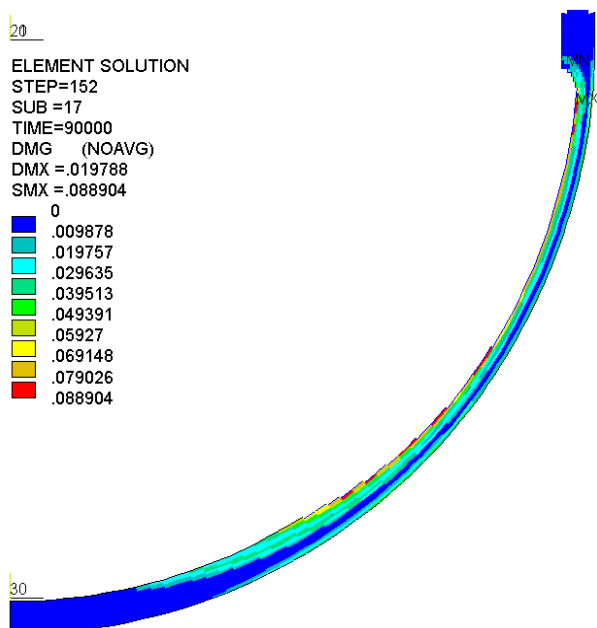
Figure 7-10: Damage after 25 h

8 A possible design for prolongation of the vessel failure time

Evaluating the observations made in the experiments and in the calculations the following conclusions can be drawn:

- The creep process is only initiated by the simultaneous occurrence of high temperatures (>600 °C) and pressure (>1 MPa). At low pressure and high temperature only the reversible thermal expansion is observed, since the dead weight loads of the lower head and the melt pool are negligible. At high pressure and low temperature the material strength is high enough to withstand the pressure load.

- If the creep process is initiated, the weak region is the hot focus area, where the highest local creep strain rate occurs. This leads to wall thinning, which accelerates the creep geometrically.

- The overall temperature level and the pressure level influence mainly the failure time, but not the failure position.

- Failure will occur at the position of highest temperatures. Additionally, there is a small influence of the vertical position of the hot focus region: closer to the cylinder it is more dangerous than at lower positions, since the primary stresses in the cylinder are higher than in the sphere.

- Below the hot focus area there is a large "bowl"-shaped region (lower head bottom centre) exhibiting a relatively high material strength due to the lower temperatures. This bowl keeps its shape and relocates only vertically downwards.

From these insights one can assume that it should be possible to prolong the failure time or even avoid the failure, if the mechanical loads within the weakest region are reduced. A possible arrangement to ensure this is shown in Figure 8-1. On the left the figure shows the vessel at the beginning of a possible in-vessel retention stage after melt relocation to the lower head. A configuration of 3 or more support plates is positioned between the lower head and the basement. In a top view this "creep stool plate"-configuration would look star-shaped. The plates start at the basement, but at the top end they form a gap to the vessel wall, so that the vertical distance becomes constant between the inner- and the outermost radial position. This will ensure that there are no negative influences during normal operation or other accidents.

When the creeping process starts the lower part of the vessel will relocate vertically until the gap is closed. Then a main part of the vertical forces is transferred from the vessel wall to the creep stool plates, as shown on the right side of the Figure 8-1.

Additionally the force of the downward moving vessel can be used to move one or several vertically arranged rods like shown in the figure. This effect can be used to open a gate or a valve to flood the reactor pit with water, e.g. from the In-Containment Water Storage Tank (IRWST), by means of a hydraulic system or other passive mechanical devices. The temperature at the vessel wall outside will be decreased by several hundred degrees and the margin to failure could be increased significantly.

To get an impression about the possible benefits of a creep stool described above, it was assumed that there were one in the FOREVER experiment EC2. In the 2D FE-

model the creep stool is considered as a continuous 360° support, however, this approximation is justified, because the material strength in the lower part is very high, so the gaps between each support plate can be managed by the vessel itself.
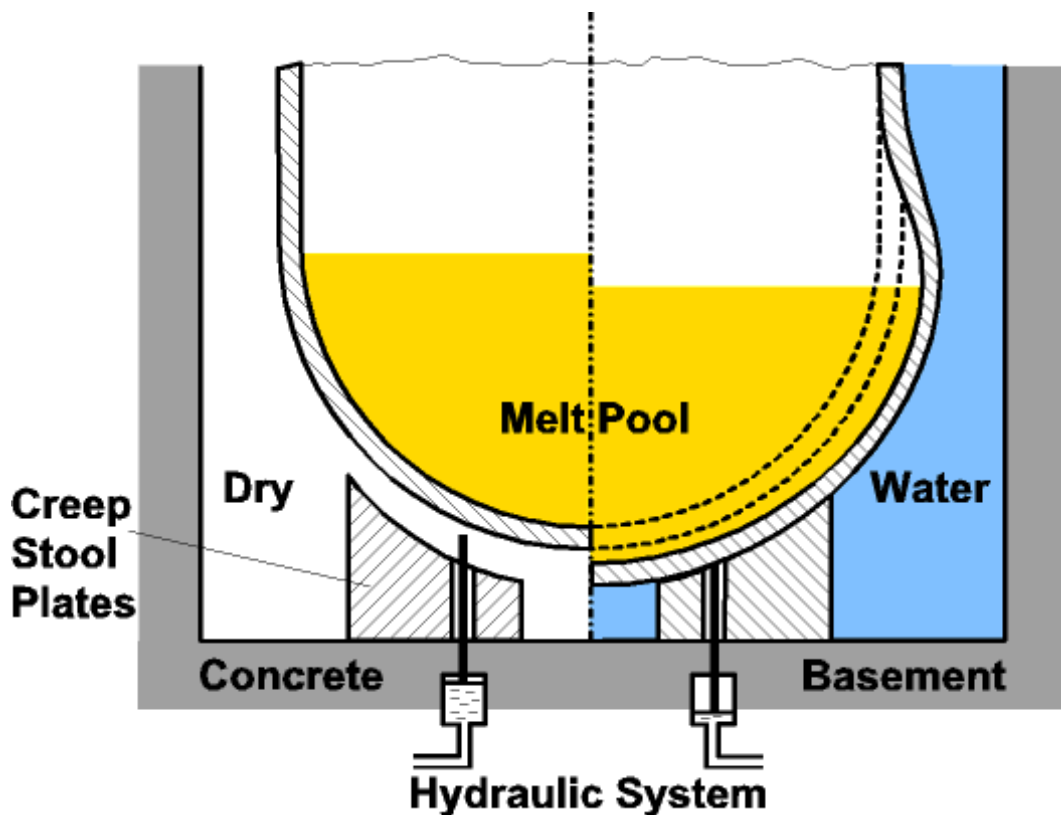
Figure 8-1: Possible arrangement for a vessel support in case of a vessel creep. Additionally a passive control device for the initiation of the reactor pit flooding is shown

A radial gap of 7 mm is modelled between the vessel wall outside and the creep stool. The modelled creep stool extends in polar direction from 5° to 45°, where 0° refers to the vessel south pole. When the gap is closed, contact with friction is assumed, i.e., the surfaces can move against each other in tangential direction.

All other conditions were the same as in the "38kW25bar+5K"-run shown in Figure 6-3. A comparison of the results is given in Figure 8-2, which shows the equivalent stress of the most damaged element in both cases. It is interesting to recognize, that the position of the most damaged element did not change, i.e., the expected failure position is the same. The solid red line represents the calculation without creep stool. The calculated failure time is 3:37 h (the time scale is referred to t=12,360 s in the experiment, which is the starting point for all calculations in Figure 8-2). The calculation shows a slight decrease of the stress within the first 30 min, which is a consequence of stress relocation. After that the stress increases with some acceleration until failure.

Contrary to this the calculation entitled "with stool +5K", which represents the behaviour with creep stool, shows a decreasing stress level after the first 40 min. The stress level decreases or keeps relatively constant over 4 h, then it increases slowly over 2:20 h and after 7:23 h the vessel fails. The reason for the stress reduction can be explained by the green curve in Figure 8-2. It shows the equivalent stress in an element at the vessel inside at the uppermost position of contact between vessel and

creep stool. It shows clearly the first contact time: after 40 min there is a steep increase of the stress. The stress is relocated to that zone of the vessel wall, which is in contact with the creep stool. But this range has a much lower temperature and therefore a much higher strength, so it is not in danger to fail.

According to this simple calculation it can be assumed that a doubling of the failure time is possible, if the stress at the weakest positions of the wall is reduced by a simple vessel support of the vessel bottom centre area. In this scenario the flooding of the reactor pit is not even considered. Finally the shape, including the local creep strain, and the damage of the vessel at failure time are shown in Figure 8-3, which illustrates the different deformation compared to that in Figure 6-4.

The analyses discussed here led to the application and granting of two patents [Willschütz 2002; Willschütz 2003].
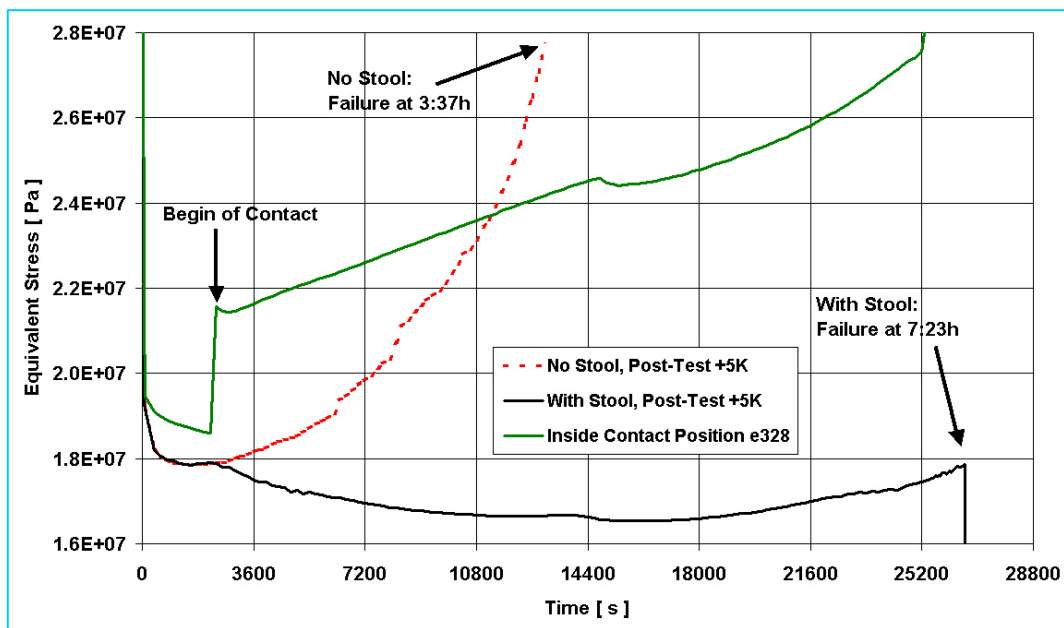
Figure 8-2: Time dependent behaviour of the equivalent stress within the most damaged region with and without creep stool
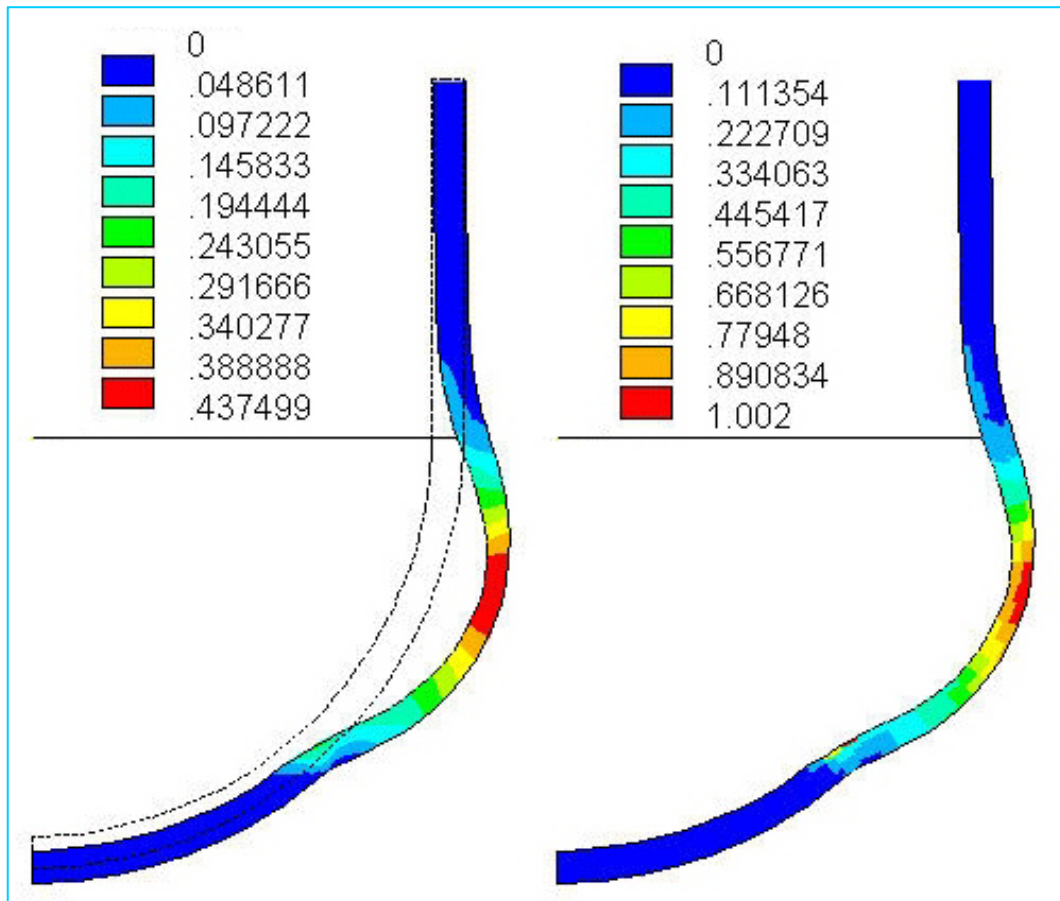
Figure 8-3: Creep strain and material damage at failure time; dry FOREVER-scenario with creep stool

9 Summary and outlook

An integral axisymmetric finite element model has been developed for simulating the late phase of core melt down scenarios in a RPV. The model allows for the calculation of the failure time and the failure mode of a vessel with a heated melt pool. In the thermal submodel the transient temperature field of the melt and of the vessel wall is evaluated. This can be done either with a CFD model or with the Effective Conduction Convection Model (ECCM). Within the mechanical submodel the viscoplastic deformation of the vessel wall is simulated. By use of the material damage the failure time and position can be determined. An additional mechanical submodel is used to evaluate the melt pool deformation. The thermal and the mechanical submodels are recursively and sequentially coupled, i.e. for each time step a thermal dynamic and a mechanical solution is calculated considering a mutual feedback. Besides the temperature dependence of the material parameters and the thermally induced stresses, which are considered in the mechanical model, the consequences of the vessel deformation for the temperature calculation are also included (change of melt pool geometry, melt level drop, change of heat resistance of the vessel wall through thickness reduction, increase of the effective surface for heat radiation and convection).

For the mechanical model a creep data base has been developed based on experimental results of projects of the 4th frame work programme of the EU. The viscoplastic calculation is coupled with the material damage. The creep data base was validated using two pipe rupture experiments.

The coupled model for vessel failure was for pre- and post test calculations of the FOREVER experiments performed at the KTH Stockholm. In general, a good agreement of the calculation and the experimental results could be achieved. The FE model can be considered as validated for medium scaled vessel tests. The main results can be summarised as follows:

- The creep process is caused by the simultaneous presence of high temperature (>600 °C) <u>and</u> pressure (>1 MPa). At low pressure and high temperatures only a reversible expansion can be observed since the loads by the weight of vessel and melt are negligible.

- The hot focus region is the most endangered zone exhibiting the highest creep strain rates. The creep deformation leads to a wall thickness reduction, which accelerates the creep process.

- The failure position is in the zone of the highest temperatures. Additionally the height of the hot focus has an influence on the failure time. Higher melt levels are more dangerous than lower ones, since the primary stresses in the cylinder are higher than those in the sphere.

- The levels of temperature and pressure have an influence on the vessel failure time but not on the failure position.

- The failure time can be predicted with an uncertainty of 20 to 25%. This uncertainty is caused by the large scatter and the high temperature sensitivity of the viscoplastic properties of the RPV steel at higher temperatures.

- Contrary to the hot focus region, the lower centre of the vessel head exhibits a higher strength because of the lower temperatures in this zone. The lower part moves down without significant deformation. Therefore it can be assumed, that the vessel failure can be retarded or prevented by supporting this part.

- The development of a gap between melt crust and vessel wall could not be proved.

The FE model has also been applied to a scenario with LWR geometry. The results of the FOREVER experiments can not be transferred directly to the prototypic conditions. The geometrical, mechanical and thermal relations can not be scaled in the same way. The main difference is the significantly higher temperature level in the LWR scenario, which may lead to a partial ablation of the vessel wall. The main findings from the calculation of the LWR scenario are:

- Without external flooding a pure thermal vessel failure (melt through) is highly probable if the core is completely relocated to the lower head. The viscoplastic behaviour is then of secondary importance. It could eventually accelerate the failure.

- With an external flooding the temperature of the outer RPV wall can be kept in a range, which provides a sufficient mechanical strength for the in-vessel retention at least in the low pressure scenarios (up to 25 bars). However, it has to be ensured that the critical heat flux is not exceeded at any position and that the generated steam can be released from the reactor pit.

- Since the internal heat generation is decreasing with time, it can be assumed on the base of the simulations that the crucial point in time lies within the first 20 hours after melt relocation. If therefore the vessel does not fail in this time frame, it can be assumed, that the vessel will not fail later on.

These results for the LWR case have to be considered as preliminary. Detailed investigations of prototypic scenarios are still necessary. Especially such phenomena have to be considered, which are not existing in scaled experiments with molten salt (FOREVER) or vessels heated by radiation (LHF, OLHF). These are the following:

- segregation of the melt pool (oxide layer and metal layer)

- thermal chemical interaction between corium and RPV wall (ablation, erosion)

- thermo mechanical stresses in RPV wall during late external flooding (thermal shock)

- radiation heat released from the free melt surface

Results of international experiments related to melt segregation and corium steel interaction (like OECD-MASCA and ISTC-METCOR) should be considered when developing further improvements of the simulation model.

10 Literature

Altstadt, E., Th. Moessner. *Extension of the ANSYS® creep and damage simulation capabilities*. Report, FZR-296, Forschungszentrum Rossendorf, Dresden, Germany, 2000.

Altstadt, E.: Extension of the ANSYS® creep, plasticity and damage simulation capabilities. User's manual for the customized ANSYS code, Customisation Revision: 3.3. Forschungszentrum Rossendorf, Dresden, Germany, 2003.

Altstadt, E. and H.-G. Willschütz (2003a): Schmelzerückhaltung im RDB nach Verlagerung von Corium in das untere Plenum. Wissenschaftlich-Technische Berichte / Forschungszentrum Rossendorf; FZR-370, ISSN 1437-322X, März 2003.

Altstadt, E. and H.-G. Willschütz (2003b): Nachrechnung von mittelskaligen Experimenten zum Kriechbruchversagen von Druckbehältern. 2. Workshop "Kompetenzverbund Kerntechnik" vom 18. - 19. 09. 2002 in Köln, Tagungsband.

Altstadt, E. and H.-G. Willschütz (2001): Pre-test Calculations for a Core Meltdown Experiment. Conference Proceedings on CD of the 19th CAD-FEM Users´ Meeting, Potsdam, Germany, 17.-19. Oktober 2001.

Ansys (2001), Programmer's Manual, ANSYS®, Inc., 2001.

Ansys (2003), User's Manual, ANSYS®, Inc., 2003

Asfia, F.J., V.K. Dhir (1996): An experimental study of natural convection in a volumetrically heated spherical pool bounded on top with a rigid wall. Nucl. Eng. Des., vol 163, pp 333-348, 1996.

Asmolov, V. (1998): *Latest Findings of RASPLAV Projekt.* Paper presented at the OECD/CSNI Workshop on In-Vessel Core Debris Retention and Coolability. Munich, 2-5 March 1998.

Azodi, D., Eisert, P.,Gruner, P.,Jendrich, U., Kuntze, W. M. (1996): Verifizierung und internationaler Vergleich von Strukturanalysemethoden zur Beschreibung des Verhaltens des Reaktordruckbehälters bei Belastung jenseits der Auslegungsgrenzen. GRS-A-2338 Forschungsbericht, Februar 1996

Bechta, S.V., V.B. Khabensky, V.S. Granovsky, E.V. Krushinov, S.A. Vitol, V.V. Gusarov, V.I. Almiashev, D.B. Lopukh, W. Tromm, D. Bottomley, M. Fischer, G. Cognet, O. Kymäläinen (2004): New Experimental Results on the Interaction of Molten Corium with Reactor Vessel Steel, Proceedings of ICAPP '04, Paper No. 4114, Pittsburgh, PA USA, June 13-17, 2004

Bernaz, L., J.-M. Bonnet, B. Spindler, C. Villermaux (1997): Thermalhydraulic Phenomena in Corium Pools: Numerical Simulation with TOLBIAC and Experimental Validation with BALI. Proceedings of the KTG/SFEN-Conference: The European Pressurized Water Reactor EPR, Cologne, 19-21 October 1997

Bernaz, L. (1998): Etude du transfert de chaleur à la frontière supèrieure d'un bain fluide avec dissipation volumique de puissance. Dissertation, L'Universite Joseph Fourier De Grenoble, 1998.

Bolshov, L.A., P.S. Kondratenko, V.F. Strizhov (2001): Natural convection in heat-generating fluids. Physics - Uspekhi 44 (10), 999-1016, 2001

Borovkow, A.I., V.S. Granovsky, S.V. Kovtunova, A.S. Semenov (1995): Finite element analysis of thermal stresses of reactor vessel in a severe light water reactor accident. Transactions of the 13th International Conference on Structural Mechanics in Nuclear Technology (SMiRT-13), Porto Alegre, August 13-18 1995

Bothe, K., Maile, K.; Obst, V. (1991): Untersuchungen der Materialeigenschaften unter auslegungsüberschreitenden Bedingungen. Forschungsbericht MPA-Stuttgart Nr. 8705-00-000, März 1991

Bui, V. A. (1998): Phenomenological and Mechanistic Modelling of Melt-Structure-Water Interactions in a Light Water Reactor Severe Accident. Doctoral Thesis at Royal Institute of Technology, Stockholm 1998

Büscher, T., M.K. Koch, H. Unger (1998): Kernschmelzunfälle unter hohem Druck: Szenarien, Schmelzedispersion und Belastung des Sicherheitsbehälters; Technischer Fachbericht RUB E-199 zum BMWi Projekt 1501084, Ruhr-Uni Bochum, 1998

Büscher, T., C. Kortz, A. Voßnacke, M.K. Koch, H. Unger (1999): Abschätzung des radiologischen Quellterms beim HPME/DHC; Technischer Fachbericht RUB E-239 zum BMWi Projekt 1501084, Ruhr-Uni Bochum, 1999

Chu, T.Y., Pilch, M.M., Bentz, J.H., Ludwigsen, J.S., Lu, W.Y., Humphries, L.L. (1999): "Lower Head Failure Experiments and Analyses", Report, NUREG/CR-5582, SAND98-2047, Sandia National Laboratories, Albuquerque, NM, USA.

Dinh, T.N., R.R. Nourgaliev (1997): *Turbulence modelling for large volumetrically heated liquid pools.* NUCLEAR ENGINEERING AND DESIGN, vol 169, pp 131-150, 1997.

Helle, M.; O. Kymäläinen (1998): Crust Effect in the COPO II-Experiments. Report 2_EU-MVI(98)-FORTUM-35, IVO Power Engineering, Vantaa, Finnland, 1998.

Hirschmann, H. (1997): CORVIS-Report No.7, Paul-Scherrer Institut, February 1997.

Horner, P., A.. Zeisberger, F. Mayinger (1998): Evaporation of Coolant at the Bottom of Particle-Bed modelling Relocated Debris; OECD/CSNI Workshop on In-Vessel Core Debris Retention and Coolability, Garching March 3-6, 1998

Humphries, L.L., T.Y. Chu, J. Bentz, R. Simpson, C. Hanks, W. Lu, B. Antoun, C. Robino, J. Puskar, P. Mongabure (2002): OECD Lower Head Failure Project Final Report, Sandia National Laboratories, Albuquerque, NM 87185-1139

Ikonen, K. (1999): "Creep Model Fitting Derived from REVISA Creep, Tensile and Relaxation Measurements", Technical Report MOSES-4/99, VTT-Energy, Espoo, Finland.

IMA (2001): M. Kadner, Prüfbericht Nr. A191/1, Chemical Analysis of a steel specimen, IMA Dresden, 2001.

Kersting, E., Löffler, H. et al. (1998): Sicherheitsanalytische Untersuchungen zu schweren Störfällen in SWR; Abschlussbericht zum BMWi-Vorhaben RS960, GRS-A-2519, Gesellschaft für Reaktorsicherheit, Mai 1998

Köhler, W., H. Schmidt, O. Herbst, W. Krätzer (1998): Experiments on Heat Removal in a Gap between Debris Crust and RPV Wall; OECD/CSNI Workshop on In-Vessel Core Debris Retention and Coolability, Garching March 3-6, 1998

Kolev, N.I. (1996): External cooling of a pressurized water reactor vessel during a severe accident. Kerntechnik 61 (1996), pp. 67-76, Carl Hanser Verlag

Kuczera, B. (1993): Innovative Trends in der Leichtwasserreaktor-Technik. KfK-Nachrichten Jahrgang 25, S. 219-249, 1993

Lemaitre, J. (1996): A Course on Damage Mechanics. ISBN 3-540-60980-6, 2nd edition Springer-Verlag Berlin, Heidelberg, New York, 1996

Mongabure, Ph., M. Desmet (1999): *RUPTHER Test#14 - Rupture test at 1000°C and variable pressure 8 then 6 bars*, Report SEMT/LISN/RT/99-003/A, CEA, France, 1999.

Müller, W. Ch. (2003): Bericht über OECD-RASPLAV und OECD-MASCA Projekte und verfügbare Unterlagen; Arbeitstreffen, GRS Garching, 29.08.2003

Mongabure, Ph. (2000): Creep tests on LHF and OLHF SA533B1 steel. Rapport No. SEMT/LISN/RT/00-060/A, CEA Saclay – DMS2, December 2000

Nourgaliev, R.R., A.T. Dinh, T.N. Dinh, B.R. Sehgal (1998): Numerical Investigation on Turbulent Natural Convection Heat Transfer in an Internally-Heated Melt Poll and Metallic Layer. OECD/CSNI Workshop in In-Vessel Core Debris Retention and Coolability, Munich, March 03-06, 1998

Obst, D., Maile, K. (1989): Versuche zur Schaffung einer Datenstruktur für die inelastische Berechnung von Kriechvorgängen in thermisch belasteten Komponenten. Forschungsbericht MPA-Stuttgart Nr. 8650 00 000, April 1989

Obst, D., A. Klenk, P. Julisch, K. Maile (1988): Versuche zum Versagen einer Hauptkühlmittelleitung infolge Kriechbruch unter hohem Systemdruck, Report MPA 1500 771, Stuttgart, Germany, 1988.

Park, H., V.K. Dhir (1992): Effect of Outside Cooling on the Thermal Behaviour of a Pressurized Water Reactor Lower Head. Nuc. Tech., vol 100, pp 331-346, 1992.

Rempe, J.L., S.A. Chávez, G.L. Thinnes, C.M. Allison, G.E. Korth, R.J. Witt, J.J. Sienicki, S.K. Wang, L.A. Stickler, C.H. Heath, S.D. Snow (1993): Light Water Reactor Lower Head Failure Analysis. NUREG/CR-5642, EEG-2618, Oct. 1993

Sainte Catherine, C. (1998), Tensile and creep tests material characterization of pressure vessel steel (16MND5) at high temperatures (20 up to 1300°C). Rapport SEMT/LISN/RT/98-009/A, CEA, France, (experimental data files), 1998.

Schaaf, K., J. Sievers, C. Müller (1999): Entwicklung und Verifikation von Modellen zur Beschreibung der Wechselwirkung Debris-RDB. Gesellschaft für Reaktorsicherheit, GRS-A-2749, Oktober 1999

Schaaf, K. (1998): Uncertainty and Sensitivity Analysis of the Heat Transfer Mechanisms in the Lower Head; OECD/CSNI Workshop on In-Vessel Core Debris Retention and Coolability, Garching March 3-6, 1998

Sehgal, B.R, V.A. Bui, T.N. Dinh, J.A. Green, G. Kolb (1998a): SIMECO Experiments on In-Vessel Melt Pool Formation and Heat Transfer with and without a Metallic Layer. OECD/CSNI Workshop in In-Vessel Core Debris Retention and Coolability, Munich, March 03-06, 1998

Sehgal, B.R, R.R. Nourgaliev, T.N. Dinh, A. Karbojian, J.A. Green, V.A. Bui (1998b): FOREVER Experiments on Thermal and Mechanical Behaviour of a Reactor Pressure Vessel during a Severe Accident. OECD/CSNI Workshop in In-Vessel Core Debris Retention and Coolability, Munich, March 03-06, 1998

Sehgal, B.R., S.A. Theerthan, H.G. Willschütz, R.R. Nourgaliev, A. Karbojian (2000): Coupled Melt Pool Convection and Vessel Creep Failure: The FOREVER Program. Proceedings of the RASPLAV Seminar 2000, Munich, Germany, 14.-15. November 2000

Sehgal, B.R., Nourgaliev, R.R., Dinh, T.N., Karbojian, A., *FOREVER experimental program on reactor pressure vessel creep behaviour and core debris retention*, Proceedings of the 15-th International Conference on Structural Mechanics in Reactor Technology (SMiRT-15), Seoul, Korea, August 15-20, 1999.

Suh, K.Y., S.H. Chang, H.D. Kim, S.J. Oh, J.I. Lee (1999a): Severe Accident Research Activities in Korea: In-Vessel Retention of Molten Core Material; Transactions of 15th SMiRT Conference, Seoul, August 15-20, 1999; Vol XI P01/1

Suh, K.Y., K.H. Kang, J.H. Kim, S.B. Kim, H.D. Kim, J.S. Cho, J.E. Chang (1999b): Thermal and Mechanical Behaviour of Hemispherical Vessel Lower Head; Transactions of 15th SMiRT Conference, Seoul, August 15-20, 1999; Vol XI P02/3

Theofanous, T.G., C. Liu, S. Additon, S. Angelini, O. Kymäläinen, T. Salmassi (1997): In-vessel coolabilty and retention of a core melt. Nuclear Engineering and Design 169 (1997) pp. 1-48

VDI (2002): VDI-Wärmeatlas, Berechnungsblätter für den Wärmeübergang, Neunte Auflage, Springer-Verlag, Berlin, 2002.

Willschuetz, H.-G. (2004): Simulation of Scaled Vessel Failure Experiments and Investigation of a Possible Vessel Support against Failure. NUCLEAR ENGINEERING AND DESIGN, Vol 228, Issues 1-3, March 2004, Pages 401-414.

Willschuetz, H.-G., E. Altstadt, B. R. Sehgal, and F.-P. Weiss (2003a): Post-Test Calculations of Medium Scaled Pressure Vessel Creep Failure Experiments. Proceedings of the ICAPP, Cordoba, Spain, May 4-7, 2003.

Willschuetz, H.-G., E. Altstadt, B. R. Sehgal, and F.-P. Weiss (2003b): FEM-Calculation of Different Creep-Tests with French and German RPV-Steels. Proceedings of 17th International Conference on Structural Mechanics in Reactor Technology, SMiRT 17, Prague, Czech Republic, August 17-22, 2003.

Willschuetz, H.-G., E. Altstadt, B. R. Sehgal, and F.-P. Weiss (2003c): Simulation of Creep Tests with French or German RPV-steel and investigation of a RPV-support against failure. ANNALS OF NUCLEAR ENERGY, vol 30, 10, pp 1033-1063.

Willschuetz, H.-G. and E. Altstadt (2003): Post Test Calculation of Tube Creep Failure Experiments. Jahrestagung Kerntechnik 2003, Tagungsbericht S.141-146, Berlin, Germany, May 20-22, 2003.

Willschuetz, H.-G. (2003): German Patent DE 100 41 778 C2, Abstützvorrichtung für Stahlbehälter.

Willschuetz, H.-G. and E. Altstadt (2002): Generation of a High Temperature Material Data Base and its Application to Creep Tests with French or German RPV-steel. Wissenschaftlich-Technische Berichte / Forschungszentrum Rossendorf; FZR-353, ISSN 1437-322X, August 2002.

Willschuetz, H.-G., E. Altstadt, B.R. Sehgal, and F.-P Weiss (2002a): Validation of a creep and plasticity model for French and German RPV-steel. OECD Meeting "OLHF Seminar 2002", Steering Committee for Nuclear Energy, Committee on the Safety of Nuclear Installations, Madrid, Spain, June 26-27, 2002.

Willschuetz, H.-G., E. Altstadt, F.-P. Weiss, and B. R. Sehgal (2002b): Scaled Vessel Failure Experiment Analysis and Investigation of a Possible Vessel Support. Jahrestagung Kerntechnik 2002, Tagungsbericht S. 173-178, Stuttgart, Germany, May 14-16, 2002.

Willschuetz, H.-G., E. Altstadt, B. R. Sehgal, and F.-P. Weiss (2002c): Analysis and insights about FE-Calculations of the EC-Forever-Experiments. Conference Proceedings on CD of the 10th International Conference on Nuclear Engineering, Arlington, Virginia, USA, April 14-18, 2002

Willschuetz, H.-G.; E. Altstadt, B. R. Sehgal, and F.-P. Weiß (2002d): Simulation of Scaled Reactor Pressure Vessel Creep Failure Experiments. Paper to the participants of NUSIM 02, 11th annual Nuclear Societies Information Meeting, Dresden, Germany, March 13-15, 2002.

Willschuetz, H.-G., E. Altstadt, B.R. Sehgal, and F.-P Weiss (2001): Coupled thermal structural analysis of LWR vessel creep failure experiments, NUCLEAR ENGINEERING AND DESIGN, vol 208, pp 265-282, 2001.

Willschuetz, H.-G. (2002): German Patent DE 100 41 779 C1, Steuereinrichtung für einen Kühlkreislauf.

Appendix A1: Figures of FOREVER-Experiments
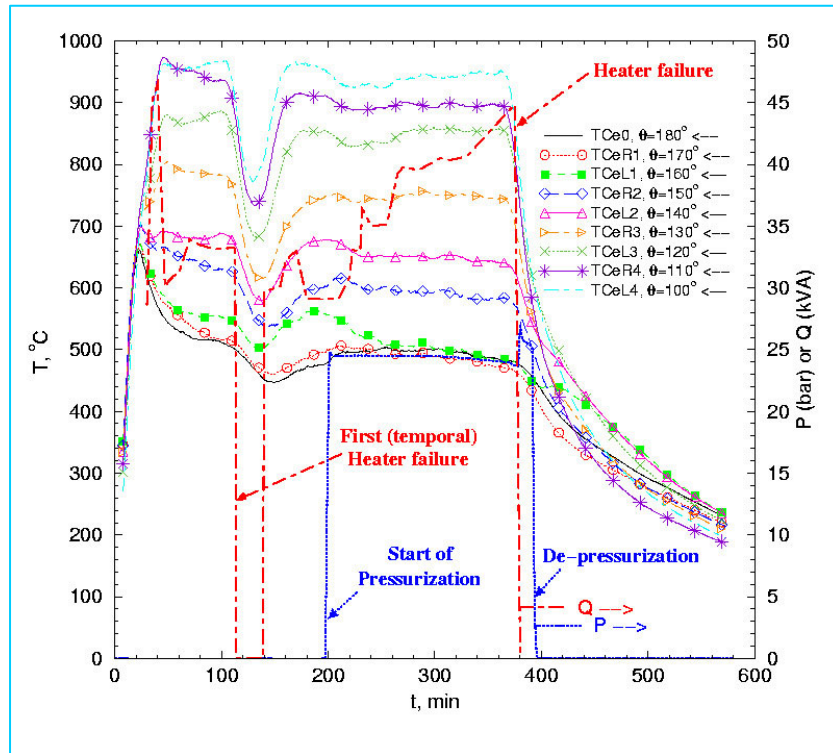
Figure A 1: External wall temperatures vs. time; experiment FOREVER-C2; 180° – south pole
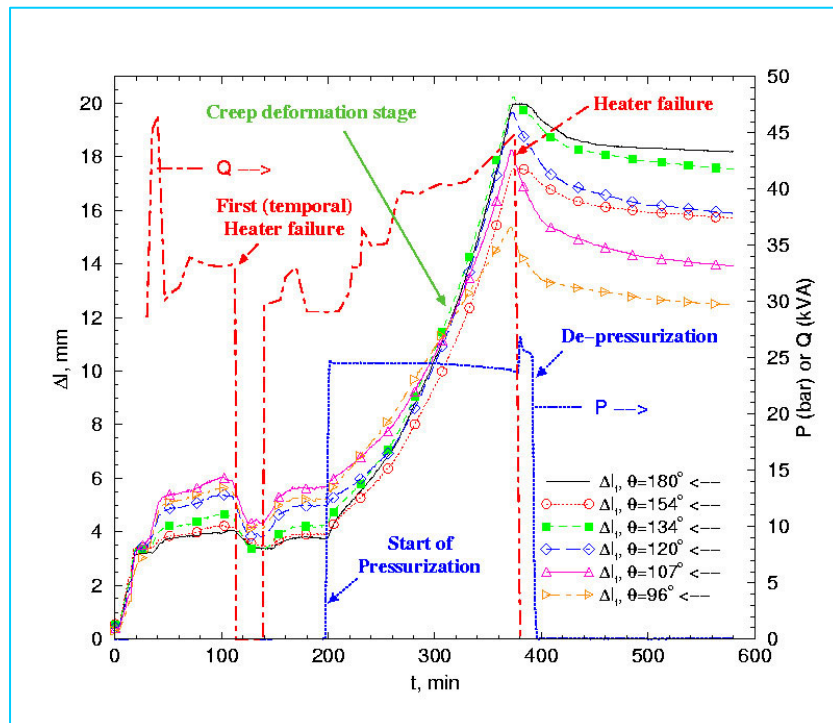
Figure A 2: Vessel displacements vs. time; experiment FOREVER-C2; 180° – south pole
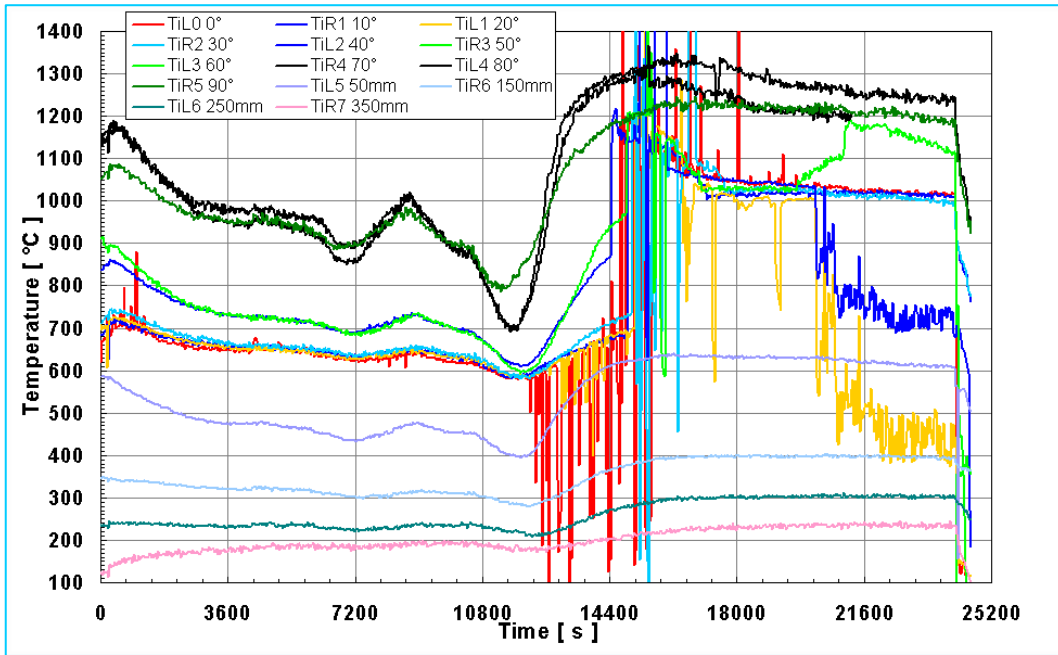
Figure A 3: Internal temperatures vs. time; Experiment FOREVER-EC2; 0°–south pole
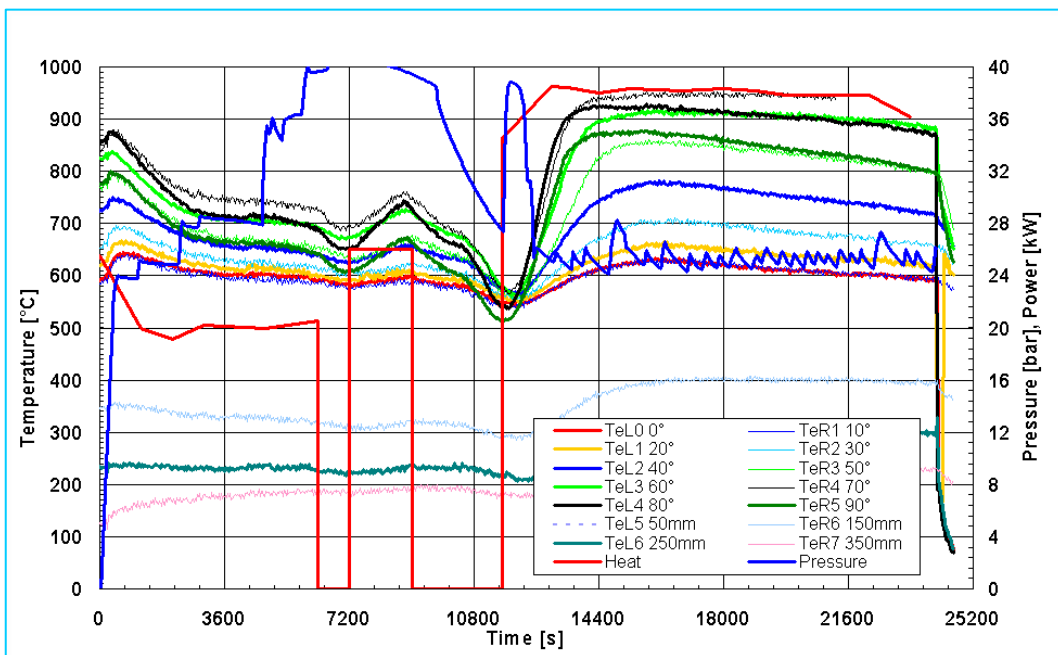
Figure A 4: External wall temperatures vs. time; Experiment FOREVER-EC2; 0°–south pole
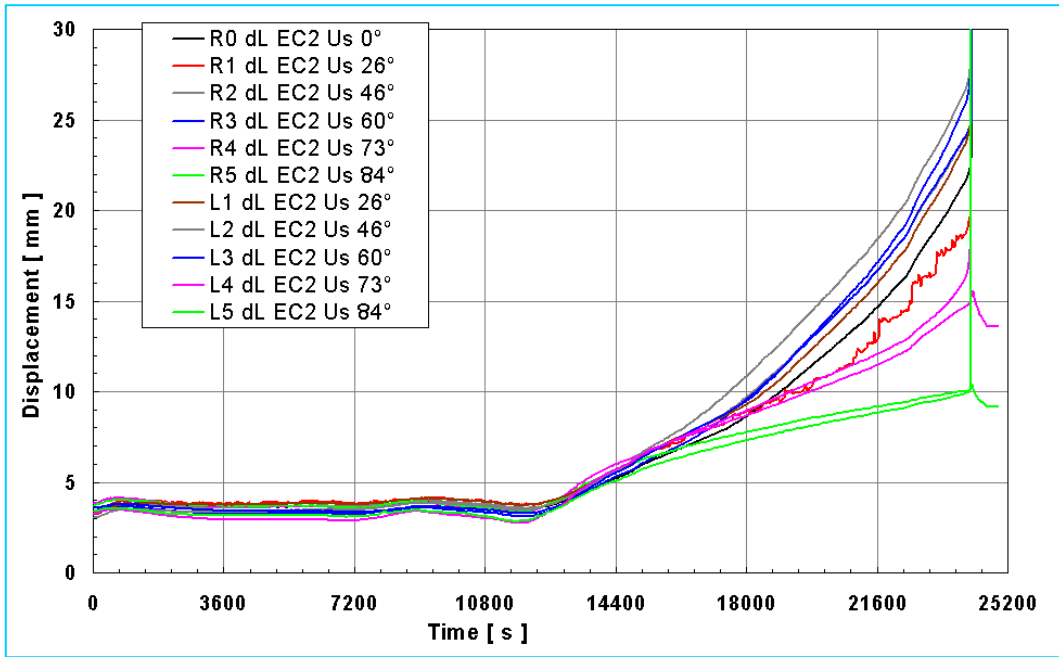
Figure A 5: Displacements vs. time; experiment FOREVER-EC2;
0°–south pole
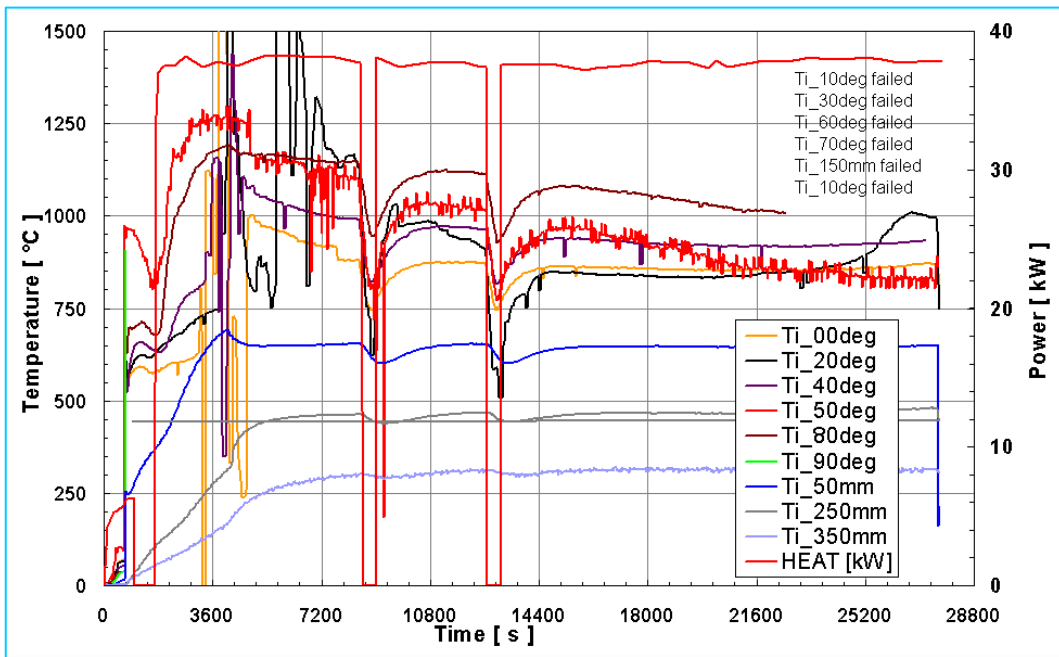
Figure A 6: Internal temperatures; experiment FOREVER-EC3b;
0°–south pole
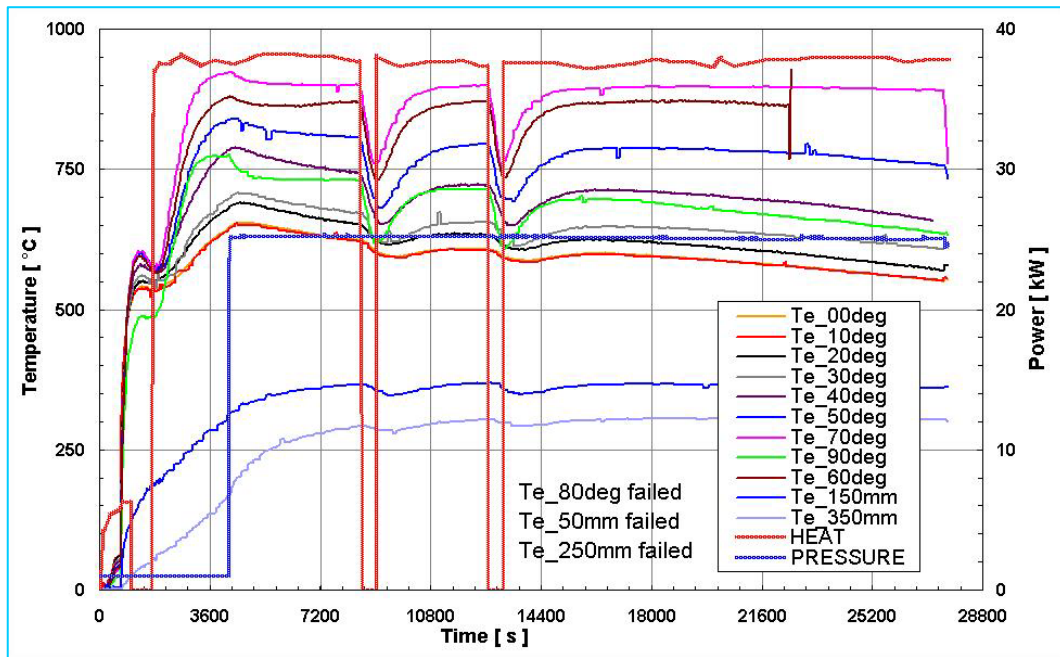
Figure A 7: External wall temperatures; experiment FOREVER-EC3b; 0°–south pole
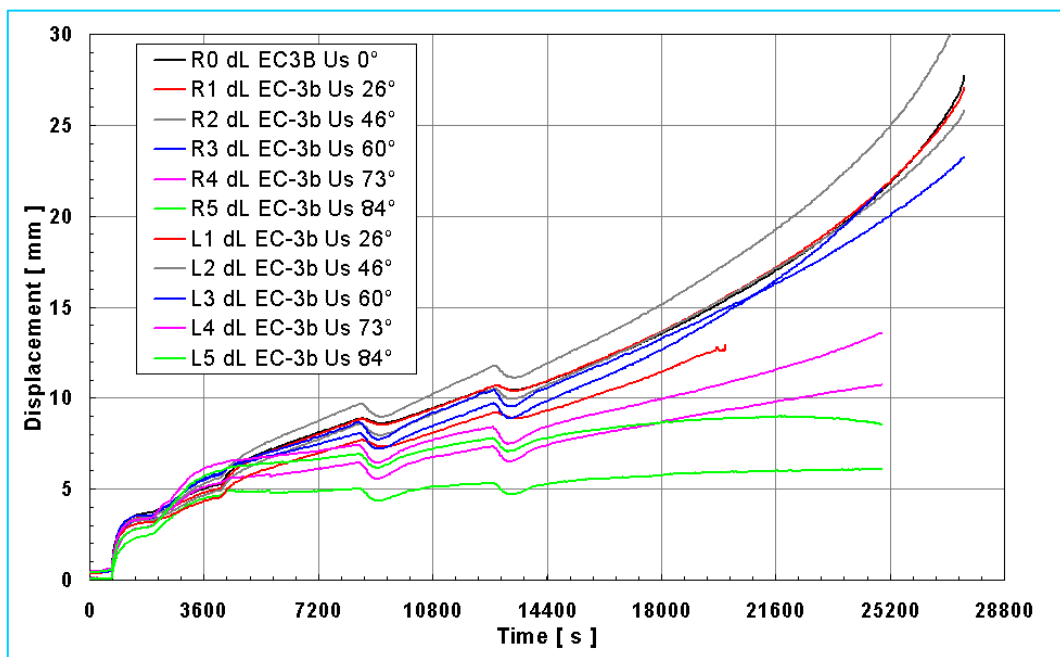
Figure A 8: Displacements vs. time; Experiment FOREVER-EC3b; 0°–south pole
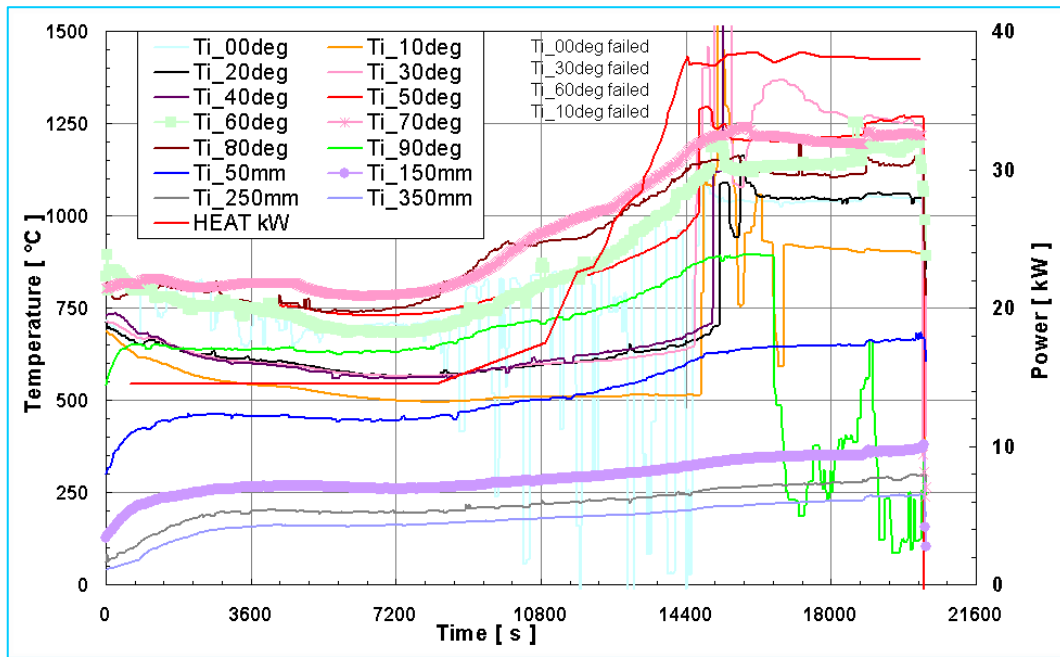
Figure A 9: Internal temperatures; experiment FOREVER-EC4; 0°–south pole
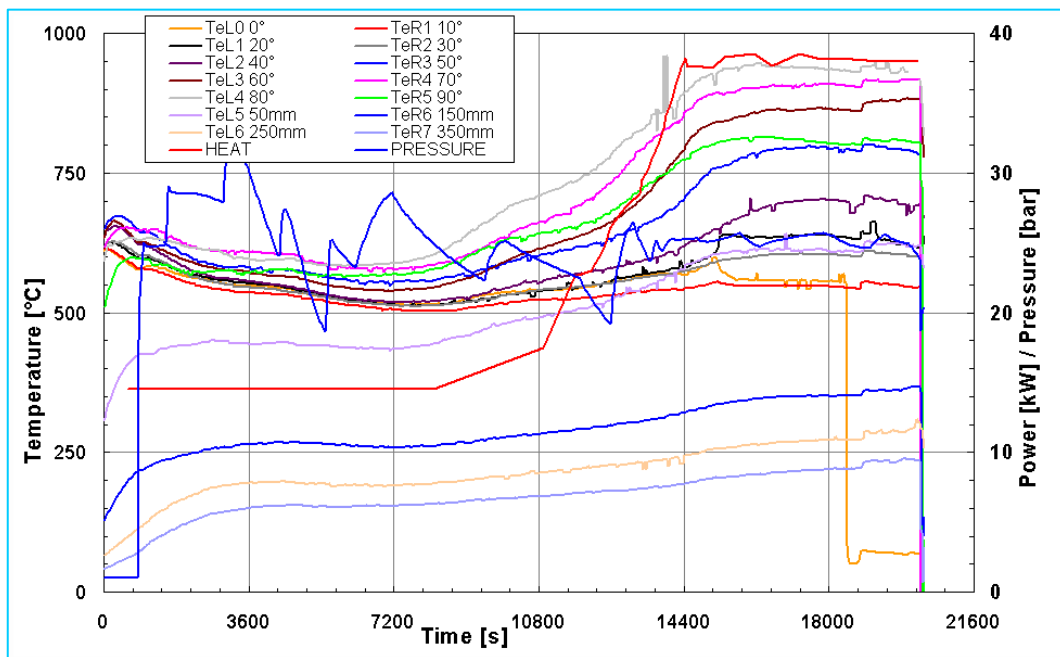
Figure A 10: External wall temperatures; experiment FOREVER-EC4; 0°–south pole
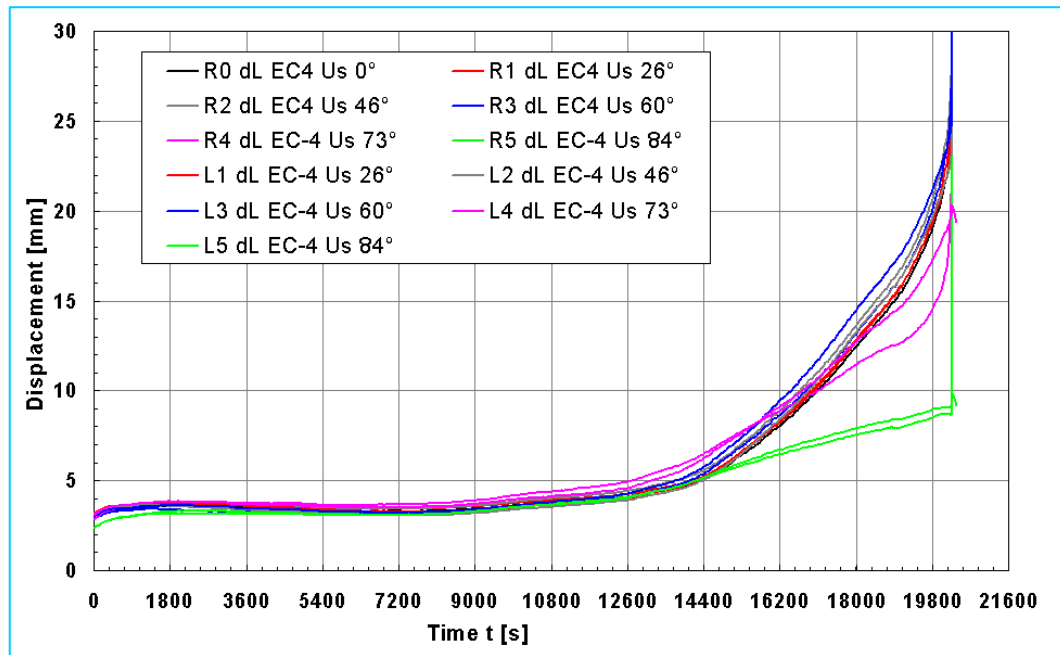
Figure A 11: Displacements vs. time; experiment FOREVER-EC4; 0°–south pole

Figure A 12: Specimens of the vessels of the experiments C1 through EC5
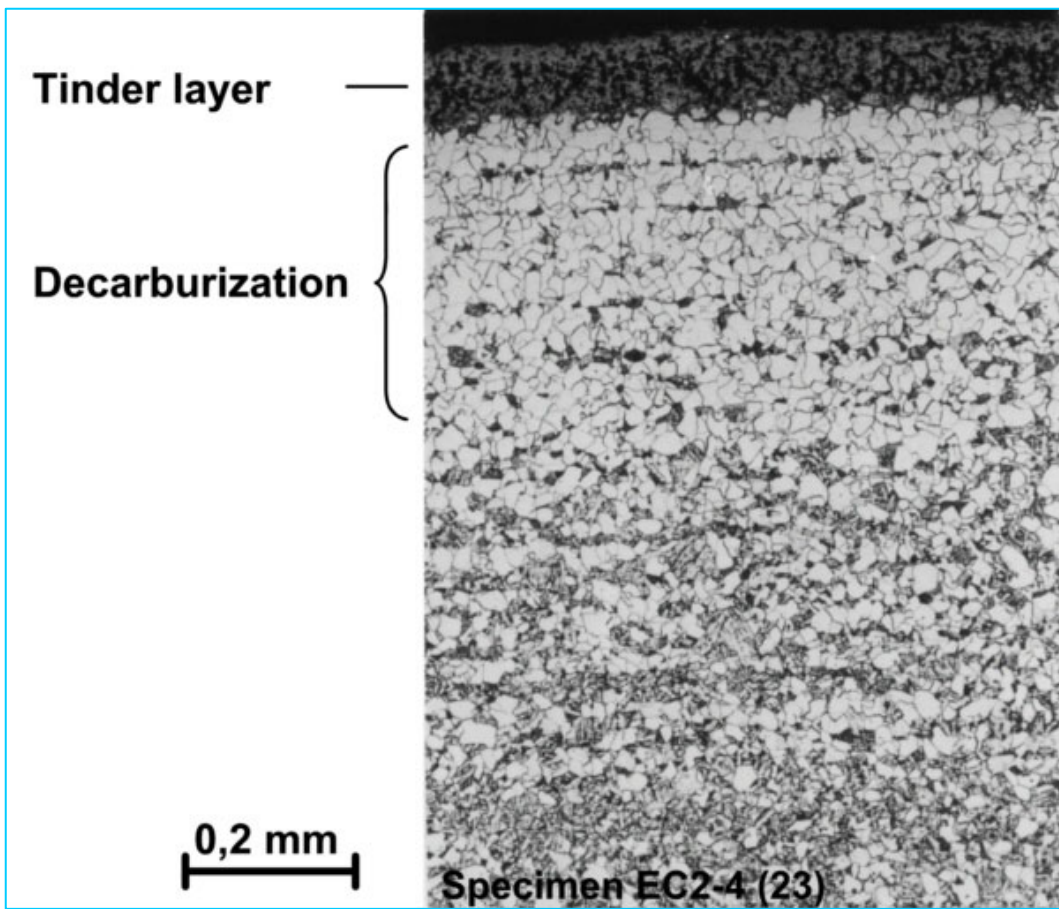
Figure A 13: Metallographic picture of a specimen of EC2, outer wall zone

Appendix A2: Figures of the material data base
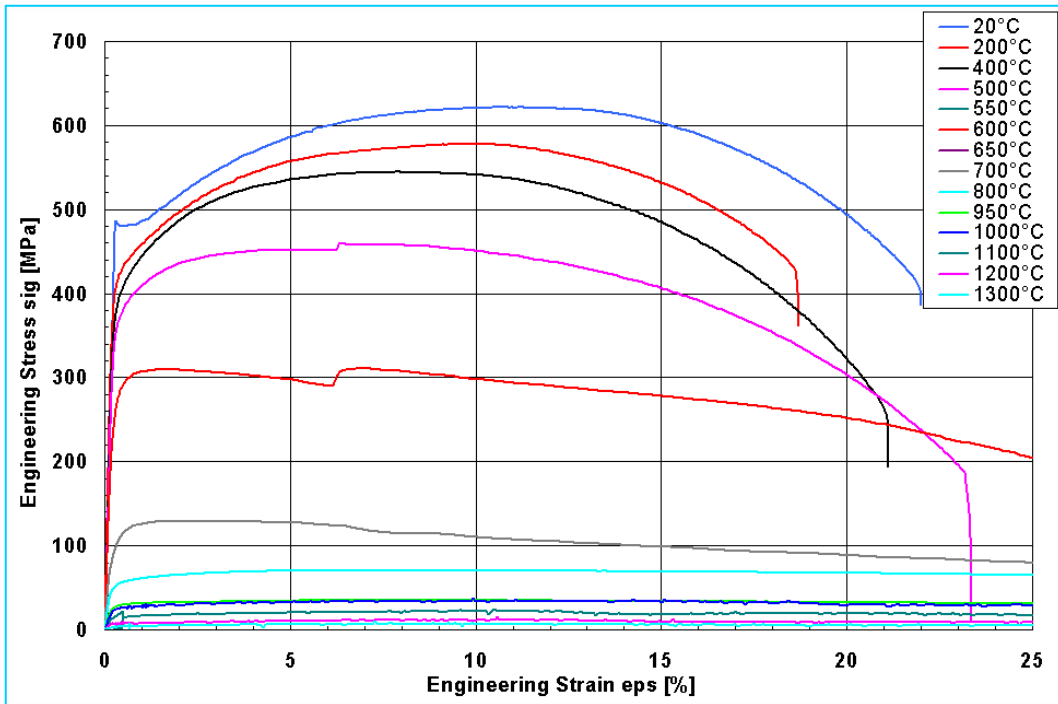
Figure A 14: Nominal stress-strain curves of the RPV steel 16MND5 at different temperatures (CEA-Measurement)
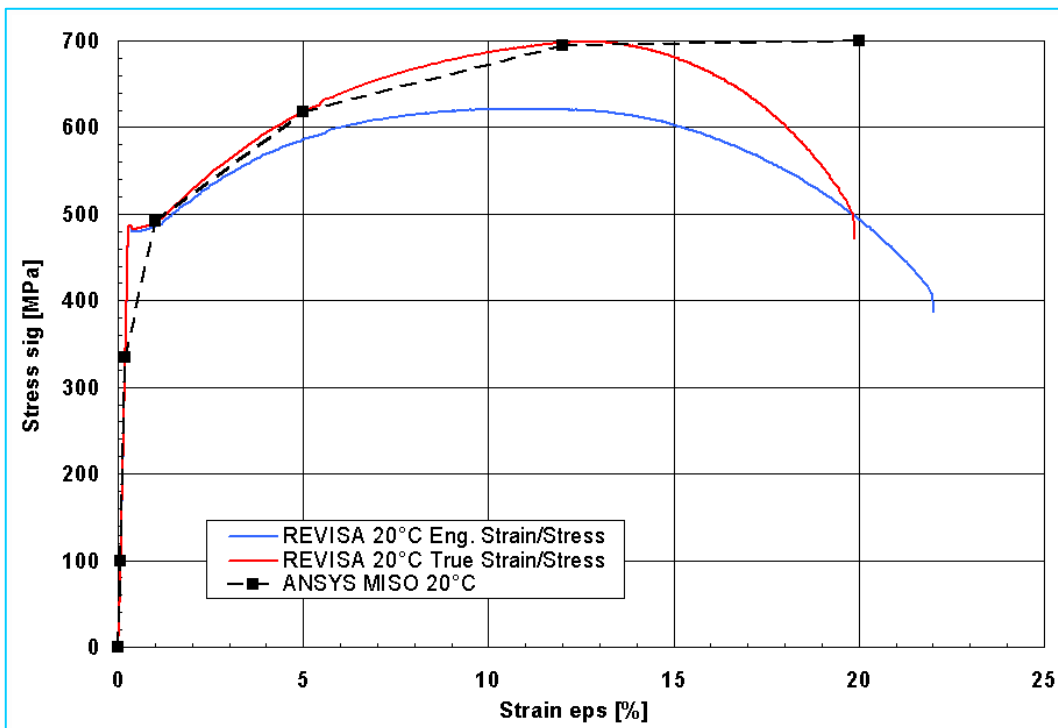
Figure A 15: Stress-strain curves of the RPV steel 16MND5 at 20 °C; CEA-Measurement and Modelling in ANSYS
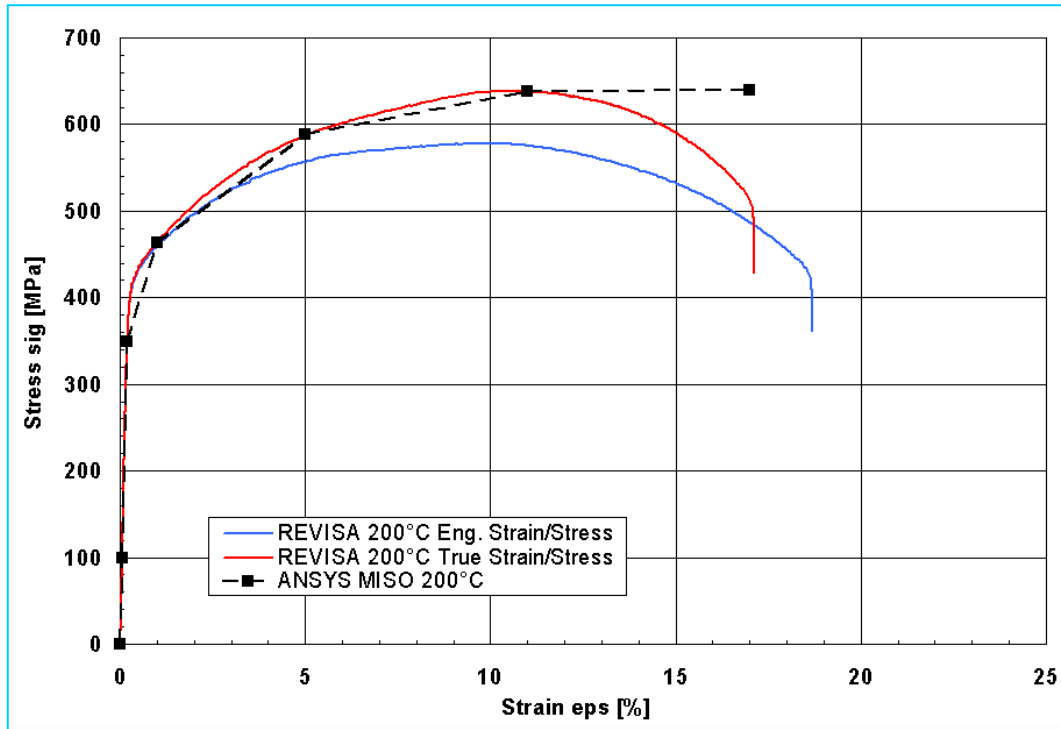
Figure A 16: Stress-strain curves of the RPV steel 16MND5 at 200 °C;
CEA-measurement and modelling in ANSYS
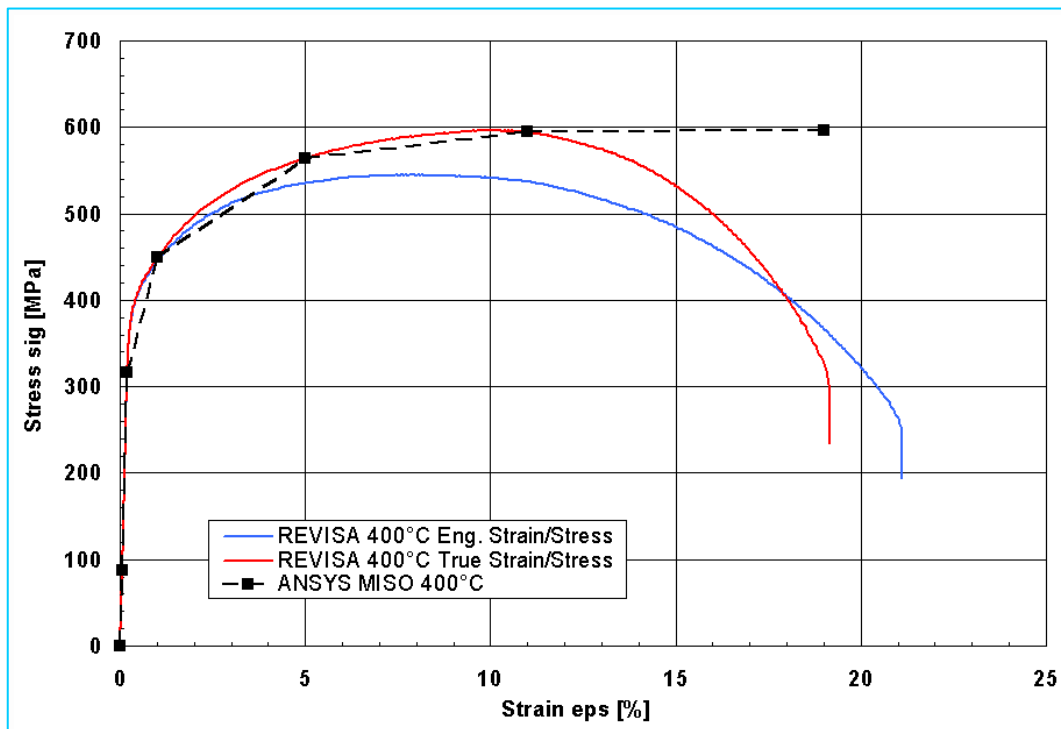
Figure A 17: Stress-strain curves of the RPV steel 16MND5 at 400 °C;
CEA-measurement and modelling in ANSYS
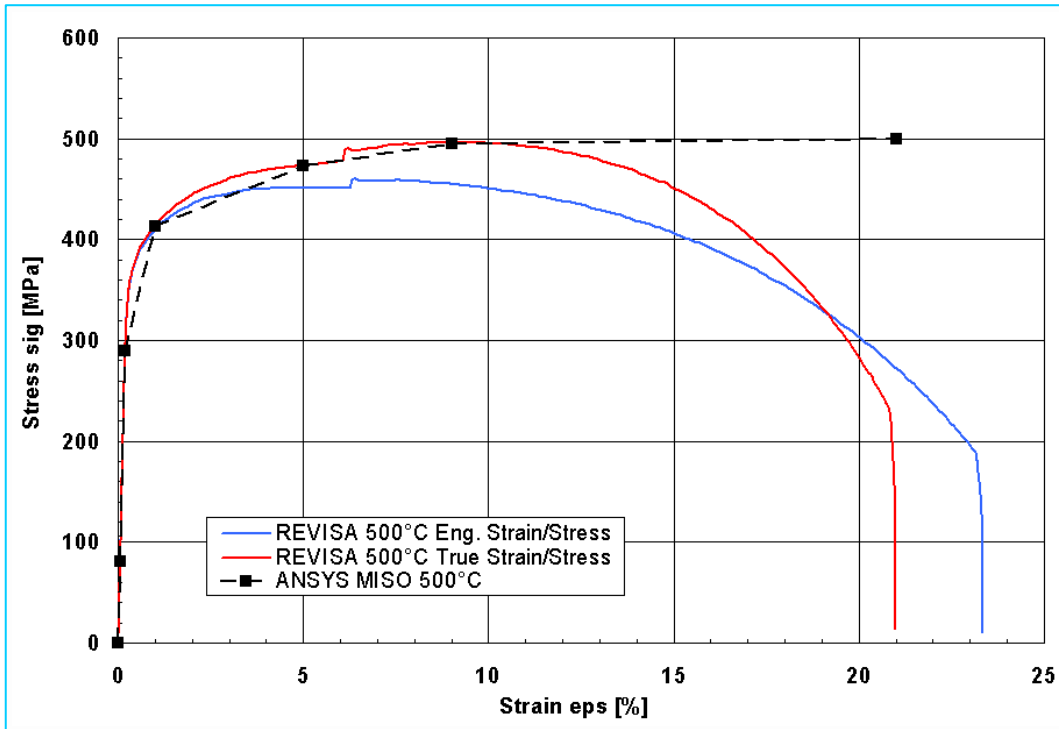
Figure A 18: Stress-strain curves of the RPV steel 16MND5 at 500 °C; CEA-measurement and modelling in ANSYS
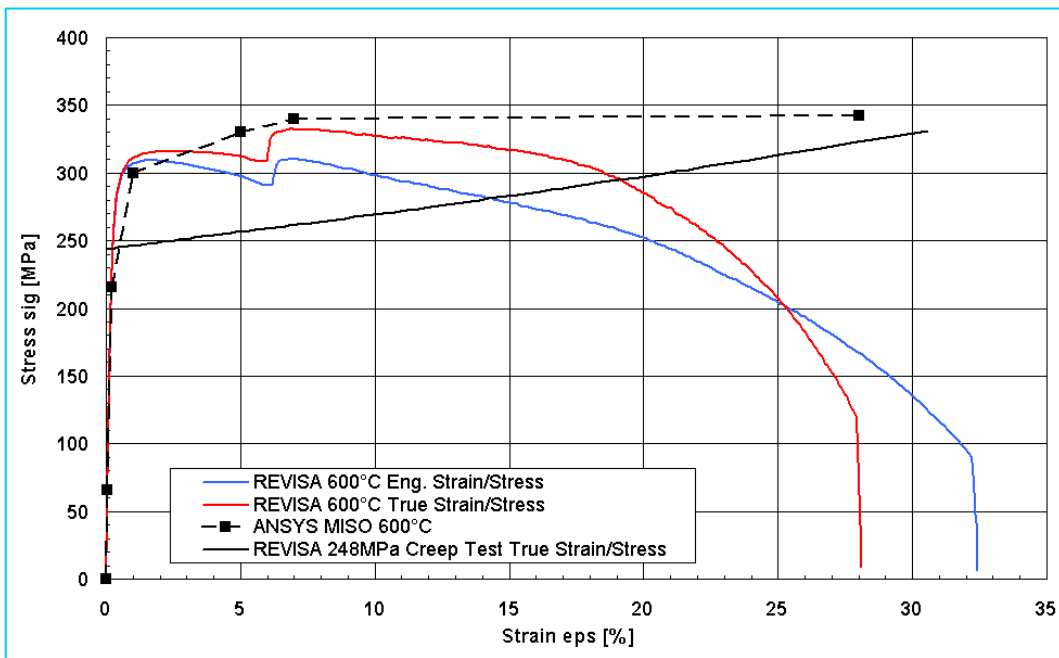
Figure A 19: Stress-strain curves of the RPV steel 16MND5 at 600 °C; CEA-measurement and modelling in ANSYS (dashed); black: values from creep test
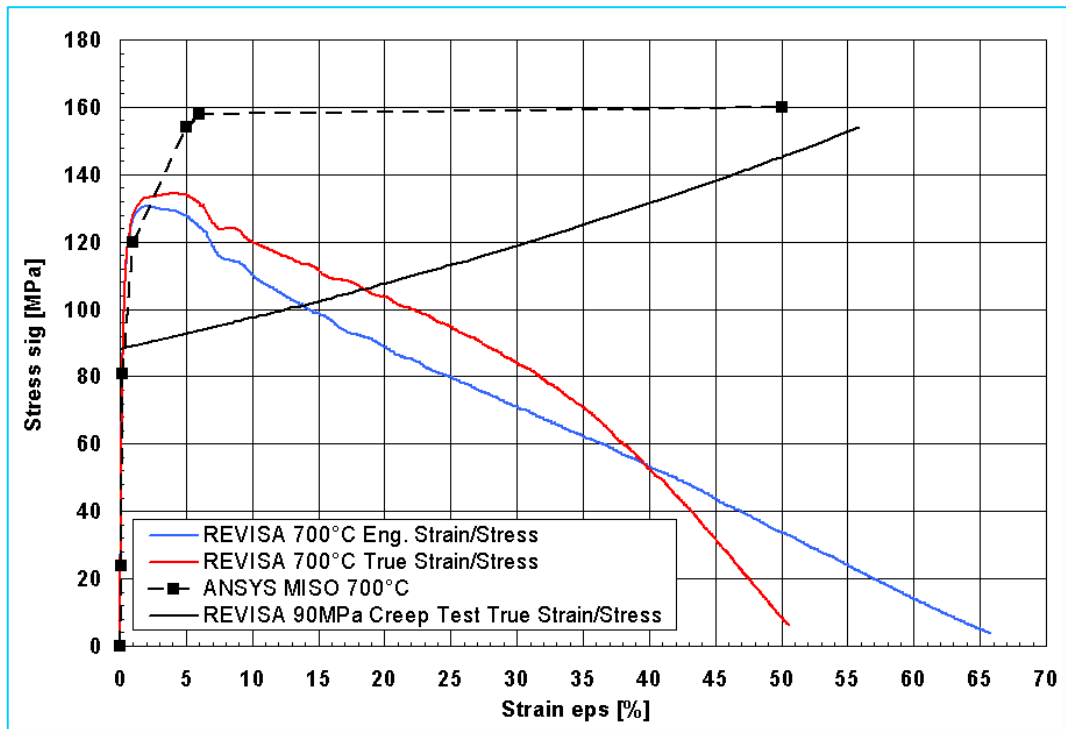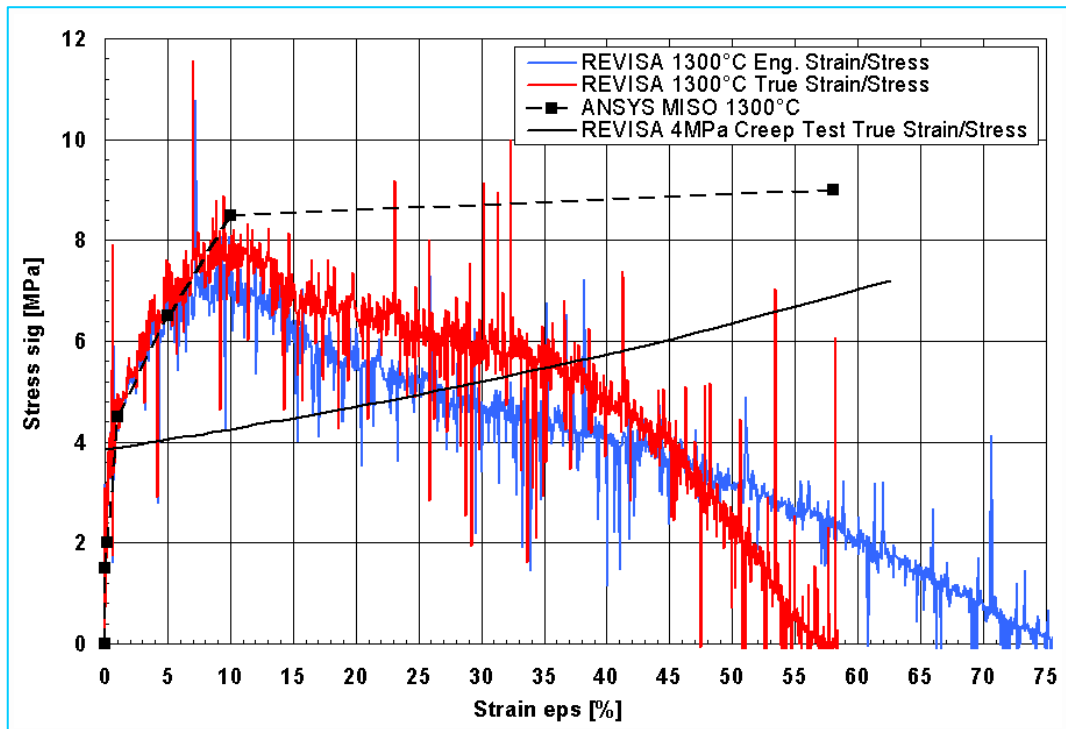
Figure A 20: Stress-strain curves of the RPV steel 16MND5 at 700 °C; CEA-measurement and modelling in ANSYS (dashed); black: values from creep test
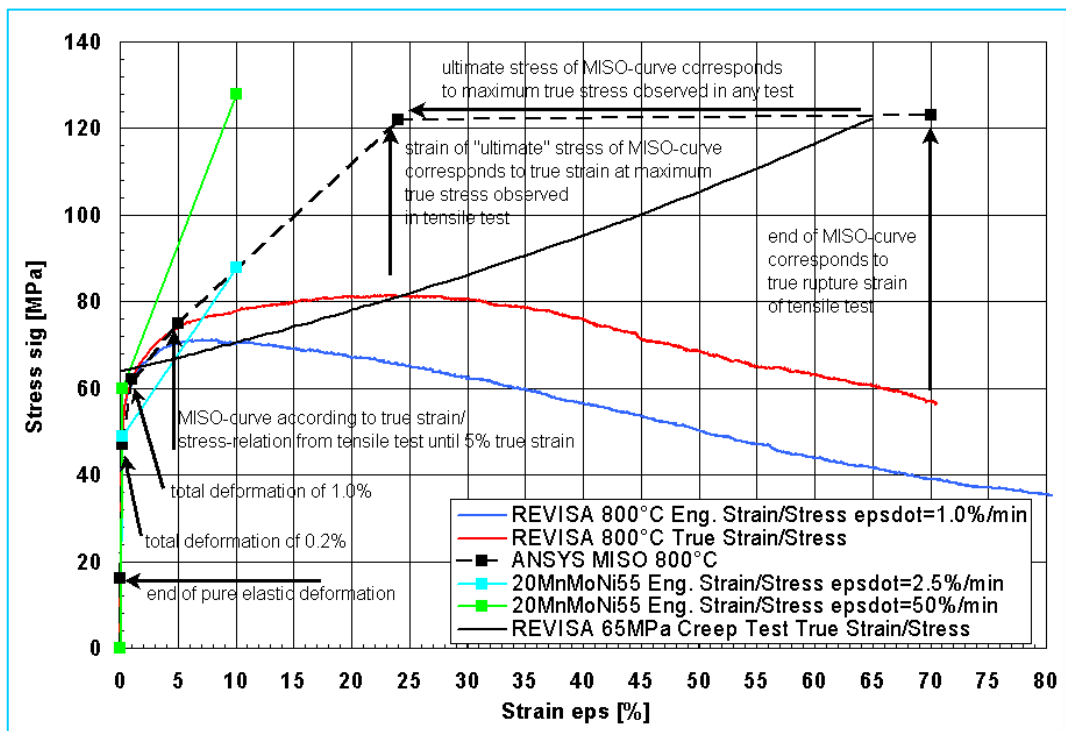

Figure A 21: Stress-strain curves of the RPV steel 16MND5 at 800 °C; CEA-measurement and modelling in ANSYS (dashed); black: values from creep test; cf. Figure 4-2
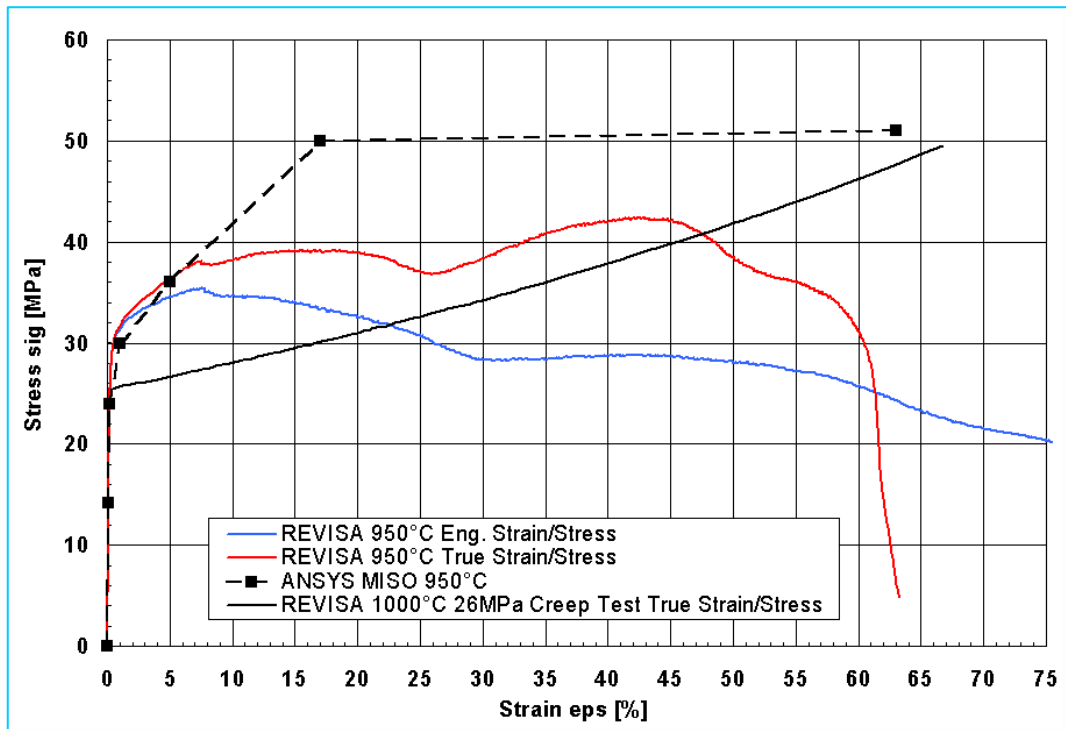
Figure A 22: Stress-strain curves of the RPV steel 16MND5 at 950 °C; CEA-measurement and modelling in ANSYS (dashed); black: values from creep test (1000 °C)
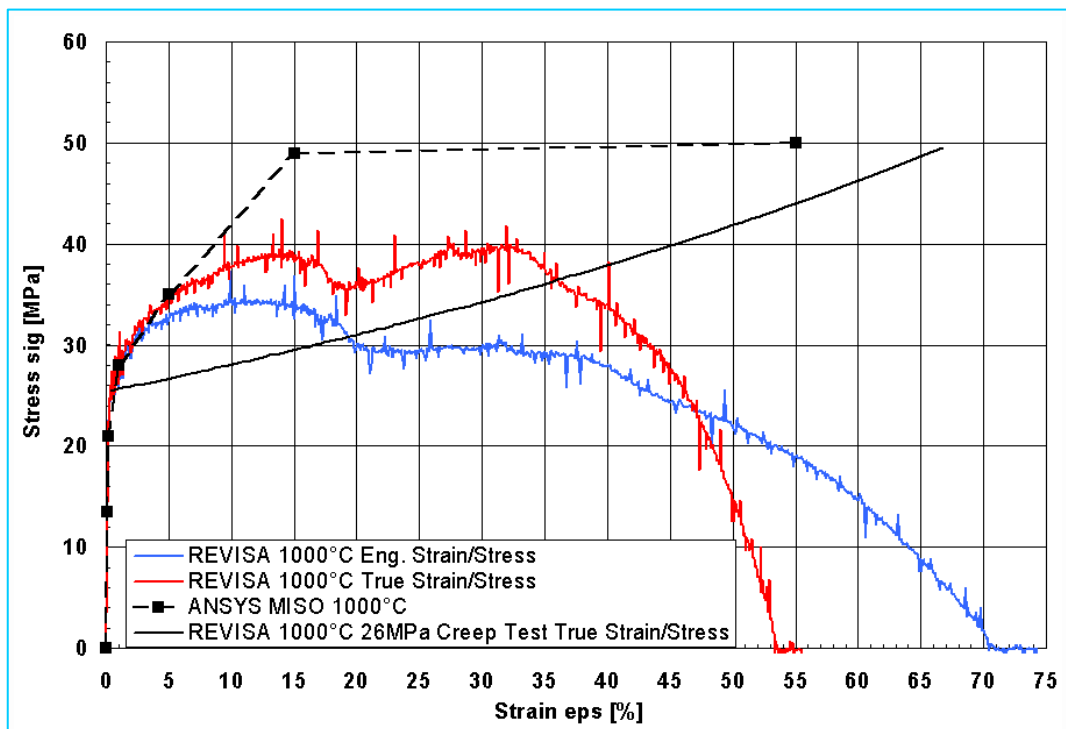
Figure A 23: Stress-strain curves of the RPV steel 16MND5 at 1000 °C; CEA-measurement and modelling in ANSYS (dashed); black: values from creep test
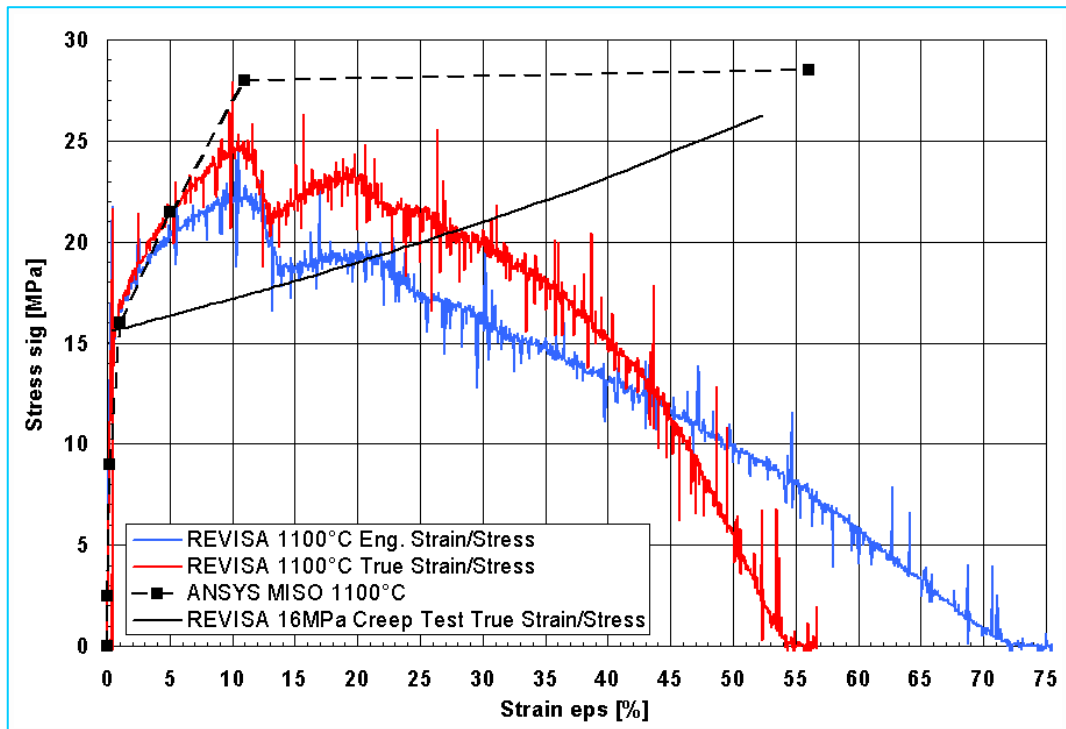
Figure A 24: Stress-strain curves of the RPV steel 16MND5 at 1100 °C; CEA-measurement and modelling in ANSYS (dashed); black: values from creep test
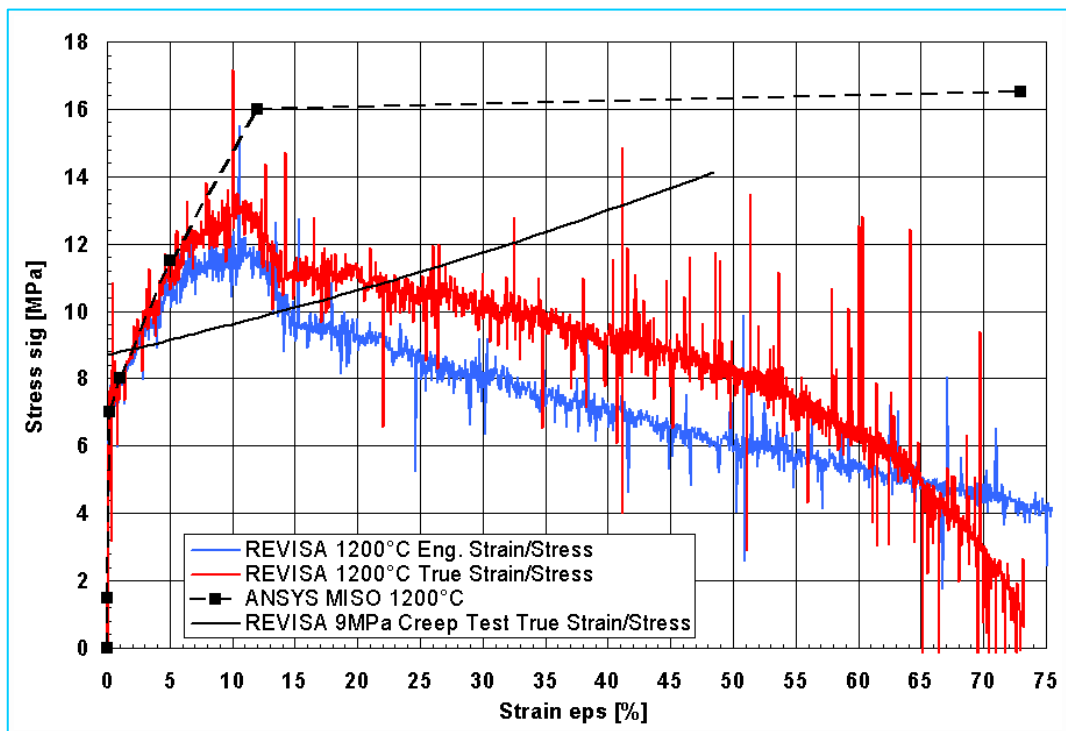
Figure A 25: Stress-strain curves of the RPV steel 16MND5 at 1200 °C; CEA-measurement and modelling in ANSYS (dashed); black: values from creep test

Figure A 26: Stress-strain curves of the RPV steel 16MND5 at 1300 °C; CEA-measurement and modelling in ANSYS (dashed); black: values from creep test
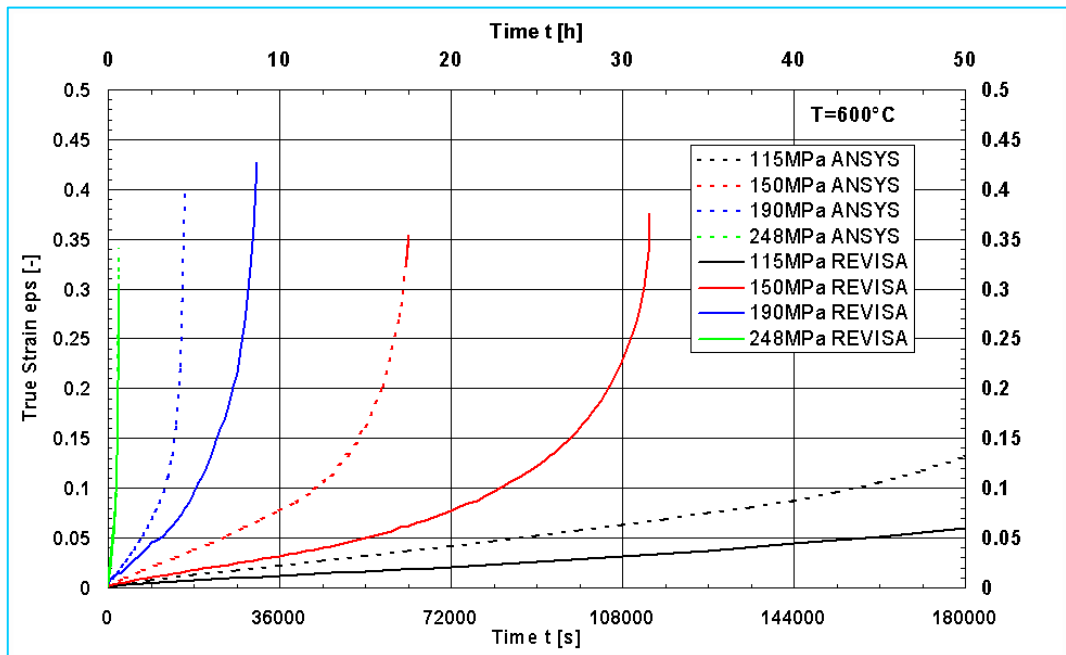
Figure A 27: Creep tests (CEA-measurement) and simulation of the creep tests using the creep data base, T= 600 °C
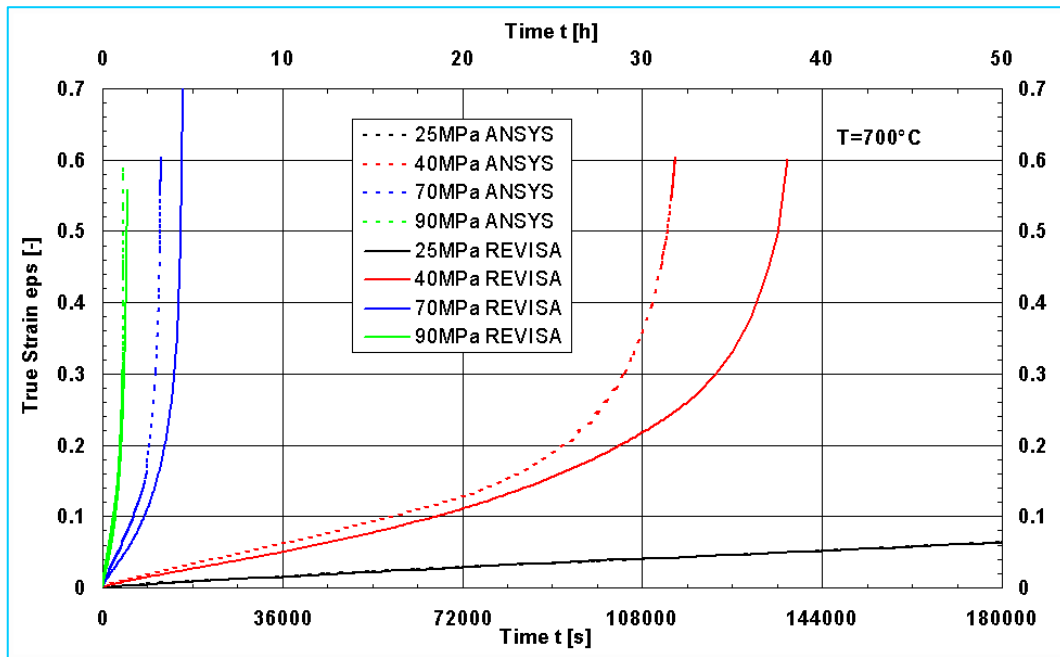
Figure A 28: Creep tests (CEA-measurement) and simulation of the creep tests using the creep data base, T= 700 °C
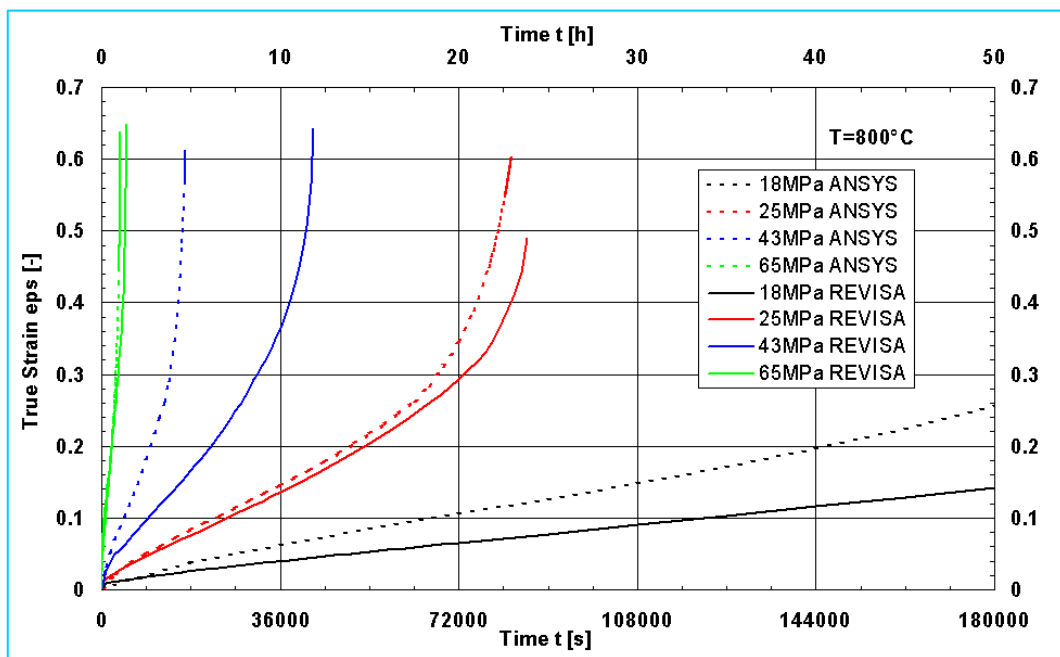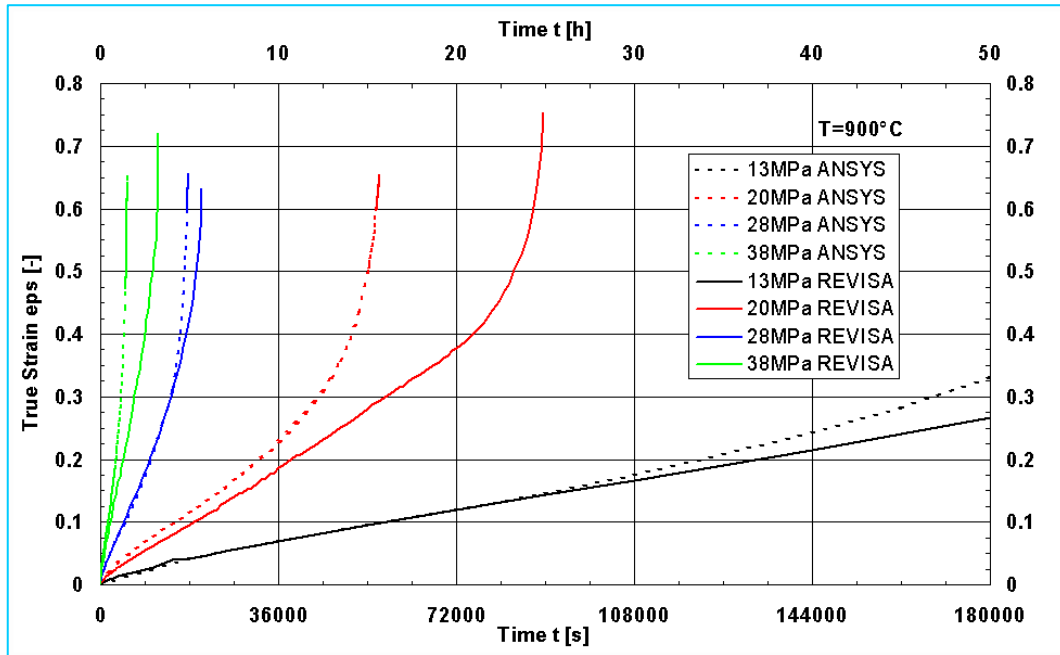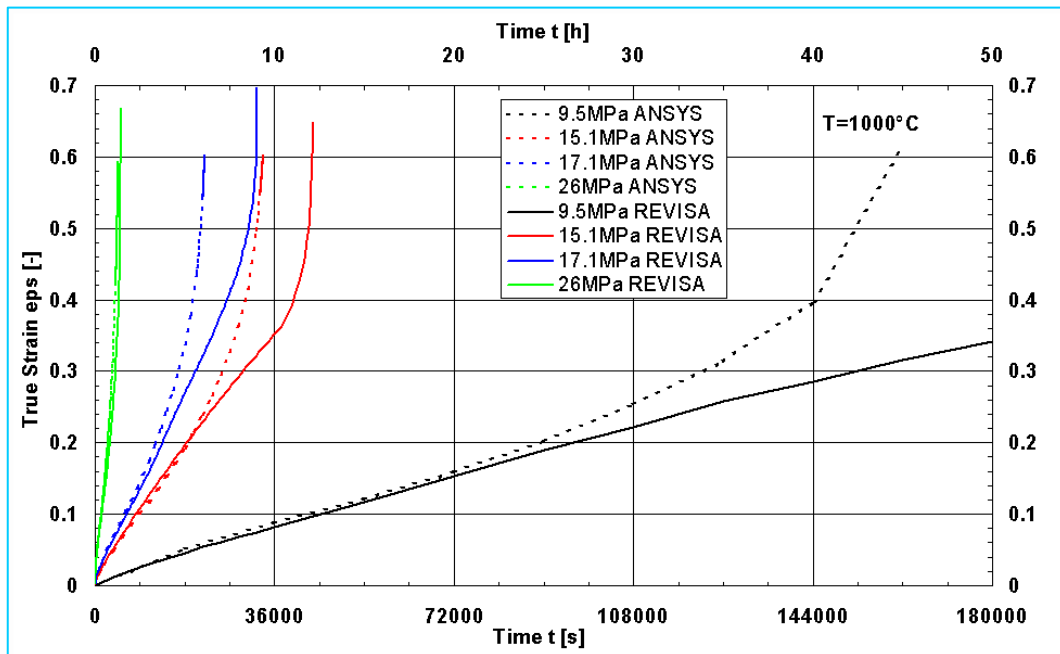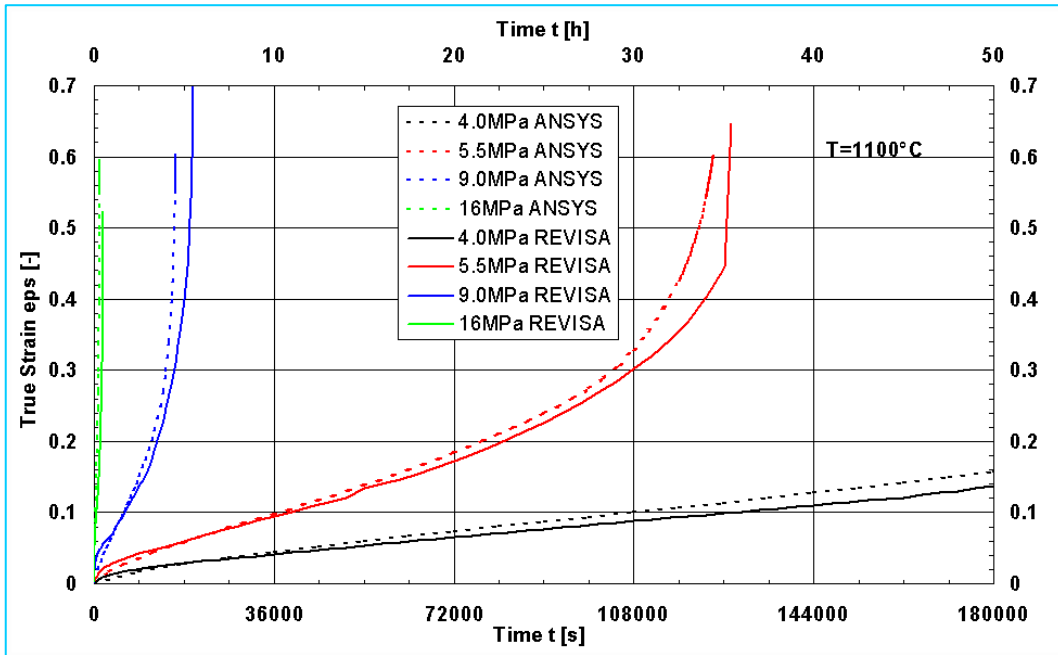

Figure A 29: Creep tests (CEA-measurement) and simulation of the creep tests using the creep data base, T= 800 °C
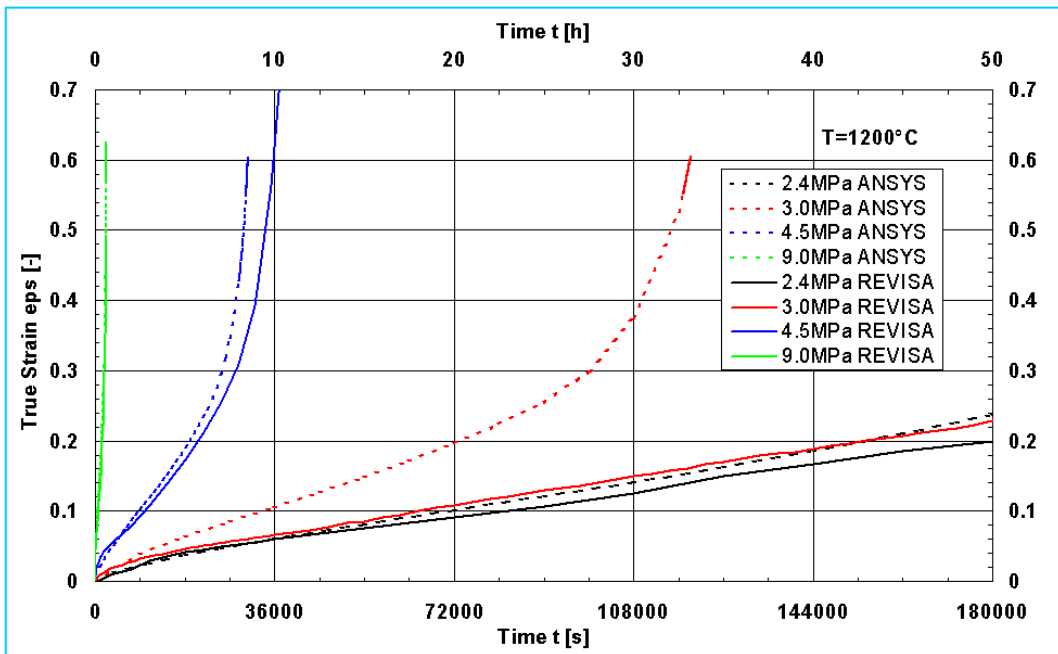
Figure A 30: Creep tests (CEA-measurement) and simulation of the creep tests using the creep data base, T= 900 °C

Figure A 31: Creep tests (CEA-measurement) and simulation of the creep tests using the creep data base, T= 1000 °C

Figure A 32: Creep tests (CEA-measurement) and simulation of the creep tests using the creep data base, T= 1100 °C

Figure A 33: Creep tests (CEA-measurement) and simulation of the creep tests using the creep data base, T= 1200 °C

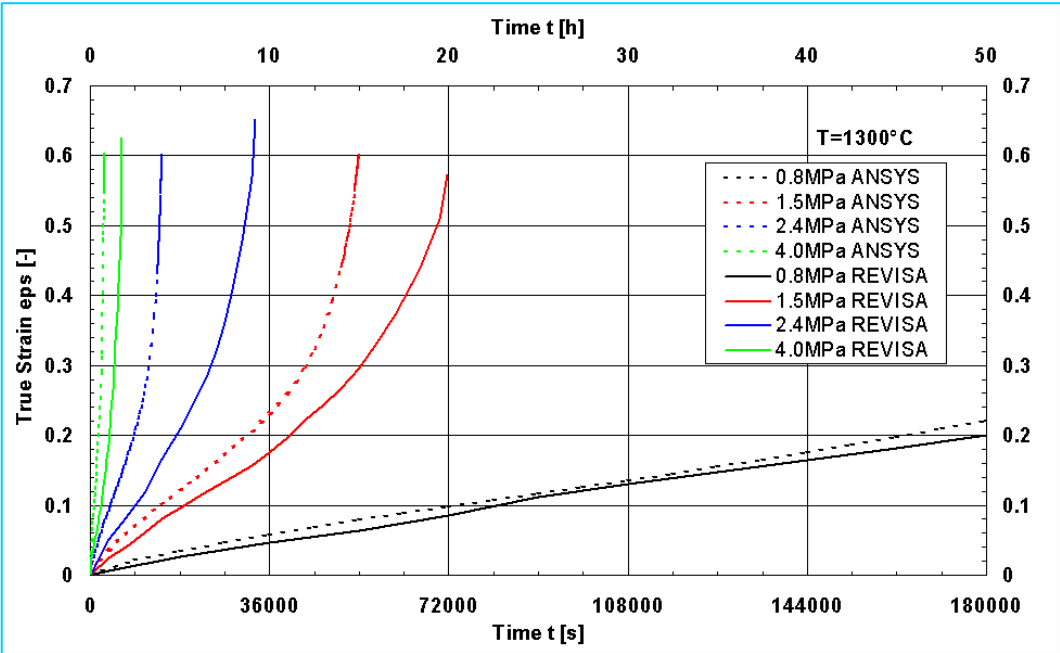**Figure A 34**: Creep tests (CEA-measurement) and simulation of the creep tests using the creep data base, T= 1300 °C